

République Algérienne Démocratique et Populaire  
Ministère de l'Enseignement Supérieur et de La Recherche Scientifique  
École Nationale Polytechnique



**Département Génie Mécanique**

**Laboratoire de Génie Mécanique et Développement**

**End of studies' Project**

Dissertation submitted in partial fulfillment of the requirements for the  
degree of the state engineer in mechanical engineering

---

**Design and Manufacture of a Windmill for Pumping Water**

---

**AOUIDAD Hichem Idris and AMMARI Mohamed Amine**

Under the direction of BOUHELAL Abdelhamid **MCA**, SMAILI Arezki  
**Professor** and BENBRAIKA Mohamed **MAA**.

Presented and publicly defended on 17/07/2024 in front of the jury composed of

President:	M. RECHAK Said	Professor at ENP
Examiner:	M. OUCHENE Samir	Doctor at ENP

ENP 2024

---

Mechanical Department/ ENP, 10 Rue des Frères OUDEK, El Harrach 16200 Algiers Algeria



République Algérienne Démocratique et Populaire  
Ministère de l'Enseignement Supérieur et de La Recherche Scientifique

**École Nationale Polytechnique**



**Département Génie Mécanique**

**Laboratoire de Génie Mécanique et Développement**

**End of studies' Project**

Dissertation submitted in partial fulfillment of the requirements for the  
degree of the state engineer in mechanical engineering

---

**Design and Manufacture of a Windmill for Pumping Water**

---

**AOUIDAD Hichem Idris and AMMARI Mohamed Amine**

Under the direction of BOUHELAL Abdelhamid **MCA**, SMAILI Arezki

**Professor** and BENBRAIKA Mohamed **MAA**.

Presented and publicly defended on 17/07/2024 in front of the jury composed of

President: M. RECHAK Said Professor at ENP

Examiner: M. OUCHENE Samir Doctor at ENP

ENP 2024

---

Mechanical Department/ ENP, 10 Rue des Frères OUDEK, El Harrach 16200 Algiers Algeria

République Algérienne Démocratique et Populaire  
Ministère de l'Enseignement Supérieur et de la Recherche Scientifique  
École Nationale Polytechnique



**Département Génie Mécanique**  
**Laboratoire de Génie Mécanique et Développement**

**Mémoire de Projet de fin d'études**

Pour l'obtention du diplôme d'ingénieur d'état en génie mécanique

---

Conception et Fabrication d'un Moulin à Vent pour Pompage d'Eau

---

**AOUIDAD Hichem Idris et AMMARI Mohamed Amine**

Sous la direction de BOUHELAL Abdelhamid **MCA**, SMAILI Arezki

**Professeur** et BENBRAIKA Mohamed **MAA**.

Présenté et soutenu publiquement le 17/07/2024 devant le jury composé de

Président : M. RECHAK Said Professeur à ENP  
Examineur : M. OUCHENE Samir Docteur à ENP

ENP 2024

## ملخص

يهدف هذا المشروع إلى تلبية الحاجة الملحة لإنتاج المياه اللامركزي من خلال تطوير نظام ضخ المياه بالطاقة الريحية. باستخدام الهندسة العكسية والتحسين الدقيق، تم تصميم الأجزاء باستخدام برامج التصميم بمساعدة الكمبيوتر وتم إنشاء نموذج مصغر عن طريق الطباعة ثلاثية الأبعاد وتم استخدام محاكاة الديناميكا الهوائية الحاسوبية لتحليل الأداء الديناميكي الهوائي. تم اختبار النموذج المصغر للتوربين الريحي في نفق هوائي للتحقق من نتائج المحاكاة. أظهرت مضخة رياحنا قدرات ضخ أعلى بكثير من تلك المثبتة في شركة بوفال.

**الكلمات المفتاحية:** الطاقة الهوائية، مضخة هوائية، مكبس المضخة، تحليل الديناميكا الهوائية، المحاكاة الرقمية.

## Résumé

Ce projet vise à répondre au besoin crucial de production d'eau décentralisée en développant un système de pompage d'eau alimenté par le vent. En utilisant la rétro-ingénierie et une optimisation rigoureuse, les pièces ont été conçues avec un logiciel de CAO, un modèle réduit a été créé via l'impression 3D, et des simulations CFD ont été employées pour analyser les performances aérodynamiques. La pompe à vent a montré des capacités de pompage nettement supérieur à celle installée à l'entreprise POVAL. Le modèle réduit de la turbine éolienne a été testé dans une soufflerie pour valider les résultats de la simulation.

**Mots clés :** Énergie éolienne, Pompe à vent, Rétro-ingénierie, Analyse aérodynamique, CFD.

## Abstract

This project addresses the critical need for decentralized water production by developing a wind-powered water pumping system. Using reverse engineering and rigorous optimization, parts were designed with CAD software, a scale model was created via 3D printing, and CFD simulations were employed to analyze aerodynamic performance. The wind pump showed significantly higher pumping capacity than the one installed at the POVAL company. The scaled-down wind turbine model was tested in a wind tunnel to validate the simulation results.

**Keywords:** Wind energy, Windmill, Reverse engineering, Aerodynamic analysis, CFD

# Acknowledgements

We would like to thank God, our creator, for giving us the strength to accomplish this work.

First and foremost, we extend our heartfelt gratitude to our supervisors, Pr. Arezki SMAILI, and Dr. Abdelhamid BOUHELAL, for always trusting us in how to conduct our work, for their advice and guidance. We also thank them for their availability, help, support, and human qualities.

We want to express our gratitude for their kindness during these three years of study in the Mechanical Engineering department, for their work within the department, and for everything they have done for the students' welfare.

A big thank you to Mr. Mohamed BENBRAIKA, our co-supervisor, who has always been attentive and available throughout the realization of this project. Thank you for your help, kindness, and encouragement.

We particularly thank the head of the Fablab, Mr. Abdelkarim LAHLAH and M. M'hamed BOUSBAI, FabLab and ENP incubator manager for their help and availability during the completion of this project.

A big thank you to Pr. Said RECHAK and Dr. Samir OUCHENE for agreeing to evaluate this work. It is an honor to have them on the jury for this final project.

Our deepest gratitude goes to the teachers of the Mechanical Engineering department and the ENP in general, thanks to whom we have been able to reach this point. Specifically Mr. Yacine BELKACEMI and Mr. Brahim GUERGUEB, for their advice, support, efforts, help, and especially for their human qualities.

# Dedications

*I dedicate this work to all the people who have extended a helping hand in my life.*

*To my dear parents and my grandmother, for their unconditional and limitless support.*

*To my only and dear sister Ines, who is far from us but always present in our hearts.*

*To my dear family.*

*To all my friends, with whom I have shared unforgettable moments. Without you, I don't know how I would have gotten through these years. Know that you are always in my heart, and I wish you a brilliant career, inshallah.*

*Once again, a huge dedication to all the people who have helped me in my university endeavors, in my studies, and in my life in general. Know that I am always at your disposal.*

*I love you and wish you all the best.*

*AOUIDAD Hichem Idris*

*I dedicate this work to all the people who have extended a helping hand in my life.*

*To my dear parents, for their unconditional and limitless support.*

*To my only and dear brother Imad.*

*To my dear family.*

*To all my friends, with whom I have shared unforgettable moments. Without you, I don't know how I would have gotten through these years. Know that you are always in my heart, and I wish you a brilliant career, inshallah.*

*Once again, a huge dedication to all the people who have helped me in my university endeavors, in my studies, and in my life in general. Know that I am always at your disposal.*

*I love you and wish you all the best.*

*AMMARI Mohamed Amine*

# Table of Contents

List of Tables

List of Figures

Nomenclature

<b>Introduction .....</b>	<b>15</b>
<b>Generalities and Literature Review .....</b>	<b>19</b>
1.1 Introduction .....	19
1.2 State of the art.....	21
1.3 Operation Theory of Piston pumps.....	23
1.3.1 Principle of Operation .....	24
1.3.2 Operating Conditions of a Slow Wind Turbine with Piston Pump.....	24
1.3.3 Froud Number.....	25
1.3.4 The Torque Cycle of a Wind Pump .....	26
1.4 Methodology of the Blade Element Momentum Theory .....	27
1.4.1 Axial Momentum Theory .....	27
1.4.2 Ideal horizontal axis turbine with wake rotation.....	30
1.4.3 Aerodynamic forces.....	31
1.4.4 Viterna Extrapolation .....	32
1.4.5 3D Correction.....	33
1.4.6 Blade Element Momentum Theory .....	35
1.4.7 Development of the BEM Performance Prediction Algorithm .....	36
1.5 Problematic .....	37

1.6 Objective.....	38
<b>Design and Modeling.....</b>	<b>39</b>
2.1 Introduction .....	39
2.2 Reverse engineering .....	39
2.3 Wind turbine design.....	44
2.3.1 General considerations.....	44
2.3.2 Solidity.....	45
2.3.3 Blade number effect.....	47
2.3.4 Blade shape .....	48
2.3.5 Optimal pitch angle .....	50
2.3.6 Structural analysis of the blade.....	50
2.4 Piston Pump Design .....	51
2.4.1 Calculation methodology.....	52
2.5 Reducer design.....	55
<b>Numerical Simulation of the scaled model .....</b>	<b>60</b>
3.1 Introduction .....	60
3.2 Wind turbine scaling .....	60
3.3 CFD step by step .....	62
3.3.1 Geometry preparation.....	63
3.3.2 Mesh Preprocessor.....	64
3.3.3 Solver configuration .....	67
3.3.4 Mesh dependency .....	71
<b>Fabrication and Experimental Validation .....</b>	<b>73</b>
4.1 Manufacturing Experience .....	73
4.2 Operation of the test bench system .....	76

4.3 Assessment of uncertainty propagation.....	78
<b>Results and Discussion.....</b>	<b>81</b>
5.1 Discussion of numerical simulation CFD results .....	81
5.2 Experimental results.....	86
5.2.1 Discussion of experimental tests.....	86
5.2.2 Comparative study between BEM, CFD and experimental results.....	88
<b>General conclusion.....</b>	<b>90</b>
<b>References.....</b>	<b>91</b>
<b>Appendices.....</b>	<b>95</b>
<b>Appendix A.....</b>	<b>95</b>
A. Mechanism of a slow wind turbine.....	95
<b>Appendix B.....</b>	<b>97</b>
B.1 Poval Windmill Data Sheet .....	97
B.2 Proposed Windmill Data Sheet .....	98
<b>Appendix C.....</b>	<b>99</b>

# List of Tables

<b>Table 2.1</b> Different Parts of the Windmill. ....	44
<b>Table 2.2</b> Wind turbines design characteristics. ....	45
<b>Table 2.3</b> Qualitative comparison of horizontal axis rotor types. ....	45
<b>Table 2.4</b> Input data for the BEM simulations. ....	50
<b>Table 2.5</b> Wind turbine input data. ....	54
<b>Table 2.6</b> Piston pump input data. ....	54
<b>Table 2.7</b> Derived parameters. ....	54
<b>Table 2.8</b> Common standard modules. ....	57
<b>Table 2.9</b> Pinions parameters. ....	57
<b>Table 2.10</b> Wheels parameters. ....	58
<b>Table 3.1</b> Scaling laws of wind turbines without Reynolds number matching. ....	61
<b>Table 3.2</b> Output data of the scaling operation. ....	62
<b>Table 3.3</b> Wall distance calculations for inflation configuration. ....	66
<b>Table 3.4</b> mesh dependency results. ....	71
<b>Table 4.1</b> Designations of the different mechanical components. ....	74
<b>Table 5.1</b> Poly BEM vs No Poly Bem correction. ....	85
<b>Table 5.2</b> Results of wind speed measurements. ....	86
<b>Table 5.3</b> Results of rotational speed measurements. ....	86
<b>Table 5.4</b> Comparison between BEM, CFD and experimental results. ....	88

# List of Figures

<b>Figure 1</b> Wind map of Algeria from 2018.....	16
<b>Figure 2</b> (a) The windmills at Kinderdijk in the village of Kinderdijk, Netherlands is a UNESCO World Heritage Site (b) L'Olifant à Burdaard (Frise).....	17
<b>Figure 1.1</b> Multi-blade wind pump.....	20
<b>Figure 1.2</b> Pumped storage wind turbines studied and developed at CDER (a) small wind turbine (b) "El Hayat" horizontal axis wind pump turbine (c) "Savonius" type 2-stage vertical axis wind pump (d) Horizontal axis wind pump.....	21
<b>Figure 1.3</b> The configuration of the crank .....	26
<b>Figure 1.4</b> Moment Cycle for a Single Acting Pump .....	27
<b>Figure 1.5</b> An actuator disk .....	28
<b>Figure 1.6</b> Dimensionless power and thrust coefficients as a function of axial induction coefficient.....	30
<b>Figure 1.7</b> Rotor analysis geometry .....	30
<b>Figure 1.8</b> Blade geometry for the analysis of a horizontal axis wind turbine .....	35
<b>Figure 1.9</b> Brief roadmap of the work.....	38
<b>Figure 2.1</b> WP-2 Windmill .....	40
<b>Figure 2.2</b> Rotor Assembly .....	41
<b>Figure 2.3</b> Reverse Engineering of Tail Vane.....	41
<b>Figure 2.4</b> Reverse engineering of the wind turbine.....	42
<b>Figure 2.5</b> Reverse engineering of the piston pump (a) suction valve (b) discharge valve (c) cylinder .....	42
<b>Figure 2.6</b> Transmission system.....	43
<b>Figure 2.7</b> Reverse engineering of the tower.....	43
<b>Figure 2.8</b> Single blade to multi blades wind rotor solidity.....	46
<b>Figure 2.9</b> Schematic diagram of three-blade and multi-blade airflow.....	47
<b>Figure 2.10</b> Blade's Number influence on (a) moment coefficient (b) power coefficient.....	48
<b>Figure 2.11</b> (CP-160-050-GN) Camber=16% Wall thickness=5% Radius=0.861. Max thickness 5.2% at 3.4% chord. Max camber 14.3% at 49.2% chord.....	49
<b>Figure 2.12</b> Glide Ratio $C_l/C_d$ curve.....	49
<b>Figure 2.13</b> Optimal pitch angle.....	50
<b>Figure</b> Blade edgewise and flapwise moments.....	51
<b>Figure 2.14</b> Structural analysis of the blade made form galvanised steel.....	51

<b>Figure 2.15</b> Cp and Cm - TSR curve.....	54
<b>Figure 2.16</b> Nominal gear Ratios. ....	56
<b>Figure 3.1</b> Control volume.....	64
<b>Figure 3.2</b> Law wall regions . ....	65
<b>Figure 3.3</b> Detailed view of blade inflation.....	67
<b>Figure 3.4</b> Clear view of the mesh around blade (a) trailing edge (b) leading edge.....	67
<b>Figure 3.5</b> Periodic boundary conditions. ....	68
<b>Figure 3.6</b> Wall function limitations.....	69
<b>Figure 3.7</b> Statistics on the values of $y^+$ around the blade.....	71
<b>Figure 3.8</b> Contour plot of the $y^+$ values near the blade.....	72
<b>Figure 4.1</b> 3D printer (a) Ender 3 (b) Creality 10.....	74
<b>Figure 4.2</b> Final Assembly of the windmill.....	75
<b>Figure 4.3</b> Wind tunnel. ....	76
<b>Figure 4.4</b> Diagram of forces. ....	77
<b>Figure 4.5</b> Anemometer. ....	79
<b>Figure 4.6</b> Tachometer.....	79
<b>Figure 4.7</b> Calibrated weights. ....	80
<b>Figure 5.1</b> Pressure Variance.....	82
<b>Figure 5.2</b> Velocity contour plot. ....	82
<b>Figure 5.3</b> Airfoil pressure contour plot at the half of the blade.....	83
<b>Figure 5.4</b> Velocity contour plot of the airfoil at the half of the blade. ....	83
<b>Figure 5.5</b> DTU ploy bem correction effect. ....	84
<b>Figure 5.6</b> Induction factor formulas effect on the thrust coefficient .....	85
<b>Figure 5.7</b> Thrust coefficient of the wind turbine.....	85
<b>Figure 5.8</b> Cp-TSR curve comparison between BEM, CFD and experimental results.....	89
<b>Figure 5.9</b> Cm-TSR curve comparison between BEM, CFD and experimental results. ..	89

# Nomenclature

## Abbreviations

<i>AEP</i>	Annual Energy Production
<i>AR</i>	Aspect Ratio
<i>BEM</i>	Blade Element Momentum Theory
<i>HAWT</i>	Horizontal Axis Wind Turbine
<i>TSR</i>	Tip Speed Ratio

## Latin letters

<i>A</i>	Rotor Swept Area	(m <sup>2</sup> )
<i>a</i>	Axial Induction Factor	
<i>a'</i>	Tangential Induction Factor	
<i>A<sub>1</sub></i>	Cross-Surface of the Stream Tube Upstream of the Rotor	(m <sup>2</sup> )
<i>A<sub>4</sub></i>	Cross-Surface of the Stream Tube Downstream of the Rotor	(m <sup>2</sup> )
<i>B</i>	Rotor Blades Number	
<i>b</i>	Dimensionless Constant	
<i>C<sub>d</sub></i>	Drag Coefficient	
<i>C<sub>d2D</sub></i>	Two-dimensional Drag Coefficient	
<i>C<sub>d3D</sub></i>	Three-dimensional Drag Coefficient	
<i>C<sub>dmax</sub></i>	Maximal Drag Coefficient	
<i>C<sub>l</sub></i>	Lift coefficient	
<i>C<sub>l2D</sub></i>	Bidimensional Lift Coefficient	
<i>C<sub>l3D</sub></i>	Tridimensional Lift Coefficient	
<i>C<sub>l<sub>stall</sub></sub></i>	Stall Lift Coefficient	
<i>C<sub>n</sub></i>	Normal Coefficient	
<i>C<sub>T0</sub></i>	Turbine torque coefficient close to zero rotational speed	
<i>C<sub>TC</sub></i>	Critical torque coefficient of the turbine	
<i>C<sub>TM</sub></i>	Maximum torque coefficient of the turbine	
<i>C<sub>TD</sub></i>	Torque Coefficient at Design Point	
<i>C<sub>t</sub></i>	Tangential Coefficient	
<i>C<sub>Tr</sub></i>	Local Thrust Coefficient	
<i>C<sub>P</sub></i>	Power coefficient	

$F$	Total Losses Correction	
$F_{hub}$	Hub Loss Correction	
$F_d$	Drag Force	(N)
$F_l$	Lift Force	(N)
$F_n$	Normal Force	(N)
$F_t$	Tangential Force	(N)
$F_{tip}$	Tip Loss Correction	
$d$	Turbine rotor diameter	(m)
$Fr$	Froude Number	
$h$	Total pump head	(m)
$L_B$	Length of the blade	(m)
$m$	Number of effective piston strokes per cycle	
$n_p$	Pump speed	(cycle per second)
$n_t$	Turbine speed	(rpm)
$q$	Average water flow	(m <sup>3</sup> /s)
$r_N$	Rotational speed increase ratio, $n/n_t$	
$s$	Pump stroke	(m)
$v$	Average Wind speed	(m/s)
$V_s$	Swept volume of the pump cylinder	(m <sup>3</sup> )
$k$	Shape Factor	
$m$	Scale Factor	(m/s)
$n$	Corrigan-Schilling Empirical Factor	
$P$	Rotor Power	(W)
$p$	Pressure	(Pa)
$p_1 p_2$	Air pressures upstream of the actuator disk	(Pa)
$p_3 p_4$	Air pressures downstream of the actuator disk	(Pa)
$Q$	Rotor Torque	(N.m)
$R$	Rotor Radius	(m)
$r$	Radial Distance of Blade Element	(m)
$Re$	Reynolds Number	
$T$	Thrust Force	(N)
$t$	Airfoil Thickness	(m)
$U$	Wind speed	(m/s)
$U_1 U_2$	Upstream wind speed of the actuator disk	(m/s)
$U_3 U_4$	Downstream wind speed of the actuator disk	(m/s)
$U_{rel}$	Relative Wind speed	(m/s)

### Greek symbols

$\alpha$	Angle of Attack	(°)
----------	-----------------	-----

$\alpha_{stall}$	Stall Angle of Attack	(°)
$\lambda$	Tip speed Ratio	
$\lambda_r$	Local Tip Speed Ratio	
$\dot{m}$	Mass Flow	(kg/s)
$\nu$	Kinematic Viscosity of the Air	(m <sup>2</sup> /s)
$\Omega$	Rotational Speed	(rpm)
$\omega$	Wake Rotation Speed	(rpm)
$\varphi$	Relative Angle	(°)
$\rho$	Density of the Air	(kg/m <sup>3</sup> )
$\sigma$	Solidity	
$\theta_p$	Pitch Angle of the Blade	(°)
$\theta_t$	Twist Angle of the Blade	(°)
$\eta_p$	Pump efficiency	
$\eta_{Tr}$	Wind-pump mechanical transmission efficiency	
$\eta$	Overall efficiency of the windmill	
$\gamma$	Efficiency of the Wind Pump Mechanical Transmission	
$\rho_a$	Air density	(kg/m <sup>3</sup> )
$\rho_{water}$	Water density	(kg/m <sup>3</sup> )

# Introduction

In the context of sustainable development and the energy transition, the challenges of the century are to end dependence on fossil fuels and ensure water access and food security. Water being the source of life, we are unable to supply it to the entire population which continues to increase with its demand at the same time, and this is because of climate change which has destabilized the natural water cycle, however it's necessary to ensure the supply of water to strategic localities such as agriculture and hygiene. The windmill for pumping water remains the most suitable solution, a decentralization of water production that means energy security while remaining the cheapest and cleanest.

Small wind turbines can make a significant contribution to the country's energy security. Indeed, several regions in Algeria, in the north, the highlands and the south, have significant wind potential. In the south of the country, in the regions of Adrar and Ain Salah, the average wind speeds available at a height of 10 m vary from 5 to 6 m/s. In Biskra, the speeds recorded are around 4.5 m/s. In the highlands, in the regions of M'Sila, Tiaret and Djelfa, the average speeds are 4 to 5 m/s. In the north of the country, the average speeds recorded in the regions of Algiers, Oran and Jijel are close to 4 m/s [1]. In cases where the wind speed averages are 4 to 7 m/s, the water pumping time is about 6 to 8 hours [2]. The available wind power potential is suitable for the operation of small wind energy conversion systems, especially in the agricultural sector. Irrigation, which is a common need for agricultural production, particularly in arid and semi-arid regions, requires the pumping of water from groundwater. Given the high price of fossil fuels, irrigating by wind pumps can be an alternative to motor pumps in Algeria. In addition, in our country, most agricultural farms are on flat and open land, which is favorable to the installation of wind energy conversion systems [3].

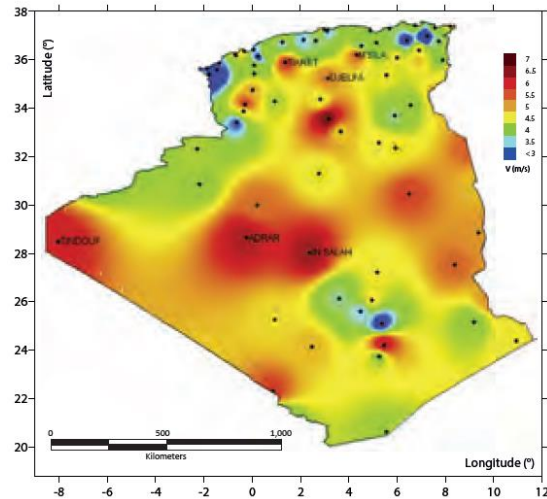


**Figure 1.** Wind map of Algeria from 2018 [1].

A small wind system with a capacity ranging from 1 to 10 kW can be a competitive solution, compared to motor pump units. Small wind power can reduce the cost of electricity for isolated agricultural farms where the electricity grid is not available while providing a non-polluting source of energy. In addition, small wind systems on agricultural farms do not affect crops. The installation of a wind turbine on an agricultural farm makes it possible to conserve more than 98% of the area to be cultivated [3].

A wind pump is a type of wind turbine used to pump water. Wind pumps have been used to pump water since at least the 9th century in various regions, including Afghanistan, Iran, and Pakistan [4]. Their use spread to the Muslim world, then to China and India. In Europe, especially in the Netherlands and the East Anglia region of Great Britain, wind pumps were widely used from the late Middle Ages onwards to drain land for agricultural purposes. Simon Stevin's work, in particular his book "Vande Molens", has made it possible to improve the efficiency of wind turbines for pumping water from the polders. In 1586, Stevin was granted a patent for his improvements. Windmills with eight or ten blades were used in the Murcia region of Spain for irrigation. These mills used the movement of the rotor to turn a Noria, a large wheel supporting a bucket chain plunging into a shaft [5]. In 1737, Bernard Forest de Belidor described the mechanism of a suction pump driven by the wings of a windmill in his work "Hydraulic Architecture" [6]. In the United States, early immigrants introduced European windmill technology. These mills were used on farms, especially on the Great Plains, to pump water from wells and water livestock. Daniel Halladay invented the self-regulating agricultural wind pump in 1854 [7]. At their peak in 1930, about 600,000 units were in use in the United States, with an average power of 250 watts [8].



(a)



(b)

**Figure 2.** (a) The windmills at Kinderdijk in the village of Kinderdijk, Netherlands is a UNESCO World Heritage Site (b) L'Olifant à Burdaard (Frise) [9].

This thesis is structured into five comprehensive chapters as follows:

**Chapter 1:** This chapter provides an overview of wind-powered piston pumps, comparing mechanical and electric wind pumps, and presenting current technologies and advancements. It outlines the research problem, objectives, and methodology. The chapter also examines the functional and mathematical aspects of conventional piston pumps, addressing efficiency issues like crawling and exploring optimization methods to enhance performance. Additionally, it covers the theory of wind turbines, emphasizing the importance of managing operational parameters for optimal efficiency. Understanding these concepts is essential for designing and optimizing wind-powered systems.

**Chapter 2:** This chapter discusses the reverse engineering processes undertaken to understand and improve existing designs. It includes the design of the wind turbine, detailing the steps involved in the conceptualization and development. Additionally, the chapter covers the sizing of the piston pump and the transmission system.

**Chapter 3:** This chapter is dedicated to the Computational Fluid Dynamics (CFD) numerical simulations performed on the scaled model of the wind pump system. It describes the simulation setup, parameters considered, and the results obtained. The insights gained from these simulations are important for validating the design and predicting the performance under various operating conditions.

**Chapter 4:** Focusing on the experimental aspects, this chapter describes the

fabrication of the scaled model and the subsequent tests and measurements conducted. It provides detailed procedures and methodologies for the experiments, ensuring that the results are reliable and reproducible. The chapter also discusses the challenges encountered during the experimental phase and how they were addressed.

**Chapter 5:** The final chapter presents a comprehensive discussion of the results obtained from both the numerical simulations and the experimental work. It compares the findings, highlights the discrepancies, and provides explanations for the observed phenomena. The chapter concludes with an evaluation of the overall performance of the wind pump system, offering recommendations for future research and potential improvements.

Finally, concluding remarks and some perspectives are presented

# Chapter 1

## Generalities and Literature Review

### 1.1 Introduction

Multi-blade wind turbines are widely used around the world, at the beginning of the twentieth century, these machines were abandoned as fossil fuels became more competitive and the electricity grid expanded. Nevertheless, the last few decades have seen the re-emergence of wind energy and, above all, the development of a new pumping process [10]. Often referred to as “weather vanes” in the United States and Canada because of their ability to orient themselves according to the direction of the wind (while also measuring its speed). A wind turbine with a diameter of 4.8 meters can pump up to 6 tons of water per hour at a height of 30 meters with a wind blowing at a speed of between 24 and 32 km/h [11]. However, they require a steady wind to start and drive the piston pump. These wind installations require little maintenance, usually limited to the annual gearbox oil change. They are particularly useful in remote areas where access to electricity is limited, and maintenance is difficult.



**Figure 1.1** Multi-blade wind pump.

The design of a wind pump depends on the type of machine to be developed. A distinction must be made between a mechanical wind pump and an electric wind pump:

**1- Mechanical wind pumping**, the operating principle is as follows: a wind rotor of about twenty blades drives, by a connecting rod and crank system, a piston pump plunged to the bottom of the well. It is a system that is quite suitable for areas with very little wind and in isolated places (where it is impossible or too expensive to connect to the network), with low daily water requirements and well depths not exceeding 30 m [12]. Mechanical wind pumps are divided into three segments based on wind speed: light, medium, and strong. Light pumps start at wind speeds of 2 or 3 m/s, medium pumps at 3-4 m/s, and strong pumps at 4-5 m/s [13]. Mechanical wind pumps are equipped with piston pumps that work best at moderate wind turbine rotational speeds. But mechanical reliability problems are encountered for very deep wells [12].

**2- Wind-electric pumping**, several wind-electric pumping systems exist, but the most common is undoubtedly the one with the following configuration; a wind rotor equipped with two to three blades is coupled to a permanent magnet generator which directly powers a three-phase induction motor which in turn is coupled to a pump, whether surface or submersible. They are equipped with centrifugal pumps that work well, preferably at high rotational speeds. However, the pump can be installed far from the wind turbine and the pumping head can be high [12].

From the two wind pumps systems described above, it can be concluded that

electric wind pumping is much more efficient than mechanical wind pumping. In the case of deep wells and large flows, the alternative of pumping with wind power remains the only solution [12].

## 1.2 State of the art

The first work of the CDER renewable energy development center in Algeria was carried out on water pumping wind turbines as shown in Figure 1.2 before moving on to electricity production. Two types of wind turbines have been built and tested: the first is a horizontal-axis, multi-bladed, slow wind turbine, coupled to a piston pump via a connecting rod-crank system. This wind turbine has been designed for total head measurements (HMTs) of 10 meters. The second prototype, a Savonius wind turbine with a vertical axis and two stages, with a 10-metre HMT, was coupled to a piston pump via a speed multiplier with bevel gearbox. In parallel with these achievements, CDER has carried out studies on the reliability of the El Hayet wind turbines of the POVAL company [13].

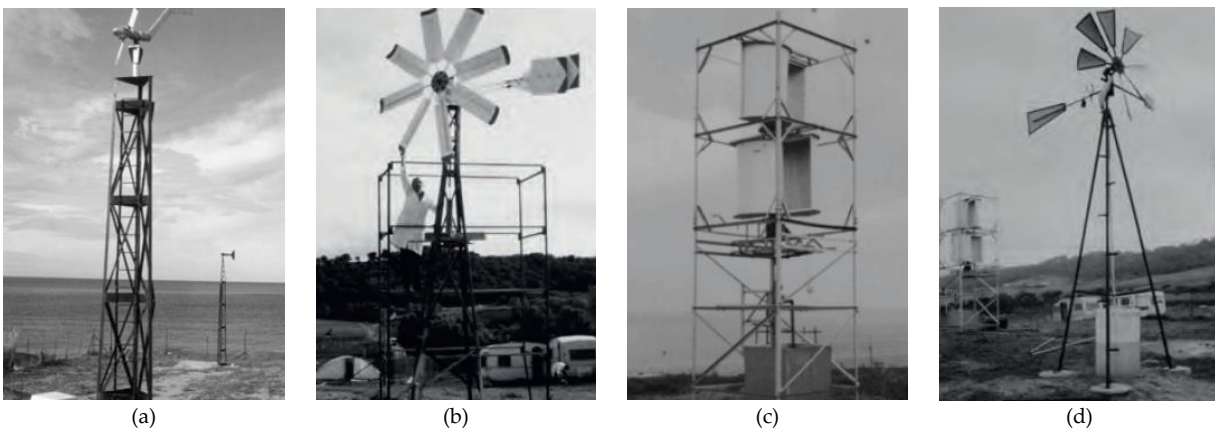


**Figure 1.2** Pumped storage wind turbines studied and developed at CDER (a) small wind turbine (b) "El Hayat" horizontal axis wind pump turbine (c) "Savonius" type 2-stage vertical axis wind pump (d) Horizontal axis wind pump [13].

In Algeria, the largest wind pump was installed in Adrar by the colonization and hydraulics services [14]. Mounted on a 25-metre-high mast, this three-bladed machine with a diameter of 15 meters operated for almost 10 years. More recently, the High Commission for the Development has installed 77 wind turbines for pumping water in the highlands [15]. Following the mechanical incidents encountered with mechanical wind pump, it is generally accepted that for deep boreholes, the wind turbine system coupled to an electric pump is more reliable. However, for such an installation to be effective, the average wind speed must be greater than 4 m/s [16].

Maouedj et al [17] conducted a study on windmills installation. In the first part, the wind energy potential of the Tindouf, Ain Salah and Ain Amenas sites was estimated. In the second part, a wind pumping system consisting of wind turbines of different powers (1 kW, 2 kW and 3 kW) was presented. The analysis of the data revealed several important conclusions, at shallow depths, the flows of pumped water are higher than for greater depths. For similar head gauges (30 m and 60 m), flow rates are higher with wind turbines with higher power ratings. As a result, 1 kW wind turbines can be adapted to shallow wells and limited water requirements, while higher power wind turbines are preferable for deeper wells. In addition, the characteristics of the wind turbine, such as rated power, rated speed, start-up speed and maximum speed, have a significant influence on the useful power generated and thus on the amount of water pumped daily by the system.

Chamlong et al [18] in another study worked on a Multi blade wind turbine that was chosen for its ability to operate at low wind speeds and its economy compared to other types of turbines. This turbine, equipped with 30 blades and a diameter of 4.2 meters, was installed at a height of 12 meters, corresponding to the height of the anemometer during the study. Directly connected to a piston pump via gears, crankshaft and connecting rods, the turbine operated efficiently even at wind speeds as low as 2.5 m/s, keeping its operation between 1.5 and 2 m/s depending on the load. The pump, with a diameter of 0.1 m and a maximum stroke of 0.18 m, could operate with suction heights of up to 6 meters and discharge heads of about 25 meters. Equipped with a water tank and an overflow valve, the system included a flow meter to measure water production in relation to wind speed. Although the efficiency of the system was relatively low, the lack of fuel costs made it economically viable.

Nghi et al [19] this time studied a multi-bladed windmill with 24 blades and a rotor of 4.5 m in diameter was installed at a height of 10 meters. Two pumps were tested: a suction pump with a diameter of 95 mm and a piston pump with a diameter of 45 mm. Two 0.7 m<sup>3</sup> water tanks were placed at a height of 4.3 m to temporarily store water for irrigation and domestic use. The results showed that the suction pump achieved a maximum flow rate of 2.3 m<sup>3</sup>/h at an average wind speed of 4.3 m/s, while the piston pump achieved a maximum flow rate of 0.93 m<sup>3</sup>/h at a wind speed of 4.1 m/s. The average efficiency of the windmill was 20.8%, with a maximum efficiency of 33.3% at a wind speed of 1.7 m/s and a minimum efficiency of 10.1% at 4.1 m/s. The overall efficiencies for the windmill-suction pump and windmill-piston pump combinations were 13.0% and 6.7%, respectively.

The Directorate of Electrical Works of Turkey has developed two wind powered water pumping systems. The first system, located in the administration's renewable

energy resources park, consists of 6 blades and can pump water up to a depth of 7 meters from a height of 5 meters, operating from a wind speed of 3 m/s. The second system, designed and manufactured by the administration, has a 2-metre diameter rotor with 16 blades and can pump water up to a height of 4 meters from a wind speed of 3 m/s [20].

In 2003, in Senegal, Project Alizes was launched to solve problems of access to water in isolated localities, where the supply of diesel, spare parts and maintenance was difficult. These regions were also far from the interconnected electricity grid. In order to meet these needs, the project built 30 pumping systems, including 27 wind turbines and 3 pumps. Water needs in these localities were low (less than 15 m<sup>3</sup>/day) and the populations had limited financial capacities, which made diesel pumping systems expensive both in terms of investment and maintenance [21]. To meet these challenges, three types of wind turbines have been selected: OASIS, FIASA and SSM:

1. OASIS: The Oasis wind turbine, manufactured by Ecolab (ex. Poncelet), is equipped with 15 blades and a direct transmission connecting rod and crank motor. It can be installed on a 10- to 12-meter-high pylon and is designed to pump water to depths of up to 35 meters. Despite its ease of installation and maintenance, it is sensitive to wind speed and static level depth, which can lead to frequent breakdowns. Its total cost, including supply, installation and maintenance, is 2.75 million CFA francs (611750 DA) per year [21].
2. FIASA: FIASA wind turbines, of Argentine origin, are like American mills and have rotor diameters of 2.5 to 4.2 meters. They are equipped with 18 blades and a gear motor with gear ratio. These wind turbines are designed to pump water to depths of up to 35 meters and are suitable for different wind conditions using two possible pump strokes. Although they are very efficient, engine failures can lead to high maintenance costs. The total cost, including supply, installation and maintenance, is about 2.4 million CFA francs (533891 DA) per year [21].
3. SSM: The SSM wind turbines, manufactured by Tuzzie Bardi in Italy and then taken over by LVIA in Senegal, have rotor diameters of 5 to 6 meters. They are equipped with 18 blades and a direct drive connecting rod and crank engine. Designed to pump water to depths of up to 35 meters, they are robust and suitable for harsh environments. However, they are sensitive to wind due to their large size and may require higher maintenance costs due to corrosion of the materials used. The total cost, including supply, installation and maintenance, is about 4.85 million CFA francs (1078904 DA) per year [21].

### 1.3 Operation Theory of Piston pumps

There are two types of pumping units available to the user: slow wind turbines with piston pumps, which currently exist in very large numbers, and fast wind turbines coupled to propeller pumps or centrifugal pumps; these last machines, of recent construction, characterize the evolution of new techniques.

At first glance, it does not seem obvious, and it is not mandatory, that a small-power pumping system should be equipped with a piston pump. But, on the one hand, the importance of the discharge heads, and on the other hand, the need to use simple equipment, generally lead, for small powers, to the use of slow piston pumps.

The wind turbine to be used in this case will be a specific low-speed machine with almost always a gear ratio. This kind of machine has a high starting torque that fits perfectly with the requirements of piston pumps. Since wheels with a specific low speed have many blades, only the use of fixed blades can be envisaged [22].

### **1.3.1 Principle of Operation**

It is one of the most widely used types of pumps. The wind turbine wheel on which blades are attached rotates under the action of the wind. This wheel is fixed on a shaft whose rotational movement is transformed into a reciprocating vertical movement by means of a crank plate or a connecting rod. The back and forth thus creates and drives downwards, through a steel rod, a piston of the water pump, which is generally submerged in the borehole. To drive a reciprocating water pump, high torque is the basic requirement. Multi-blade wind turbines have high strength and a low tip speed ratio, which results in higher starting torque. There are two choices to set our target: The first is to set the desired output of the system and specify all the parameters accordingly. Secondly, it is a question of analyzing the amount of wind energy available on the rotor at a specific location and the production that can be achieved, while considering all impossibilities and losses [22].

### **1.3.2 Operating Conditions of a Slow Wind Turbine with Piston Pump**

It can therefore be seen that, depending on the speed of the wind, it will be necessary to adopt this model of pump. The machine is not called upon to operate for a single value of the wind speed, but for a whole range of speeds, with durations characterized by the speed-duration curve of the region under consideration. Starting from the speed-duration curve and the flow curves as a function of wind speed, it will be easy to determine for each type of pump the total volume of water pumped in the year, as well as the total number of operating hours [23].

Since the piston pump is a constant torque pump (except for irregularities, mentioned above, but in normal operation and taking into account the inertia of the impeller, everything happens as if the machine were absorbing a constant torque), it is

convenient to represent the characteristics of the wind turbine on a torque-speed graph with the wind speed as a parameter [23].

### 1.3.3 Froude Number

The Froude number is the dimensionless parameter of fluid mechanics that appears wherever the effects of inertia and gravity are significant. The last term of equation 1.1 indicates that this is the case for wind turbine piston pumps;  $gh$  being the term of gravity and  $v$  the speed of the wind [24].

If we consider a wind turbine with a shaft-water efficiency  $\eta = \eta_p \eta_{Tr}$ , The net conversion factor for wind power to water is

$$\frac{\text{Water Power}}{\text{Wind Power}} = C_p \eta_p \eta_{Tr} = C_p \eta = \frac{g \rho_w h q}{\frac{1}{2} \rho_a A v^3} = \frac{8 g \rho_w h q}{\pi \rho_a d^2 v^3} \quad (1.1)$$

where  $h$  and  $q$  are respectively the water height and flow capacity,  $v$  is the average wind speed,  $d$  is the diameter of the wind turbine, and  $\rho_a$   $\rho_w$  are the densities of air and water, respectively.

For a piston pump, the water flow averaged over time

$$q = mn V_s \eta_p = mn \gamma d^3 \eta_p \quad (1.2)$$

where  $n$  is the speed of the pump in cycles per second,  $V_s$  is the swept volume of the cylinder,  $\eta_p$  is the efficiency of the piston pump and  $\gamma$  is a geometric factor of the wind pump equal to  $V_s / d^3$ ,  $m$  is equal to 1 for a single-acting unit, 2 for a double-acting unit and  $n_p$  is equal to the number of cylinders for a multi-cylinder unit.

The substitution in equation 1.1 gives

$$C_p \eta_p \eta_{Tr} = \frac{8 g \rho_w h m n_p \gamma}{\pi \rho_a v^3} \eta_p = \frac{8 m \gamma r_n \rho_w \pi d n_t g h}{\pi^2 \rho_a v v^2} \eta_p \quad (1.3)$$

$$C_p = \frac{8 m \gamma r_n \rho_w \pi d n_t g h}{\pi^2 \eta_{Tr} \rho_a v v^2} \quad (1.4)$$

$n_t$  being the number of revolutions per second of the turbine.

Since multi-effect wind pumps are not common, equation 1.4 is simplified by taking  $m=1$

$$C_p = \frac{8 \gamma r_n \rho_w \pi d n_t g h}{\pi^2 \eta_{Tr} \rho_a v v^2} \quad (1.5)$$

Definition of the Froude number of the wind pump,  $Fr$ , as

$$Fr = \frac{v}{\sqrt{gh}} \quad (1.6)$$

and noting that the tip speed ratio  $\lambda = \frac{\pi dn_t}{v}$ , equation 1.6 takes the form

$$C_p = \frac{8}{\pi^2} \frac{\rho_w \gamma r_n}{\rho_a \eta_{Tr} F_r^2} \lambda \quad (1.7)$$

Dividing by the tip speed ratio results in the required dynamic torque coefficient.

$$C_T = \frac{8}{\pi^2} \frac{\rho_w \gamma r_n}{\rho_a \eta_{Tr} F_r^2} \frac{1}{\lambda} \quad (1.8)$$

The concept of the Froude number of the wind pump can now be appreciated and clearly seen as the dimensionless parameter that fully characterizes the operation of the wind pump.

### 1.3.4 The Torque Cycle of a Wind Pump

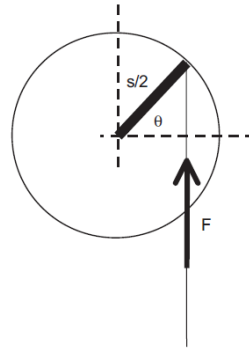


Figure 1.3 The configuration of the crank [24].

Given the torque that the wind pump must exert on the water column, Figure 1.3 shows the crank mechanism schematically. The momentary torque at any angle  $\theta$  is [24]

$$T = (\rho_w gh A_p) \left( \frac{s}{2} \cos(\theta) \right) \quad (1.9)$$

Where  $\rho_w$  is the density of water,  $g$  is the acceleration due to gravity,  $h$  is the column of water above the piston,  $A_p$  is the area of the piston head, and  $s$  is the stroke.

This can be expressed as follows:

$$T = A \cos(\theta) \quad (1.10)$$

where  $A$  is a computable constant equal to  $\frac{1}{2} \rho_w gh V_s$ , where  $V_s$  is the swept volume of the piston. The torque-angle profile of a single-acting pump would resemble that in Figure 1.4.

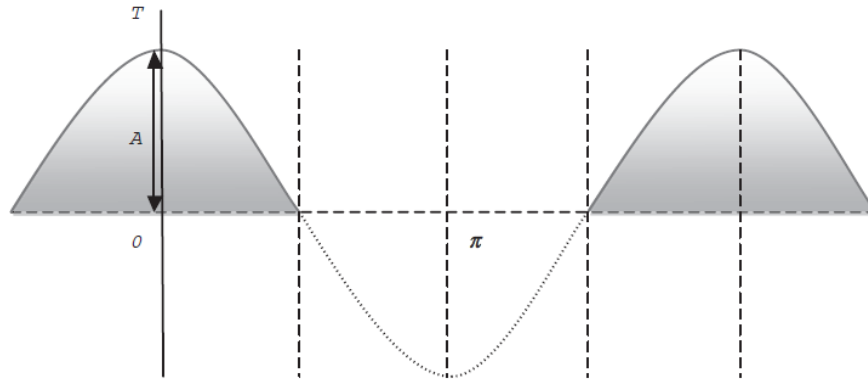


**Figure 1.4** Moment Cycle for a Single Acting Pump [24].

The maximum torque that the wind turbine can experience due to the water column is  $A$ . The average torque can be obtained by integrating the torque expression, equation 1.10, across a range of angles and dividing by the range. The result for the average torque is  $A/\pi$ .

## 1.4 Methodology of the Blade Element Momentum Theory

### 1.4.1 Axial Momentum Theory

The basic aerodynamic model of flow is described by the concept of the actuator disk in wind turbines. This model considers a control volume, in which the boundaries are the lateral surface of a streamtube and the cross-sections of the tube in Figure 1.5 where the flow is assumed to be one-dimensional. The actuator disk creates a discontinuity in the pressure of the air flowing through the streamtube. The theory is based on the following assumptions

- Homogeneous, incompressible flow and steady state.
- Neglected friction and drag.
- Infinite number of blades.
- The wake is assumed to be non-rotational.
- The static pressures of the flow far downstream and upstream are considered equal.

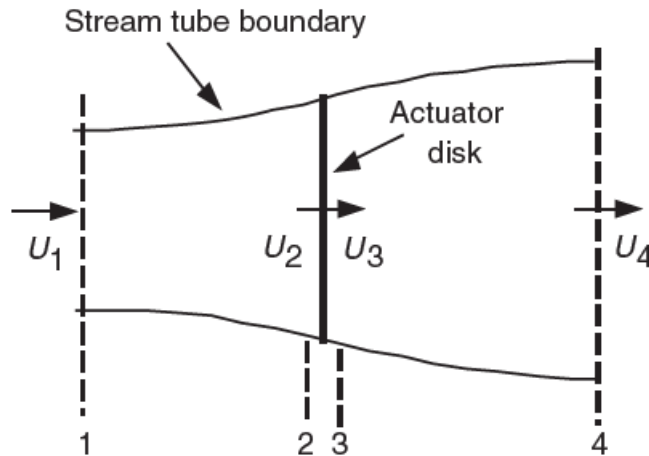


Figure 1.5 An actuator disk [25].

If  $A_2$  is the surface of the actuator disk,  $A_1$  and  $A_4$  the surfaces of the upstream and downstream cross-sections of the streamtube,  $U_1$ ,  $U_2$ , and  $U_4$  are the velocities of the flow upstream, at the actuator disk, and downstream respectively, and  $\rho$  is the density of the air, then the conservation of the mass flow through the streamtube will be

$$\dot{m} = \rho U_1 A_1 = \rho U_2 A_d = \rho U A \quad (1.11)$$

The thrust force is given by

$$T = \dot{m} (U_1 - U_4) \quad (1.12)$$

Bernoulli's equation upstream of the actuator disk gives

$$p_1 + \frac{1}{2} \rho U_1^2 = p_2 + \frac{1}{2} \rho U_2^2 \quad (1.13)$$

The same goes for the flow downstream of the disk

$$p_3 + \frac{1}{2} \rho U_3^2 = p_4 + \frac{1}{2} \rho U_4^2 \quad (1.14)$$

The thrust can also be expressed as the net sum of the forces on each side of the actuator disk

$$T = A_d (p_2 - p_3) \quad (1.15)$$

From Bernoulli's equations 1.13 and 1.14, taking into account the assumptions of the actuator disk, ( $U_2 = U_3$ ) et ( $p_1 = p_4$ ), the thrust is then

$$T = \frac{1}{2} \rho A_d (U_1^2 - U_4^2) \quad (1.16)$$

So from equations 1.12 and 1.16 and considering the conservation of the mass flow in equation 1.11, we can therefore derive the following equality

$$U_2 = \frac{U_1 + U_4}{2} \quad (1.17)$$

The actuator disk induces a velocity in the streamtube. The difference between  $U_1$  and  $U_2$  is called the induced axial velocity. This velocity is represented by a dimensionless factor called the axial induction factor  $a$

$$a = \frac{U_1 - U_2}{U_1} \quad (1.18)$$

The flow velocity at the level of the actuator disk and downstream can therefore be expressed as follows

$$U_2 = U_1(1 - a) \quad (1.19)$$

$$U_4 = U_1(1 - 2a) \quad (1.20)$$

Finally, from equations 1.16, 1.19 and 1.20, by setting the flow velocity far upstream  $U$  and the surface area of the actuator disk  $A$ , the axial thrust of the actuator disk is therefore given as follows

$$T = \frac{1}{2} \rho A U^2 4a(1 - a) \quad (1.21)$$

The aerodynamic output power of the rotor,  $P$ , is equal to the thrust force  $T$  multiplied by the velocity of the flow at the disc, which gives from equations 1.19 and 1.20

$$P = \frac{1}{2} \rho A U^3 4a(1 - a)^2 \quad (1.22)$$

The power coefficient is defined by the ratio of the extracted power to the power available in the wind

$$C_p = \frac{\text{Rotor power}}{\text{Power in wind}} = \frac{P}{\frac{1}{2} \rho A U^3} = 4a(1 - a)^2 \quad (1.23)$$

The maximum of  $C_p$  is determined by differentiating its expression according to the axial induction factor  $a$ , and by equalizing the derivative to 0, which gives us a factor  $a = 1/3$  therefore

$$C_{p \max} = \frac{16}{27} \quad (1.24)$$

This limit is known as: Betz Limit.

Similar to power, thrust can be expressed using a dimensionless thrust coefficient

$$C_T = \frac{T}{\frac{1}{2} \rho A U^2} \quad (1.25)$$

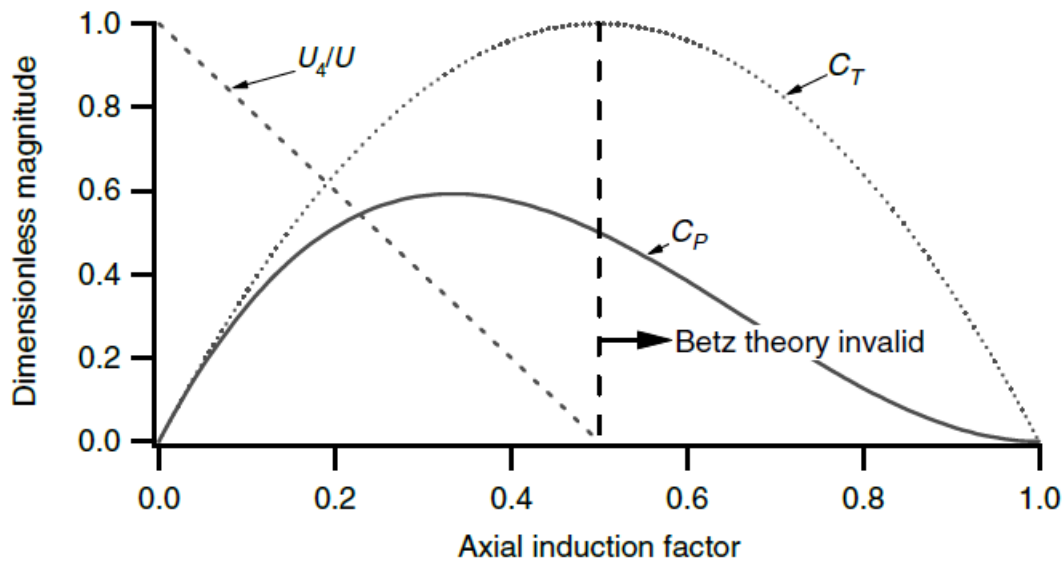


Figure 1.6 Dimensionless power and thrust coefficients as a function of axial induction coefficient [25].

### 1.4.2 Ideal horizontal axis turbine with wake rotation

In the previous analysis, the rotor was considered to be a simple disc with no rotational speed in order to assume a one-dimensional airflow. In the case of a rotating turbine, the flow of air flow downstream of the rotor will rotate in a direction opposite to that of the rotor, as opposed to the rotational torque generated by the rotor. This is the wake rotation as shown in Figure 1.7.

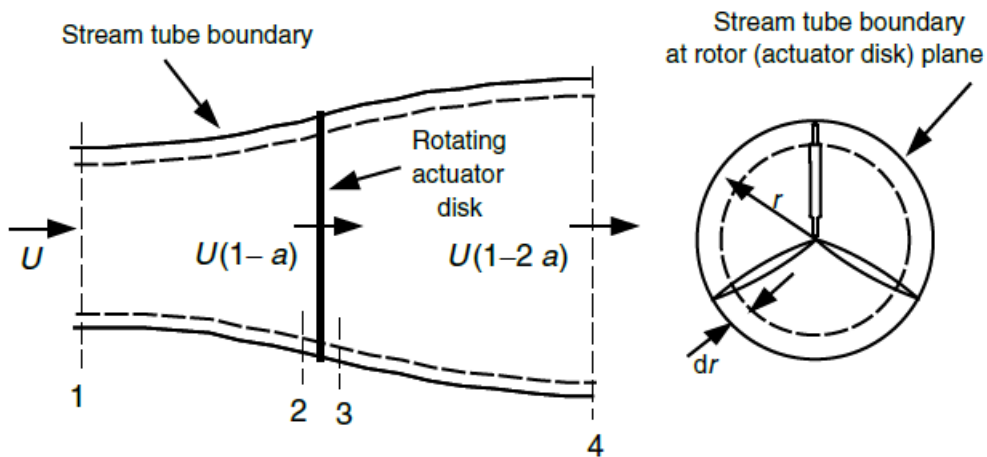


Figure 1.7 Rotor analysis geometry [25].

The angular velocity of rotation of the wake is lower than that of the rotor. Assuming a control volume with a rotation equal to that of the blades, and applying the energy

conservation equation, Glauert [26] was able to determine the pressure difference at the turbine by noting that the axial velocity of the air remains constant, and that this tangential component increases from  $\Omega$  to  $\omega + \Omega$

$$p_2 - p_3 = \rho\left(\Omega + \frac{1}{2}\omega\right)\omega r^2 \quad (1.26)$$

From equations 1.15 to 1.26, the elementary thrust is

$$dT = \left[\rho\left(\Omega + \frac{1}{2}\omega\right)\omega r^2\right] 2\pi r dr \quad (1.27)$$

The angular or tangential induction factor is defined by

$$a' = \frac{\omega}{2\Omega} \quad (1.28)$$

If the wake rotation is taken into account in the analysis, the induced velocity is no longer only axial  $a$ , but also has a tangential component  $a'$ . The elementary thrust can then be expressed as follows

$$dT = \rho\Omega^2 r^2 [4a'(1 + a')] \pi r dr \quad (1.29)$$

Identifying this expression with the one found using axial momentum theory for thrust equation 1.27 in the case of an annular element, we obtain the following parameter

$$\frac{a(1 - a)}{a'(1 + a')} = \frac{\Omega^2 r^2}{U^2} = \lambda_r^2 \quad (1.30)$$

Where  $\lambda_r$  is the local Tip Speed Ratio (TSR). The overall  $\lambda$  is defined as follows

$$\lambda = \frac{\Omega R}{U} \quad (1.31)$$

The torque exerted on the rotor Q is equal to the variation of the angular momentum of the wake, for an annular element this gives

$$dQ = d\dot{m}(\omega r)(r) = (\rho U_2 2\pi r dr)(\omega r)(r) \quad (1.32)$$

Taking equations 1.9 and 1.32 the expression of the pair then becomes

$$dQ = \rho U \Omega r^2 [4a'(1 - a)] \pi r dr \quad (1.33)$$

The power generated at each element is related to the torque by the following formula

$$dP = \Omega dQ \quad (1.34)$$

### 1.4.3 Aerodynamic forces

The airflow will generate a distribution of force on the airfoil. When the flow passes on the convex side of the airfoil, the airflow will tend to accelerate, which will have the effect of reducing the pressure on this surface. Conversely, the flow velocity on the concave

side will decrease causing an increase in pressure. This pressure difference on both sides of the airfoil will then create the lift force  $F_l$  perpendicular to the direction of flow. In addition, the contact between the air and the surface of the airfoil will cause friction with the effect of reducing speed. This friction results in the drag force  $F_d$  in the opposite direction to the direction of flow. Both of these forces depend on the relative wind speed perceived by the blade. In the case where wake rotation is taken into account, the speed at the rotor will have two components: the axial component given in equation 1.9. As for the tangential component, it will be equal to the sum of the rotational speed of the blade  $\Omega r$  and that of the wake  $\omega r/2$ , which gives

$$\Omega r + \frac{\omega}{2} r = \Omega r + \Omega a' r = \Omega r(1 + a') \quad (1.35)$$

The two lift and drag forces acting on the airfoil of a blade along a length  $r$  and chord  $c$  are

$$F_l = \frac{1}{2} C_l \rho U_{rel}^2 c r \quad (1.36)$$

$$F_d = \frac{1}{2} C_d \rho U_{rel}^2 c r \quad (1.37)$$

With  $U_{rel}$ , the wind speed seen through the blade. These two equations are a function of two dimensionless parameters: the lift coefficient  $2D C_l$  and the drag coefficient  $2D C_d$ . These two coefficients depend on the angle of attack  $\alpha$ , as well as on the Reynolds number  $Re$

$$Re = \frac{U_{rel} c}{\nu} \quad (1.38)$$

These coefficients are called two-dimensional because they are obtained from flow simulations on the two-dimensional shape of the airfoil. It's possible to obtain these coefficients in wind tunnel experiments or with the help of dedicated software.

#### 1.4.4 Viterna Extrapolation

Experiments and prediction codes for lift coefficients  $C_l$  and drag  $C_d$  can only give results for a small range of angles of attack values  $\alpha$  around the stall area. It is necessary to be able to predict these coefficients over a wider range when calculating the BEM theory. Extrapolation from Viterna (1982) is the most widely used method for predicting aerodynamic coefficient values. Viterna extrapolation allows the data to be extrapolated beyond the stall angle  $\alpha_{stall}$  [27] to an angle of attack less than or equal to  $90^\circ$ .

The lift and drag coefficients are extrapolated using the following relationships:

$$C_l = A_1 \sin 2\alpha + A_2 \frac{\cos^2 \alpha}{\sin \alpha} \quad (1.39)$$

$$C_d = B_1 \sin^2 \alpha + B_2 \cos \alpha \quad (1.40)$$

With

$$C_{d \max} \approx 1.11 + 0.018 AR \quad (1.41)$$

$$A_1 = \frac{C_{d \max}}{2} \quad (1.42)$$

$$B_1 = C_{d \max} \quad (1.43)$$

$$A_2 = (C_{l \text{ stall}} - C_{d \max} \sin \alpha_{\text{stall}} \cos \alpha_{\text{stall}}) \frac{\sin \alpha_{\text{stall}}}{\cos^2 \alpha_{\text{stall}}} \quad (1.44)$$

$$B_2 = \frac{C_{d \text{ stall}} - C_{d \max} \sin^2 \alpha_{\text{stall}}}{\cos \alpha_{\text{stall}}} \quad (1.45)$$

With  $\alpha_{\text{stall}}$ ,  $C_{l \text{ stall}}$  and  $C_{d \text{ stall}}$  the values of the angle of attack, lift coefficients and drag at the time of stalling.  $AR$  is the aspect ratio, it can be taken between 0 and 50 and will have a slight effect on the extrapolated curve.

For a complete extrapolation from  $-180^\circ$  to  $180^\circ$ , the airfoil is assumed to act as a flat plate described by the following equations

$$C_l = 2 \sin \alpha \cos \alpha \quad (1.46)$$

$$C_d = 2 \sin^2 \alpha \quad (1.47)$$

### 1.4.5 3D Correction

When the wind turbine is in operation, the variation in wind speed associated with the rotation of the blade causes a variation in the relative speed acting on the blades. This rotation has an effect on the boundary layer that is not taken into account in the static simulations of the  $2D$   $C_l$  and  $C_d$  coefficients. This phenomenon is called static stall, the effect of which is observed in the stall zone, where the boundary layer experiences a delay in stall (Stall-Delay). The  $2D$  aerodynamic coefficients are therefore underestimated in the stall zone. In order to correct this difference, several empirical models have been developed to approximate the  $3D$  boundary layer.

### 1.4.5.1 3D correction by Du and Selig [28]

For the cross-section of a chord airfoil  $c$  at a distance  $r$  from the center of a rotor with a radius  $R$  of Rotational speed and at a wind speed  $U$ , the corrected coefficients  $C_{l,3D}$  and  $C_{d,3D}$  are given by:

$$C_{l,3D} = C_{l,2D} + \Delta C_l \quad (1.48)$$

$$C_{d,3D} = C_{d,2D} - \Delta C_d \quad (1.49)$$

With

$$\Delta C_l = f_l(C_{l,p} - C_{l,2D}) \quad (1.50)$$

$$\Delta C_d = f_d(C_{d,2D} - C_{d,0}) \quad (1.51)$$

Where:  $C_{l,p} = 2\pi (\alpha - \alpha_0)$ ,  $\alpha_0 = \alpha$  for  $C_{l,2D} = 0$  and  $C_{d,0} = C_{d,2D}$  for  $\alpha = 0$ .  
Factors  $f_l$  et  $f_d$  are

$$f_l = \frac{1}{2\pi} \left[ \frac{1.6 \left(\frac{c}{r}\right) a - \left(\frac{c}{r}\right) \frac{dR}{\Gamma r}}{0.1267b + \left(\frac{c}{r}\right) \frac{dR}{\Gamma r}} - 1 \right] \quad (1.52)$$

$$f_d = \frac{1}{2\pi} \left[ \frac{1.6 \left(\frac{c}{r}\right) a - \left(\frac{c}{r}\right) \frac{dR}{2\Gamma r}}{0.1267b + \left(\frac{c}{r}\right) \frac{dR}{2\Gamma r}} - 1 \right] \quad (1.53)$$

$$\Gamma = \frac{\Omega R}{\sqrt{U^2 + (\Omega R)^2}} \quad (1.54)$$

With  $a$ ,  $b$  and  $d$  empirical factors generally taken equal to 1.

### 1.4.5.2 3D Correction of Corrigan–Schilling [29]

The 3D correction is performed only on the lift coefficient  $C_{l,3D}$

$$C_{l,3D} = C_{l,2D} + a\Delta\alpha \quad (1.55)$$

$$\Delta\alpha = (\alpha_{c_{l,max}} - \alpha_{c_{l=0}}) \left[ \left( \frac{K\theta_{TE}}{0.136} \right)^n - 1 \right] \quad (1.56)$$

$$\Delta\alpha = \left( \frac{c/r}{0.1517} \right)^{-\frac{1}{1.084}} \quad (1.57)$$

With  $a$  the tangent of the curve  $C_l$  vs  $\alpha$  for  $C_l = 0$ ,  $\alpha_{C_{l,max}}$  the angle of attack for the maximum lift coefficient (at static stall),  $\theta_{TE}$  represents a polar angle equal to the ratio  $c/r$  and  $n$  an empirical factor to be taken between 0.8 and 1.6.

### 1.4.6 Blade Element Momentum Theory

The axial momentum theory describes a mathematical model of an ideal actuator disk using the principles of linear and angular conservation of momentum. The blade element theory, on the other hand, refers to the analysis of forces at a section of the blade. These two approaches combined give the Blade Element Momentum Theory (BEM).

For each element, the forces are calculated on the 2D sections to determine lift, drag, thrust, torque and therefore power. The equations are then obtained according to the triangle of forces.

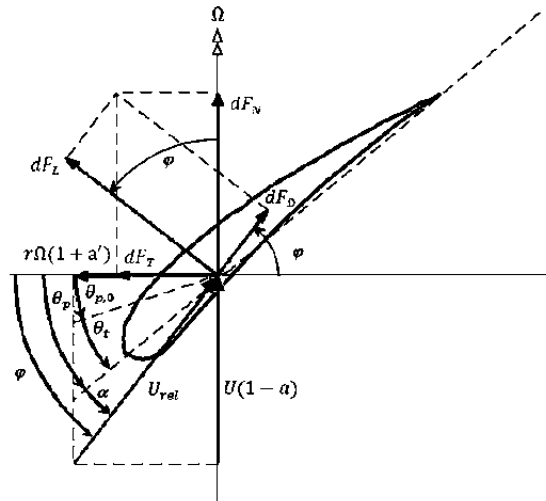


Figure 1.8 Blade geometry for the analysis of a horizontal axis wind turbine [25].

$$\varphi = \alpha + (\theta_t + \theta_p) = \alpha + \theta \quad (1.58)$$

It then appears from the triangle of velocities

$$\tan \varphi = \frac{U(1-a)}{\Omega r(1+a')} = \frac{1-a}{(1+a')\lambda_r} \quad (1.59)$$

$$U_{rel} = \frac{U(1-a)}{\sin \varphi} = \sqrt{(U(1-a))^2 + (\Omega r(1+a'))^2} \quad (1.60)$$

We can also derive the formulas for the elementary normal and tangential forces  $dF_n$  and  $dF_t$  as a function of the elementary lift and drag forces  $dF_l$  and  $dF_d$  (equations 1.52 and 1.53):

$$dF_t = \frac{1}{2} \rho U_{rel}^2 (C_l \sin \varphi - C_d \cos \varphi) c dr \quad (1.61)$$

$$dF_n = \frac{1}{2} \rho U_{rel}^2 (C_l \cos \varphi + C_d \sin \varphi) c dr \quad (1.62)$$

Finally, for a wind turbine with a number of blades  $B$ , the formulas for thrust, torque and elementary power for an annular cross-section:  $dT$ ,  $dQ$  and  $dP$  by the BEM theory are:

$$dT = B dF_n = B \frac{1}{2} \rho U_{rel}^2 (C_l \cos \varphi + C_d \sin \varphi) c dr \quad (1.63)$$

$$dQ = Br dF_t = B \frac{1}{2} \rho U_{rel}^2 (C_l \sin \varphi - C_d \cos \varphi) c r dr \quad (1.64)$$

$$dP = \Omega dQ = \Omega B \frac{1}{2} \rho U_{rel}^2 (C_l \sin \varphi - C_d \cos \varphi) c r dr \quad (1.65)$$

#### 1.4.7 Development of the BEM Performance Prediction Algorithm

The algorithm based on BEM theory allows to determine the aerodynamic performance of a wind turbine using an iterative calculation to calculate the axial and tangential induction factors  $a$  and  $a'$  until they converge to implement them in the equations mentioned in section 1.4.6. Power, torque and total thrust will be obtained by summing the elements. The calculation will be made for each element and for each operating speed of the wind turbine:

1. Calculate for each element and for each speed the local solidity and the local TSR

$$\sigma = \frac{Bc}{2\pi r} \quad (1.66)$$

2. Initializing the  $a$  and  $a'$  factors to 0

$$\lambda_r = \frac{\Omega r}{U} \quad (1.67)$$

3. Calculation of the relative wind angle as well as the angle of attack

$$\varphi = \tan^{-1} \left( \frac{1 - a}{\lambda_r (1 + a')} \right) \quad (1.68)$$

$$\alpha = \varphi - (\theta_t + \theta_p) \quad (1.69)$$

4. Determination of the lift and drag coefficients  $C_l$   $C_d$  corresponding to the angle of attack  $\alpha$ , extrapolation of the data by Viterna and then 3D correction.
5. Determination of the normal and tangential coefficients:

$$C_n = C_l \cos \varphi + C_d \sin \varphi \quad (1.70)$$

$$C_t = C_l \sin \varphi - C_d \cos \varphi \quad (1.71)$$

6. Correction of losses at the tip and hub

$$F_{tip} = \frac{2}{\pi} \cos^{-1} \left( e^{-\frac{B}{2} \frac{R-r}{r \sin \varphi}} \right) \quad (1.72)$$

$$F_{hub} = \frac{2}{\pi} \cos^{-1} \left( e^{-\frac{B}{2} \frac{r-R_{hub}}{r \sin \varphi}} \right) \quad (1.73)$$

$$F = F_{tip} \times F_{hub} \quad (1.74)$$

7. Local thrust coefficient

$$C_{Tr} = \frac{\sigma(1-a)^2 C_n}{\sin^2 \varphi} \quad (1.75)$$

8. Calculation of axial and tangential induction factors:

When the axial induction factor  $a$  is greater than 0.4, the assumptions of the BEM theory are invalid, which requires correction. We will then use Buhl's correction [30].

$$\begin{cases} a = \left[ 1 + \frac{4F \sin^2 \varphi}{\sigma C_n} \right]^{-1} & \text{if } C_{Tr} \leq 0.96F \\ a = \frac{18F - 20 - 3\sqrt{C_{Tr}(50 - 36F) + 12F(3F - 4)}}{30F - 50} & \text{if } C_{Tr} > 0.96F \end{cases} \quad (1.76)$$

$$a' = \left[ -1 + \frac{4F \sin \varphi \cos \varphi}{\sigma C_t} \right]^{-1} \quad (1.77)$$

9. Repeat calculations 3 to 8 until factors  $a$  and  $a'$  converge at a given tolerance

10. Calculation of thrust, torque and power for each element and speed (equations 1.58, 1.59 and 1.60)

11. Calculation of torque, thrust and total turbine power

$$\begin{cases} T = \sum dT \\ Q = \sum dQ \\ P = \sum \Omega dQ \end{cases} \quad (1.78)$$

## 1.5 Problematic

A common wind pump with several blades usefully supplies about 4% to 8% of

the annual wind power passing through the swept area [28,29]. This low conversion is due to poor load matching between wind rotors and fixed-stroke piston pumps. The main limitation is due to the very nature of the piston pump, which causes several problems. Additionally, the purely mechanical system necessitates a complex assembly involving numerous parts and mechanical connections. This complexity leads to exorbitant manufacturing costs, extended construction times, and a higher likelihood of various breakdowns. Consequently, regular maintenance is essential to ensure the system's functionality, making it less efficient compared to electric wind pumps.

### 1.6 Objective

The objective of this work is to foster innovation among polytechnic engineers using modern methods of optimization, analysis, and study, specifically within the field of wind turbines. Several goals have been established, with the primary aim being to reduce both manufacturing and maintenance costs by minimizing the number of components. Utilizing advanced mathematical tools and the latest research, this work emphasizes the optimization of wind turbines and piston pumps. To validate the performance of the final design, a CFD numerical simulation will be conducted, and a scale model based on the principle of similarity will be fabricated and tested. In the figure below is a summary of the different aspects dealt with in this study:

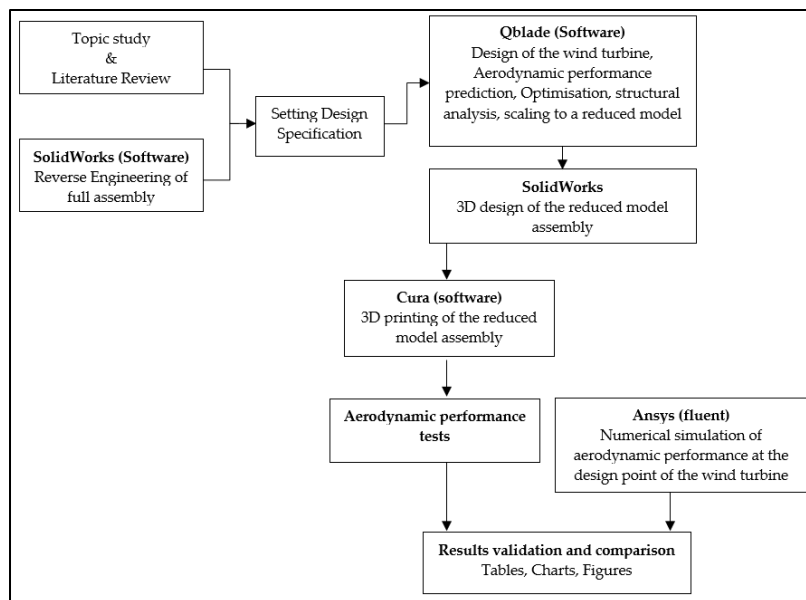


Figure 1.10 Brief roadmap of the work.

# Chapter 2

## Design and Modeling

### 2.1 Introduction

This study was based on the reverse engineering of a windmill located at the POVAL company in Medea. It aimed to optimize the design of the wind turbine, piston pump, and transmission system. The wind turbine's design is critical as it is the machine's core component. It depends on numerous parameters and conditions, including the number of blades, rotor diameter, and blade surface area. Even minor changes in speed or diameter can drastically alter the power output. The piston pump's performance is defined by the piston stroke and diameter, with its configuration greatly impacting the desired height and flow rate.

### 2.2 Reverse engineering

At a higher level of engineering, there are two types of engineering: direct engineering and reverse engineering. Direct engineering is the traditional process of moving from high-level abstractions and logical designs to the physical implementation of a system. Reverse engineering is the process of duplicating a component without the help of drawings, documentation, or computer models [31].

In our project, we reverse-engineered an existing wind pump model without

having the original technical drawings. Instead, we took the necessary dimensions from the wind pump itself, which had been in use for about forty years, relying on the technical documents available from that time. During our investigation, we discovered a similar type of windmill, the WP-2, developed for moderately windy sites at the National Aeronautical Laboratory (NAL) in Bangalore [32]. Between 1959 and 1964, NAL indigenously developed and produced the WP-2 windmills in batches, erecting 80 units for field trials across various locations in India. These windmills were primarily used for lifting water for domestic and minor irrigation purposes. Figure 2.1 shows the WP-2 type windmill.

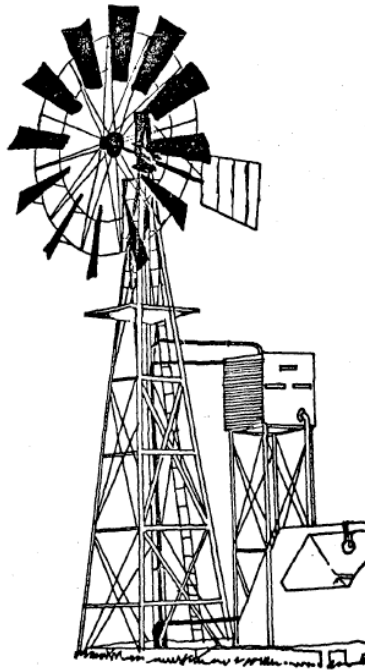


**Figure 2.1** WP-2 Windmill [32].

The rotor is 4 m in diameter. The rotor spiders are fabricated out of galvanised pipe. These are strengthened with tie rods which are kept in tension by means of adjustable eye bolts [32]. Fittings are provided over the pipes and angles to fix the rings and blades. Two rings are fabricated, each of diameter 2.7 m and 4 meter and these form the support for the blades as shown in Figure 2.2.

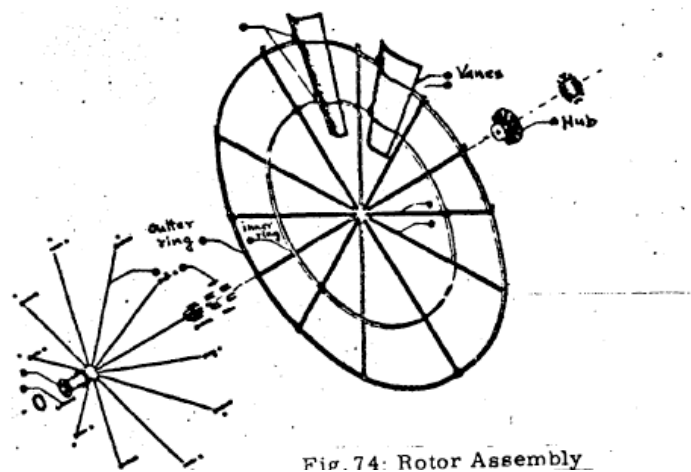


Figure 2.2 Rotor Assembly [32].

The tail vane in Figure 2.3, is fabricated from galvanized plain sheet. The rotor pipes and angles are rigidly fixed to a cast iron hub. A pipe fabricated from sheet tube with two mild steel flanges is provided as an extension to the hub to which the tie rods are fixed [32]. The hole in the hub for the shaft is 0.5 m in diameter.

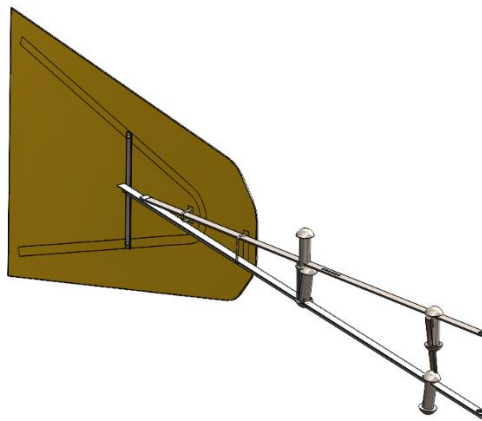
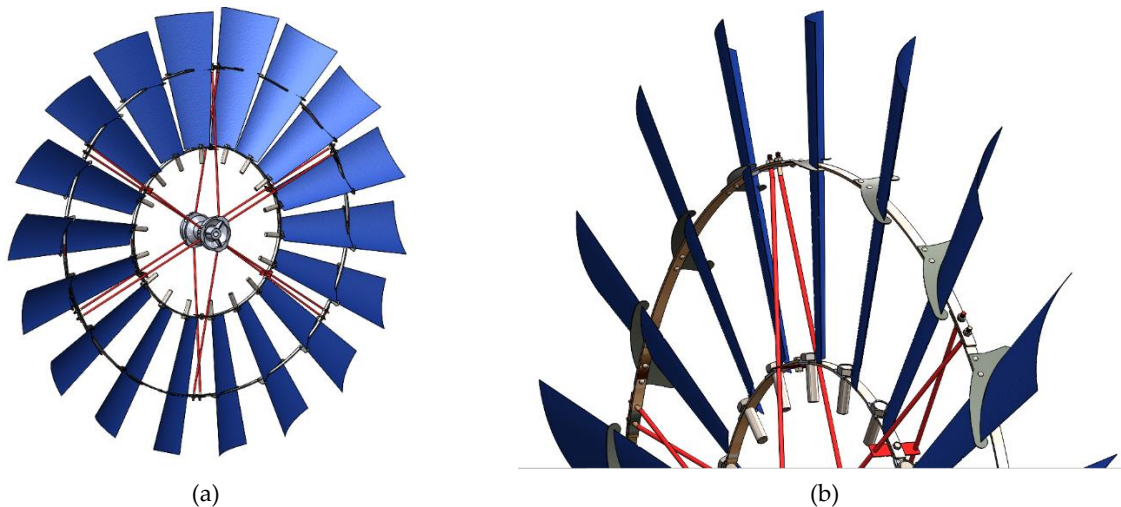


Figure 2.3 Reverse Engineering of Tail Vane.

There are 16 blades made of galvanized plain sheets shown in Figure 2.4. To stiffen the blades and to maintain the shape, a framework is made out of flat sections and fabricated angles. The inner and outer leading edges of the vanes are set at  $45^\circ$  and  $35^\circ$  respectively to the plane of the rotor such that the rpm does not go beyond 40 at greater wind speed. The inclination is maintained by the vane fittings. The blades are fixed to the rotor ring with vane fittings that are fabricated out of angle sections. Each blade can be easily fixed or removed independently.



**Figure 2.4** Reverse engineering of the wind turbine.

The pumps used for windmills are of single-acting piston type pump with a brass cylinder. There are two sizes of pumps of similar design with cylinders of 15 cm and 10 cm diameter. The small pump is for use where the depth of the well is more or where there is a possibility of the well getting drained by the continuous working of the windmill. The pump comprises of cylinder, plunger, suction valve, top and bottom plate as shown in Figure 2.5.

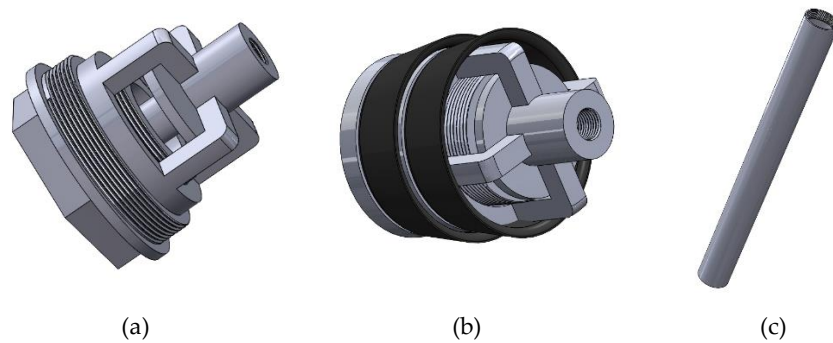


**Figure 2.5** Reverse engineering of the piston pump (a) suction valve (b) discharge valve (c) cylinder

The transmission system of a windpump is responsible for converting the rotational energy of the wind turbine into mechanical energy that can drive a water pump. The gearbox in Figure 2.6-a adjusts the rotational speed and increase the torque of the main shaft to the appropriate speed required by the pump. Gearboxes can be simple or complex, depending on the specific requirements of the windpump system. The crankshaft converts the rotational motion from the gearbox into reciprocating motion, which is necessary for the operation of a piston pump. It typically consists of a crank and a connecting rod as shown in Figure 2.6-b. As the crankshaft rotates, the connecting rod translates this motion into a back-and-forth motion for the piston.

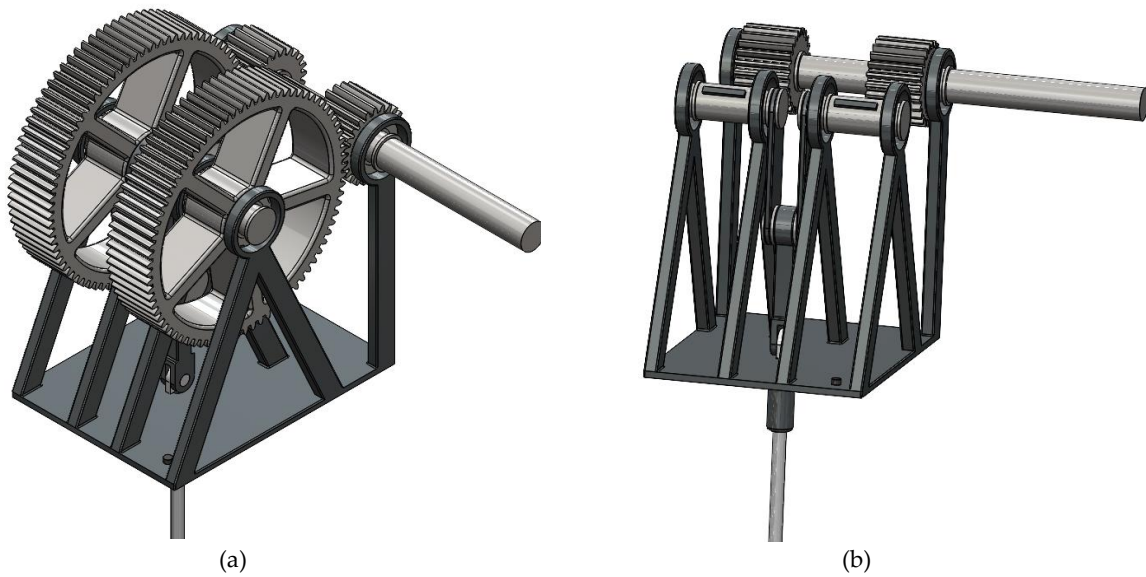


**Figure 2.6** Transmission system.

The steel tower, depicted in Figure 2.7, stands 10 meters above ground and is built in three sections for easier erection. Each section is reinforced with angle-back pieces bolted together, enhancing strength and reducing strain on the joints. The tower features heavy angle steel legs and cross braces, spaced every 1.5 meter, for added stability. A ladder and a hardwood platform, supported by steel angles, provide accessibility for maintenance.



**Figure 2.7** Reverse engineering of the tower.

The windmill is basically made of steel and uses a slightly complicated mechanism. Also, the cost of fabrication is considerable, which may be beyond the reach

of the individual farmers [32]. In Table 2.1 main parts are summarized.

**Table 2.1** Different Parts of the Windmill.

Part Number	Part Name
1	Rotor Spiders
2	Rotor Rings
3	Rotor Pipes
4	Blades
5	Turn table
6	Shaft
7	Crank
8	Connecting rod
9	Piston pump
10	Tower
11	Tail Vane
12	Braking system

## 2.3 Wind turbine design

### 2.3.1 General considerations

Table 2.2 shows the different considerations regarding selection of suitable tip speed ratio. If the tip speed is high, low chord length is required which reduces the blade dimensions and material used. But higher tip speed ratio increases the aerodynamic and centrifugal frictional loss. To reach some conclusion, we have to fix some parameters like rotor size.

**Table 2.2** Wind turbines design characteristics [33].

<b>Tip speed ratio</b>	1-2	>10
<b>Torque</b>	High	Low
<b>RPM</b>	Low	High
<b>Uses</b>	Included multi-bladed windmills and rotors	2-3 bladed wind turbines, suitable for generators for electricity production
<b>Efficiency</b>	Low because of rotational wake due to relatively high torque of windmill	High up to 40% relative to Betz limit
<b>Solidity</b>	High and contains 12,16,18 or 24 blades	low, mostly 2 or 3 blades
<b>Blade design</b>	Simple design, large curved blades	Design considerations are very crucial
<b>Noise</b>	Low due to low rotation and less sliding parts	Noise is relatively high
<b>Frictional losses</b>	Low due to low rotational speed	Increased as rotational speed

Water pumping windmills characteristically start under load. This requires high torque, realized mainly by increasing blade number or solidity which can be in the region of 0.5–0.8 for the American windmill compared with that of conventional wind turbines given in Table 2.3.

**Table 2.3** Qualitative comparison of horizontal axis rotor types [34].

Type	Starting Torque	Speed	Fabrication Method	Power Coefficient	Solidity (%)
Cretan sail or flat paddles	Medium	Low	Simple	0.05-0.15	50
Cambered plate fan	High	Low	Moderate	0.15-0.30	50-80
Moderate speed wind turbine	Low	Moderate	Moderate	0.2-0.35	5-10
Modern wind turbine	Almost zero	High	Precise	0.30-0.45	5

### 2.3.2 Solidity

The concept of wind rotor solidity is described as the ratio of the total area of the wind turbine blades to the area of the wind passing the wind rotor. For calculation

purposes, blades are considered flat because radius of curvature is much larger as compared with arc length

$$\sigma = \frac{B \cdot A_{blade}}{A} \tag{2.1}$$

$$A_{blade} = \frac{1}{2} L_B (L_{chord1} + L_{chord2}) \tag{2.2}$$

Solidity  $\sigma$  ranges between 0 and 1. For a windmill used for water pumping, value of solidity is high to achieve high starting torque. For that purpose, condition of  $\sigma = 0.8$  must be met for the smooth operation of the system [33].

Figure 2.8 is a schematic diagram of several horizontal axis wind turbine rotor with four kinds of rotors of single blade, double blades, three blades and multiple blades. The solid ratio of the wind rotor from single blade to three blades is small, which is a low solid wind rotor and the rotor has a high solidity ratio of 12 blades, which is a high solid wind rotor.

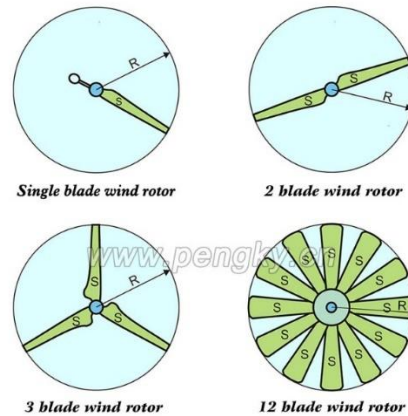


Figure 2.8 Single blade to multi blades wind rotor solidity [35].

The lower part of Figure 2.9 is a schematic diagram of the air flow through the multi-blade (high-solid) wind rotor. The multi-blade greatly increases the resistance of the air passage. A part of the air flow will bypass the blade rotor flow to the rear [35]. This part of the air flow does not work through the blade rotor, so the actual wind energy obtained by the blade rotor is reduced, which is an important reason why multi-blade the wind turbine can't get more wind energy.

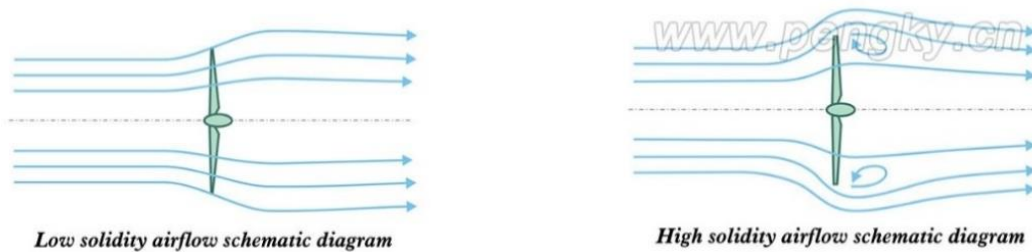


Figure 2.9 Schematic diagram of three-blade and multi-blade airflow [35].

### 2.3.3 Blade number effect

Increasing the number of blades allows for minimal improvements and sacrifices too much blade rigidity as the blades become thinner. Generally, the lower the number of blades, the lower the material and manufacturing costs [36].

Effect of wake rotation on maximum power coefficient: Torque is generated by forces acting tangentially on the blades, resulting from changes in air velocity. The direction of air velocity change opposes the forces on the blades, causing wake rotation opposite to the rotor's direction, leading to energy loss. High torque requires low tip-speed ratios, resulting in large tangential velocities in the wake and thus greater energy loss and lower power [37].

The number of blades also affects the maximum power coefficient. This is caused by the tip-losses that occur at the tips of the blades. These losses depend on the number of blades and the tip-speed ratio [37].

It was evident that increasing the number of blades enhances solidity, resulting in higher starting torque, while decreasing the number of blades minimizes power losses, leading to higher power output. We conducted three BEM simulations at a wind speed of 6 m/s, including tip loss and 3D correction, with a fixed pitch angle of zero. The results were consistent with previous studies. As shown in Figure 2.10, wind turbines with 16 blades have high torque coefficient at lower TSR, with the  $C_m$ -curve falling below that of the 12-blade configuration after a TSR of 0.8. Additionally, the power coefficient  $C_p$  for the 16-blade turbines is higher within a narrow range of TSRs but still has the lowest  $C_p$  peak. In this study,  $C_p$  parameter was more important and more explanation will be conducted in the piston pump optimization section just below.

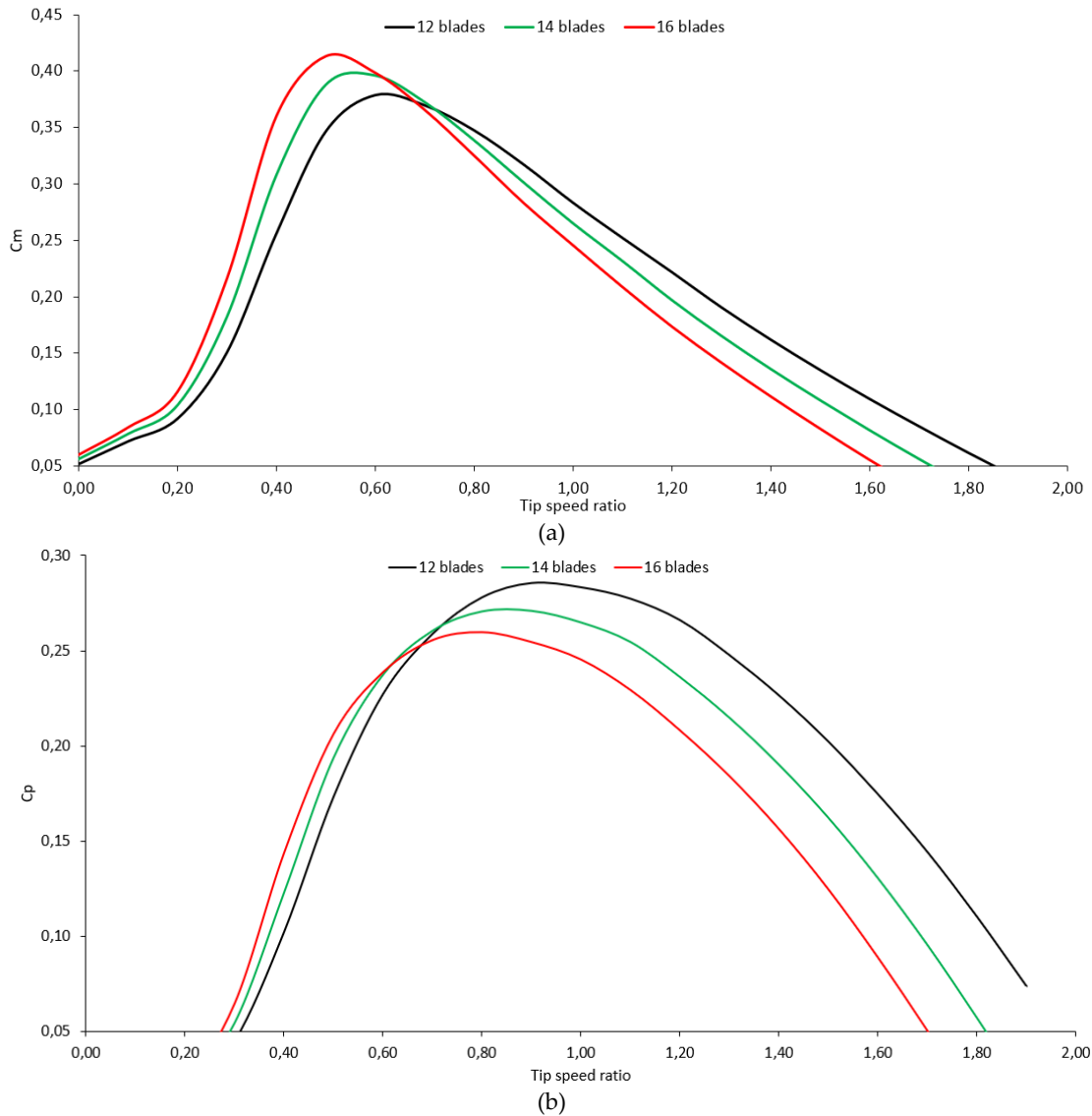


**Figure 2.10** Number of blades influence on (a) moment coefficient (b) power coefficient.

### 2.3.4 Blade shape

A simple and effective way of making blades for small wind turbines is to cut the blades from sections of metal or PVC pipe. The angle and twist of the blade can be controlled by the shape of the cut and the curve of the pipe approximates to an airfoil shape. When the airfoil is normalized, the camber and thickness of the blade depends on size of the section through the pipe. The following parameters are used to model a typical section.

- The wall thickness of the pipe is 5% of the radius.
- The leading edge is semi-circular.
- The camber is based on the top surface (outer radius of the pipe).
- The trailing edge is sharp and cut away at the bottom of the airfoil until it

meets the lower surface at a tangent.

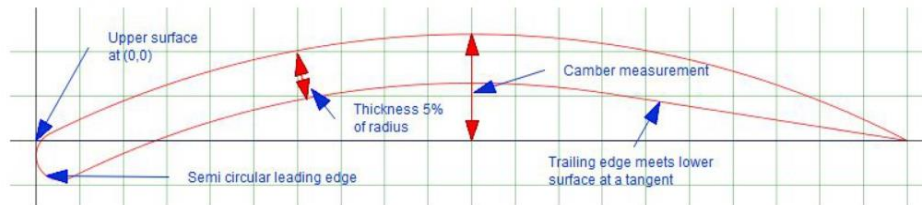


**Figure 2.11** (CP-160-050-GN) Camber=16% Wall thickness=5% Radius=0.861. Max thickness 5.2% at 3.4% chord. Max camber 14.3% at 49.2% chord [38]

In order to select the most suitable airfoil shape for the rotor of windmill water pumping system, different airfoils were simulated [39] and as the results of simulations, the curved shape airfoil has maximum lift. The curved shape airfoil has the minimum drag to lift ratio.

Using XFOIL from QBlade, we can predict the lift and drag coefficients of the aerodynamic airfoil at the Reynolds number calculated by the equation. Thus, from the Cl/Cd curve, we can easily determine the angle of attack that corresponds to the peak point of the curve in Figure 2.12.

$$Re = \frac{\rho Vc}{\mu} \tag{2.3}$$

With  $c$  the mean chord equal to 0.2 and  $V$  design wind speed of 6 m/s,  $\rho$  which is the density 1.225 and  $\mu$  the dynamic viscosity of the air

$$Re = 133489$$

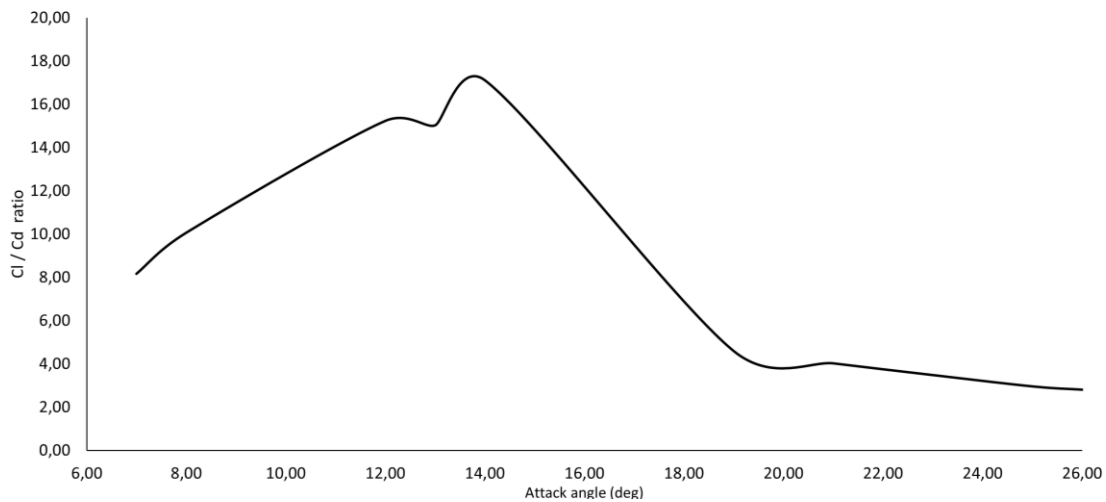


**Figure 2.12** Glide Ratio Cl/Cd curve.

### 2.3.5 Optimal pitch angle

For a TSR of 1 and a wind speed of 6 m/s, we aimed to determine the optimal pitch angle. Given that TSR and wind speed are fixed, the rotational speed can be deduced from the equation  $\lambda = \omega R/V$ , assuming our rotor has a radius of 1.5 meters. The rotational speed was approximately 38.2 rpm. After running several BEM simulations for a range of angles from 0° to 40°, we found that 29° was the optimal angle as shown in Figure 2.13, providing a maximum power output of 360 W and a torque of 90 N.m.

**Table 2.4** Input data for the BEM simulations.

Rotor Diameter [m]	3
Wind speed [m/s]	6
TSR	1
Rotational speed [RPM]	38.2
Number of blades	12
Kinematic viscosity [m <sup>2</sup> /s]	0.000014607
Air Density [kg/m <sup>3</sup> ]	1.225

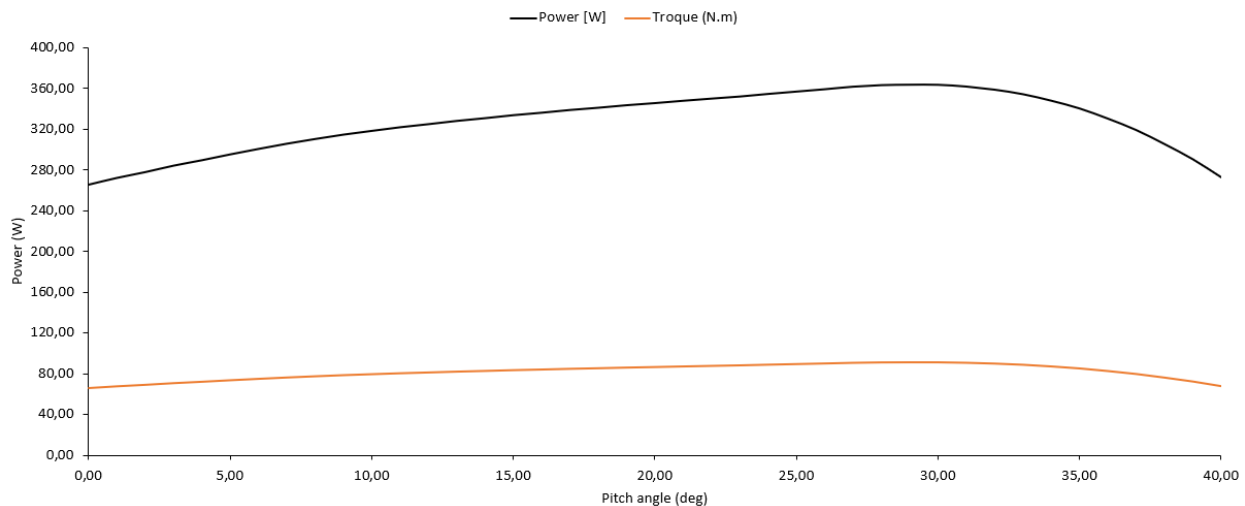


**Figure 2.13** Optimal pitch angle.

### 2.3.6 Structural analysis of the blade

Metals are undesirable because of their vulnerability to fatigue but smaller blades can be made from lightweight metals such as aluminum. To Build a solid wing we chose galvanized steel.

An important goal is to control the weight of the blade. Gravitational loads include axial loads and tension/compression loads as well as bending. The magnitude of these loads fluctuates cyclically, and the edge moment are reversed every 180° of rotation.

Wind is another source of loading of the rotor blades. Lift causes bending in the direction of the flap while airflow around the blade causes edge bending as shown in Figure 2.14.

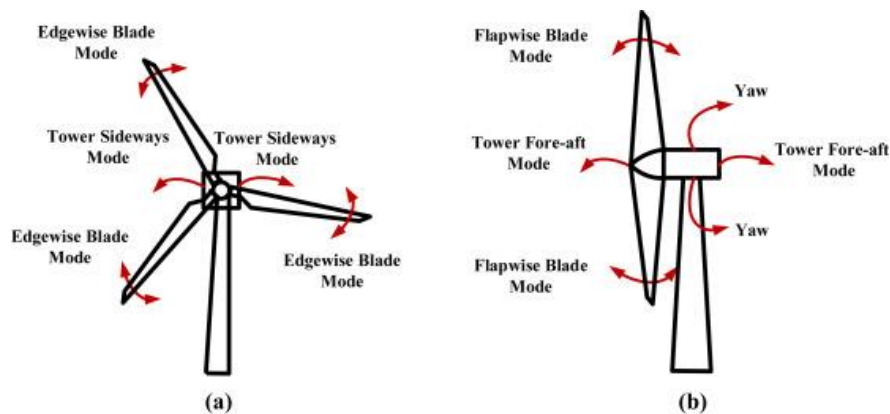


Figure 2.14 Blade edgewise and flapwise moments.

Figure 2.15 shows the equivalent stress along the blade at 6 m/s. The stress limit of the blade is determined by the strength of the galvanized steel used in the skin of the blade, which has a density of  $7200 \text{ kg/m}^3$  and an elastic modulus of up to 210 GPa. The stress development appears to be concentrated near the root of the blade, where the blade may fail, and at the trailing and leading edges. It can be noted that the most deflection occurs at the 20%-30% span distance from the tip, and most stress occurs near the root. QBlade also calculated the blade deformation at 38.2 rpm, and the deformations were very small, in the micro-deformation range, due to the high stiffness of the material.

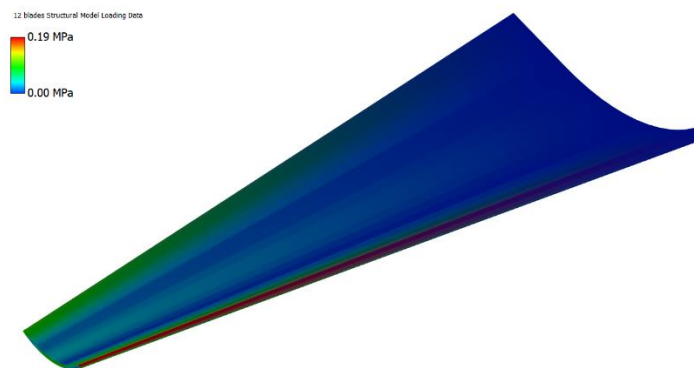


Figure 2.15 Structural analysis of the blade made from galvanized steel.

## 2.4 Piston Pump Design

To calculate mechanical power available for the pump there's some Loss

consideration to take in account. First of all, when it comes to bearings and gears, gears with excellent design and a finely finished surface can have an efficiency of 90% per pair of gears in contact. Then, when it comes to fluidic friction losses, using the right size smooth pipes, choosing the right values, and avoiding sudden bends can increase the efficiency up to 95% [33], which can be assumed to be 100%. Finally, when it comes to losses in the pump, even with the best design and excellent materials, the overall efficiency of the pump is estimated at 85%. The mechanical power available for the pump is calculated as follows:

$$P_{wind} = \frac{1}{2} \rho_a A v^3 \quad (2.4)$$

$$P_m = P_{wind} C_p \eta_p \eta_{Tr} \quad (2.5)$$

### 2.4.1 Calculation methodology

According to the previous equations developed in Chapter 2, we have  $b$  as a non-dimensional factor

$$b = \frac{8 \rho_w r_n}{\pi^2 \rho_a \eta_{Tr}} \quad (2.6)$$

Calculation of the geometric non-dimensional coefficient

$$\gamma = \frac{V_s}{d^3} \quad (2.7)$$

Where

$$A_p = \frac{\pi d_p^2}{4} \quad (2.8)$$

$$V_s = s A_p \quad (2.9)$$

$$\gamma = \frac{s A_p}{d^3} \quad (2.10)$$

Any combination of the stroke, cylinder diameter and turbine rotor diameter that satisfies equation 2.11 would lead to an optimal system configuration. To calculate the number of Fr

$$F_{rD} = \sqrt{\frac{b\gamma}{C_{TD}}} \quad (2.11)$$

In order to calculate the head, we use Froud's equation 2.11 and we get equation 2.12

$$F_{rD} = \frac{v}{\sqrt{gh}} \quad (2.12)$$

$$h = \frac{v^2}{gF_{rD}^2} \quad (2.13)$$

Calculating the flow rate by equality 2.14, which brings us back to equation 2.15

$$P_{water} = P_m = g\rho_w hq \quad (2.14)$$

$$q = \frac{P_m}{g\rho_w h} \quad (2.15)$$

For the calculation of the torque, we use equation 2.14

$$T = (\rho_w g h A_p) \left( \frac{s}{2} \cos(\theta) \right) \quad (2.16)$$

The maximum torque is calculated for  $\theta = 0$ , equation 2.16

$$T = \frac{s\rho_w g h A_p}{2} \quad (2.17)$$

To calculate the tangential force

$$F_t = \rho_w g h A_p \quad (2.18)$$

To calculate the pressure on the piston surface

$$P = \rho_w g h \quad (2.19)$$

Based on the previous design of the wind turbine, we have obtained power and torque coefficient curves, as shown in Figure 2.16. These curves are essential for designing the piston pump because the maximal power coefficient is needed to calculate the optimal Froude number. The input data are summarized in Table 2.4 above, and a numerical application was performed for a long-stroke configuration among several configurations listed in Appendix B-2.

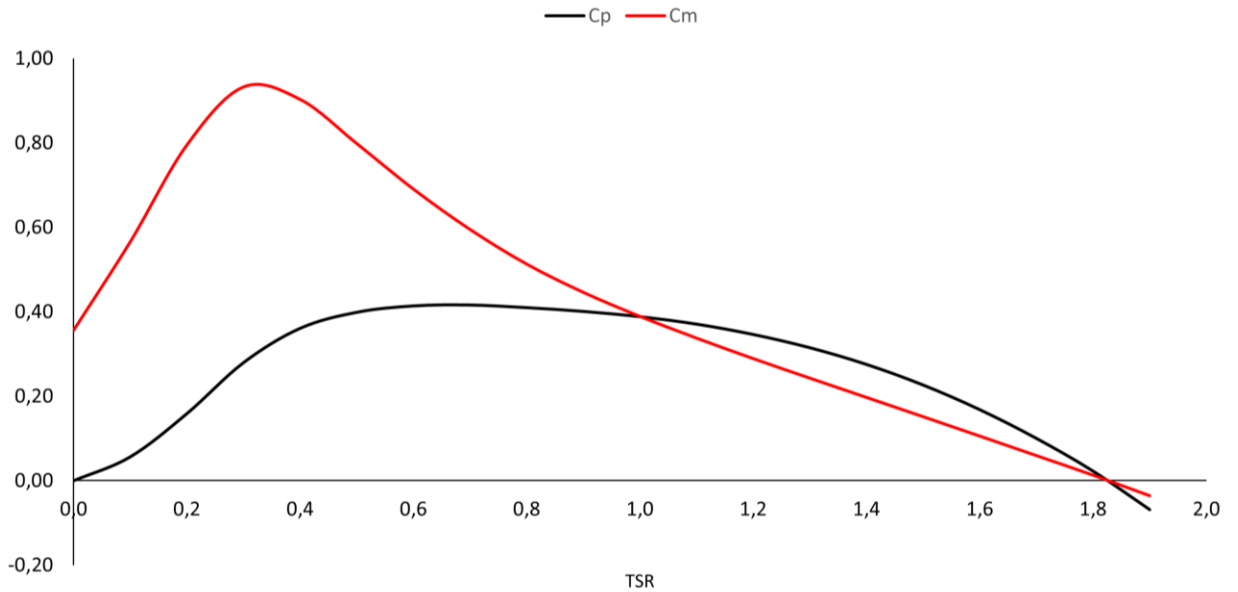


Figure 2.16 Cp and Cm - TSR curve.

Table 2.5 Wind turbine input data.

$d$ [m]	$A$ [m <sup>2</sup> ]	$V$ [m/s]	$\lambda$	$C_p$	$C_T$	$\rho_a$ [kg/m <sup>3</sup> ]	$\eta_{Tr}$
0.1	6.57	1	1	0.389	0.389	1.225	0.9

Table 2.6 Piston pump input data.

$d_p$ [m]	$s$ [m]	$r_n$	$m$	$\rho_w$ [kg/m <sup>3</sup> ]
0.05	0.2	1	1	1000

Table 2.7 presents the results obtained from using the equations, which firstly led to the optimal configuration of the piston pumps. Additionally, it allowed us to calculate the head and capacity, as well as the maximum torque required to lift the volume of water. Compared to the Poval wind pumps in the Appendix B-1, our wind pumps show a very high performances where the head is doubled for the same wind turbine of 3m diameter and with less blades and parts.

Table 2.7 Derived parameters.

$P_{rotor}$ [W]	$P_m$ [W]	$b$	$\gamma$	$Fr$	$h$ [m]	$Q$ [l/h]	$T$ [N.m]
364	278.64	735.210	0.00001454	0.17	133	765	257

## 2.5 Reducer design

Integrating a speed reducer into a wind pump enables smoother and more efficient operation by adjusting the wind turbine's speed to match the pump's needs. This reduces the risks of overheating and mechanical failures, while minimizing vibrations and noise. Additionally, the increased efficiency allows for maximum water production even in low winds, making the system more reliable. The speed reducer also facilitates the handling of varied loads, thereby extending the lifespan of the entire equipment.

### 2.5.1 Power transmitted by shafts

#### Input shaft

$$P_1 = P_{wt} = 364 W \quad (2.20)$$

#### Output shaft

$$P_2 = P_{wt} * \eta_p * \eta_m = 278.64 W \quad (2.21)$$

### 2.5.2 Shaft rotation speed

We know that

$$C = \frac{P}{\omega} \quad (2.22)$$

And we have the input and output torques  $C_1$  and  $C_2$  which represent the torque generated by the wind turbine and the torque required to lift the volume of water respectively.

#### Input shaft

$$\omega_1 = \frac{P_1}{C_1} = 4 \text{ rad/s} \quad (2.23)$$

Finally

$$N_1 = \frac{60\omega_1}{2\pi} = 38.23 \text{ rpm} \quad (2.24)$$

#### Output shaft

$$\omega_2 = \frac{P_2}{C_2} = 1.08 \text{ rad/s} \quad (2.25)$$

Finally

$$N_2 = \frac{60\omega_2}{2\pi} = 10.35 \text{ rpm} \quad (2.26)$$

### 2.5.3 Gear ratio

$$i = \frac{N_{input}}{N_{output}} = \frac{N_1}{N_2} = 3.69 \quad (2.27)$$

I	II	I	II	I	II
1.00	1.00	2.00	2.00	4.00	4.00
	1.12		2.24		4.50
1.25	1.25	2.50	2.50	5.00	5.00
	1.40		2.80		5.60
1.60	1.60	3.15	3.15	6.30	6.30
	1.80		3.55		7.1

Figure 2.17 Nominal gear Ratios [40].

According to the nominal standardized transmission ratios, a value is taken: **3.55**

### 2.5.4 Determination of Number of Teeth

$$i = \frac{Z_2}{Z_1} = 3.55 \quad (2.28)$$

We take  $Z_1 = 11$ , and we obtain  $Z_2 = 39$

### 2.5.5 Module Determination

$$m \geq 10 \times \sqrt[3]{\frac{11P}{k.Z.\sigma_p.\omega}} = 4.95 \text{ mm} \quad (2.29)$$

Where :

- P : Power to transmit
- k : Coefficient of tooth width, it is chosen according to the space available and according to the perfection of the shaft guides ( $10 < k < 12.5$ )
- $\sigma_p$ : The allowable tensile stress by the material. ( $75 \text{ N/mm}^2$ )
- Z : the number of teeth .
- $\omega$ : Rotation speed.

The standard modules range from 0.5 to 50 mm and are divided into three series: primary, secondary and exceptional. It is recommended to choose the modules of the main series and to avoid the use of the modules of the exceptional series. The following table gives the values of the usual standard modules.

**Table 2.8** Common standard modules [41].

I	3 ; 4 ; 5 ; 6 ; 8 ; 10 ; 12 ; 16 ; 20 ; 25 ; 32 ; 40 ; 50
II	3.5 ; 4.5 ; 5.5 ; 6.5 ; 7 ; 9 ; 11 ; 14 ; 18 ; 22 ; 28 ; 36 ; 45

According to the Main series, the module is taken: **5 mm**

### 2.5.6 Gear spacing

$$a = \frac{d_1 + d_2}{2} = \frac{m \cdot z_1}{2} + \frac{m \cdot z_2}{2} = 125 \text{ mm} \quad (2.30)$$

### 2.5.7 Geometric parameters

#### Pinions

**Table 2.9** Pinions parameters.

Designation	Symbol	Formula	Result
Module	m	m	5 mm
Step	p	$p = m \cdot \pi$	15.71 mm
Primitive diameter	$d_p$	$d_p = m \times z_1$	55 mm
Outside diameter	$d_o$	$d_o = d_p + 2m$	65 mm
Base diameter	$d_b$	$d_b = d_p \times \cos \alpha$	26.53 mm
Foot diameter	$d_f$	$d_f = d_p - 2.5m$	42.5 mm
Projection	$h_a$	$h_a = m$	5 mm
Hollow	$h_f$	$h_f = 1.25m$	6.25 mm
Tooth height	h	$h = h_a + h_f$	11.25 mm
Tooth thickness	s	$s = \pi \frac{m}{2}$	4.85 mm

#### Wheels

**Table 2.10** Wheels parameters.

Designation	Symbol	Formula	Result
Module	m		5 mm
step	P	$p = m \cdot \pi$	15.71 mm
Primitive diameter	$d_p$	$d_p = m \times z_2$	195.25 mm
Outside diameter	$d_o$	$d_a = d_p + 2m$	205.25 mm
Base diameter	$d_b$	$d_b = d_a \times \cos \alpha$	83.76 mm
Foot diameter	$d_f$	$d_f = d_p - 2.5m$	182.75 mm
Projection height	$h_a$	$h_a = m$	5 mm
Hollow height	$h_f$	$h_f = 1.25m$	6.25 mm
Tooth height	h	$h = h_a + h_f$	11.25 mm
Tooth thickness	s	$s = \pi \frac{m}{2}$	7.85 mm

### 2.5.8 Calculation of forces

A normal force  $F_N$  appears on contact with both teeth. This can be decomposed in two orthogonal directions: the tangential force and the radial force. We calculate the two components on the primitive circle of the wheel

#### Tangential Force ( $F_T$ )

$$F_T = \frac{C}{R} \quad (2.31)$$

For the pinions

$$F_T = \frac{2C_1}{dp_1} = 3305.89 \text{ N}$$

For the wheels

$$F_T = \frac{2C_2}{dp_2} = 2632.52 \text{ N}$$

#### Radial Force ( $F_R$ )

$$F_R = F_T \times \tan \alpha \quad (2.32)$$

For the pinions

$$F_R = 7395.81 \text{ N}$$

For the wheels

$$F_R = 5889.38 \text{ N}$$

**Normal force (F<sub>N</sub>)**

$$F_N = \sqrt{F_T^2 + F_R^2} \quad (2.33)$$

For the gears

$$F_N = 8101.04 \text{ N}$$

For the wheels

$$F_N = 6450.96 \text{ N}$$

**2.5.9 Preliminary Sizing of Shafts**

The gearbox shafts are subjected to torsional and bending stresses. In this phase of the project, bending cannot be taken into account, because we do not know the forces that load the trees, nor the distances between the supports, nor the location of the forces between the supports. So, to obtain indicative values of the shaft diameters, we will do their preliminary torsional sizing, taking into account the existence of the bending. We will work with acceptable values.

The preliminary dimensioning relationship:

$$d \geq \sqrt[3]{\frac{C}{0.2R_{pg}}} \quad (2.34)$$

$$R_{pg} = \frac{R_p}{2} = \frac{R_{pe}}{4} = 58.75 \text{ N/mm}^2 \quad (2.35)$$

Where

R<sub>pe</sub> : Elastic limit of the material (235 N/mm<sup>2</sup>).

R<sub>p</sub> : Basic permissible fatigue stress.

R<sub>pg</sub> : Modified permissible fatigue stress.

Then the diameter of the input shaft and output shaft  $d_1$  and  $d_2$  respectively

$$d_1 \geq \sqrt[3]{\frac{C_1}{0.2R_{pg}}} = 19.78 \text{ mm}$$

$$d_2 \geq \sqrt[3]{\frac{C_2}{0.2R_{pg}}} = 27.97 \text{ mm}$$

# Chapter 3

## Numerical Simulation of the scaled model

### 3.1 Introduction

Computational fluid dynamics (CFD) is one of the powerful tools for blade shape analysis of wind machines. Despite the blade element momentum theory seen in the sections above, CFD is a branch of fluid mechanics that uses numerical analysis and data structures to analyze and solve problems that involve fluid flows. Computers are used to perform the calculations required to simulate the free-stream flow of the fluid, and the interaction of the fluid with surfaces defined by boundary conditions. Initial validation will be performed using a wind tunnels in the next section.

### 3.2 Wind turbine scaling

In the previous section, we designed a wind turbine with a diameter of 3 meters using real dimensions, aiming to conduct wind tunnel tests and compare them with CFD results. To achieve this, scaling must be applied. One of the most well-known methods is based on the principle of similarity.

**Principle of similarity**, scaling relationships are considered mainly for changing the geometric size of the turbine. Reynolds number matching is ignored [42]. For scaling relations, Manwell et al. [25] use the following assumptions:

1. Keep the tip speed ratio constant.
2. Keep the blade profile, the number of blades and the blade material constant.
3. Geometric similarity is maintained to the extent possible.

Table 3.1 summarizes the relationships between quantities of interest for wind turbines based on rotor diameter as the scaling factor.

**Table 3.1** Scaling laws of wind turbines without Reynolds number matching [25].

Quantity	Symbol	Relation	Scale dependence
<b>Power, force, and moment</b>			
Power	P	$P_1/P_2 = (R_1/R_2)^2$	$\sim R^2$
Torque	Q	$Q_1/Q_2 = (R_1/R_2)^3$	$\sim R^3$
Thrust	T	$T_1/T_2 = (R_1/R_2)^2$	$\sim R^2$
Rotation Speed	$\Omega$	$\Omega_1/\Omega_2 = (R_1/R_2)^1$	$\sim R^1$
Weight	W	$W_1/W_2 = (R_1/R_2)^3$	$\sim R^3$
Aerodynamic Torque	$M_A$	$M_{A,1}/M_{A,2} = (R_1/R_2)^3$	$\sim R^3$
Centrifugal Force	$F_c$	$F_{c,1}/F_{c,2} = (R_1/R_2)^2$	$\sim R^2$
<b>Stress</b>			
Gravitational	$\sigma_G$	$\sigma_{g,1}/\sigma_{g,2} = (R_1/R_2)^1$	$\sim R^1$
Aerodynamic	$\sigma_A$	$\sigma_{A,1}/\sigma_{A,2} = (R_1/R_2)^0 = 1$	$\sim R^0$
Centrifugal	$\sigma_c$	$\sigma_{c,1}/\sigma_{c,2} = (R_1/R_2)^0 = 1$	$\sim R^0$
<b>Resonance</b>			
Natural Frequency	$\omega$	$\omega_{n,1}/\omega_{n,2} = (R_1/R_2)^1$	$\sim R^1$
Excitation	$\Omega/\omega$	$(\Omega_1/\omega_{n,1})/(\Omega_2/\omega_{n,2}) = (R_1/R_2)^0 = 1$	$\sim R^0$

Gao and Hu [43] recognize that dynamic similarity (Reynolds number matching) is hard to achieve with wind turbines of different sizes. They show that the power coefficient of two wind turbines is different if the Reynolds numbers are different. If the sizes of wind turbines are different, such as is usually the case with testing a scaled wind turbine in a wind tunnel as opposed to an actual wind turbine, the Reynolds number cannot be satisfied, and wind tunnel data cannot be directly applied to the original wind turbine.

Final features of the rotors are presented in Table 3.2 The rotors were named as rotor A, for the largest one, and rotor B, for the smallest one.

**Table 3.2** Output data of the scaling operation.

	Rotor A	Rotor B (scaled)
Number of blades	12	12
Blade airfoil	Cambered plate CP-160	Cambered plate CP-160
Rotor diameter (m)	3	0.53
Hub diameter (m)	0.8	0.15
Rotational speed (tr/min)	38.20	216.21
Wind speed (m/s)	6	6
Tip speed ratio	1	1
Design power (W)	935.73	29.21
Blade length (m)	1.1	0.190
Chord 1 (m)	0.150	0.500
Chord 2 (m)	0.025	0.083
Twist (°)	0	0

### 3.3 CFD step by step

In order to create the computational domain and generate mesh, the commercially available software ANSYS Workbench is used to build a wind tunnel (mimicking a wind tunnel) model and generate an unstructured mesh around the blade in the computational domain. Periodic boundary condition is applied to the right and left surface of the computational domain. Faces are meshed using Tetrahedral cells. A refined boundary layer is carefully constructed around the airfoil to capture the boundary layer behavior.

Computational Fluid Dynamics (CFD) provides a numerical approximation of the equations governing fluid motion. It comprises three main components:

1. **Preprocessor:** Manages meshing based on the studied geometry, flow parameters, and boundary conditions.
2. **Solver:** Resolves the equations that govern fluid flow under specified conditions.
3. **Post-processor:** Visualizes the results graphically.

This chapter details these steps to explain how CFD calculations were conducted to analyze the wind turbine's performance. CFD software operates by solving the Navier-Stokes equations around the geometry under specified constraints. A mesh is generated to pinpoint where these equations will be resolved, discretizing the physical space into finite points. A higher number of points yields a more accurate solution but requires more computational time and power. After generating the mesh, Fluent is configured with numerous variables, including models, solver settings, initial values, steps, and boundary conditions. Once the solver is configured, the results are visualized in the results tab.

### 3.3.1 Geometry preparation

**Control Volume Sizing.** After finalizing the 3D design of the scale model and centering the wind turbine, the geometry must be exported from SOLIDWORKS in IGES or PRT format for later import into ANSYS for CFD simulation. The CFD computation domain consists of a cylindrical wind tunnel, with far-field boundaries placed both axially and radially. The rotating domain includes the turbine blades. To reduce computation time, we will take advantage of the rotor's symmetry to study only 1/12 of the control volume, and then apply a periodic study.

**Blockage ratio.** The blockage effect observed during wind tunnel tests of rotors stems from the test section walls being closer than any natural obstacles in real-world conditions, leading to two primary causes [44].

- The first is the "solid blockage," which occurs due to the wind turbine model reducing the available space for air passage, temporarily increasing airflow velocity near the rotor.
- The second cause is "wake blockage," resulting from the test section walls interfering with the development of backward vortices behind the wind turbine.

In all cases where the blockage ratio  $BR$  exceeds 10%, the results obtained must be corrected by the blockage correction factor [44]. The blockage correction factor should be applied to the overall velocity increase due to the vortex and solid blockage effect. Blockage ratio is defined as:

$$B_r = \frac{A_s}{A_t} \quad (3.1)$$

where  $A_s$  is the projection surface of the wind turbine model, while  $A_t$  is the cross-sectional area of the air tunnel test section perpendicular to the air flow direction.

Since the control volume simulates a wind tunnel, and to avoid any blockage, we ensured that the blockage ratio remained below 10% by choosing a diameter for the control volume of  $2.75D$  as shown in Figure 3.1. About the distances along the z-axis, we used  $2.5D$  and  $7.5D$ , as found in the literature [45].

$$B_r = \frac{\frac{\pi d_{rotor}^2}{4}}{\frac{\pi d_{control\ volume}^2}{4}} = \left( \frac{D_{rotor}}{D_{control\ volume}} \right)^2 = \left( \frac{D_{rotor}}{2.75D_{rotor} \cdot 2} \right)^2 = 0.03 \quad (3.2)$$

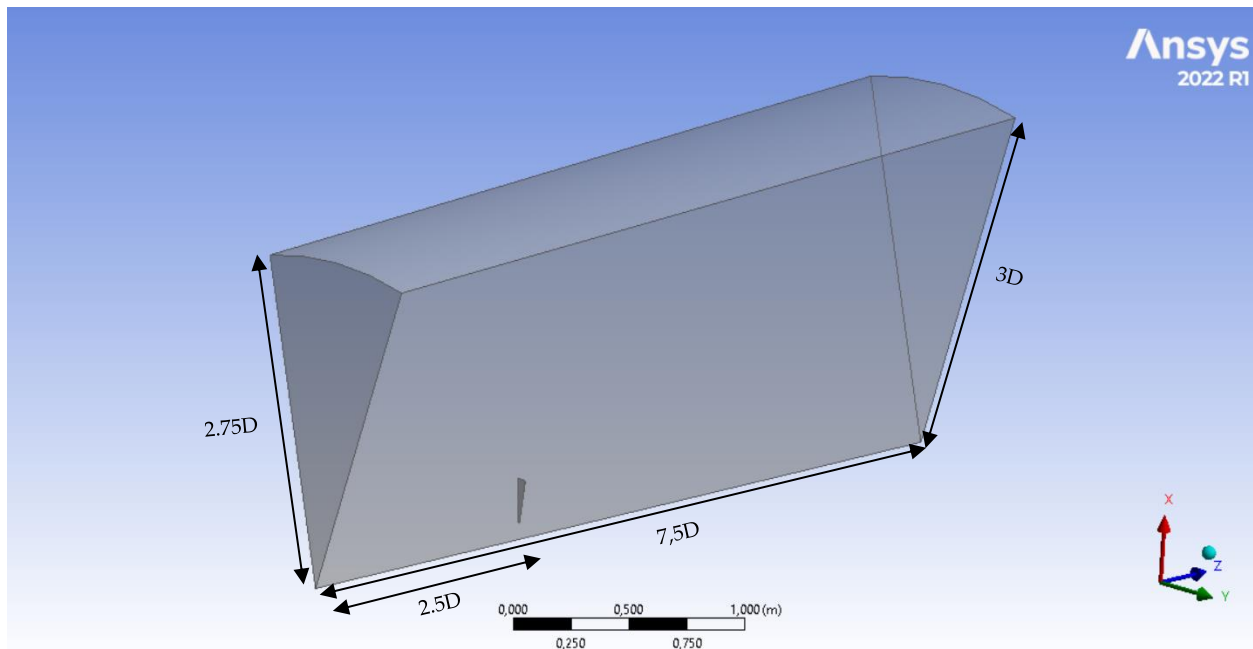


Figure 3.1 Control volume.

### 3.3.2 Mesh Preprocessor

**Mesh preparation.** Mesh generation involves creating a computational grid that represents the physical domain of the wind turbine and its surrounding environment. The quality and structure of this mesh significantly impact the accuracy, stability, and efficiency of the simulations. Additionally, to examine the trade-offs between computational cost and simulation fidelity, it's important to apply some strategies to achieve high-resolution results without excessive computational expense. Techniques such as mesh refinement, boundary layer meshing, and the use of rotating and stationary domains are also reviewed. Before preparing the mesh it's so important to apply some evaluations, understanding the wall law is so important to define the suitable mesh for the carried study.

**Universal law of Wall.** A valuable tool in understanding and analyzing turbulent flows is obtained by dimensional analysis of the flow near a solid boundary. It is known as the Law of the Wall and is derived by assuming that the turbulence near that boundary is a function only of the flow conditions pertaining at that wall and is independent of the flow conditions further away. For the non-dimensional analysis, we can identify the following limited set of wall regions and fluid properties illustrated in Figure 3.2:

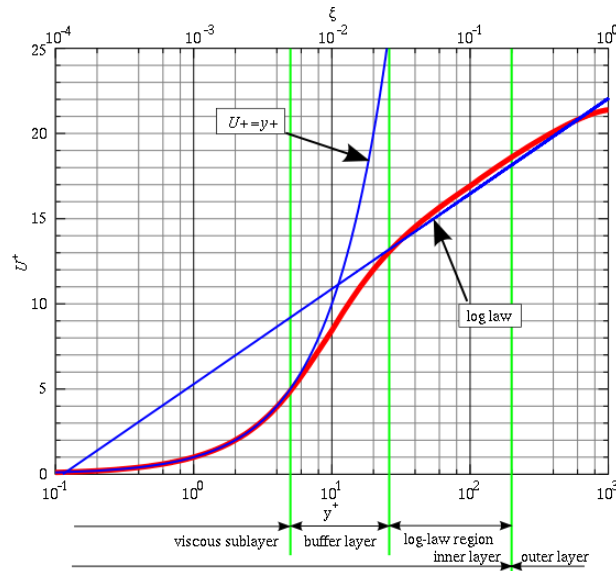


Figure 3.2 Law wall regions [46].

- **The viscous sublayer ( $y^+ < 5$ )** In the viscous layer, the fluid is dominated by the viscous effect, so it can be assumed that the Reynolds shear stress is negligible [46]. The “linear velocity law” is given by:

$$u^+ = y^+ \quad (3.3)$$

- **The logarithmic area ( $y^+ > 30$ )** In the logarithmic layer, turbulence stress dominate the flow and velocity profile varies very slowly with a logarithmic function along the distance  $y$  [46]. Formula 3.4 describes this region with the Karman constant  $\kappa$  of 0.41 and the constant  $B = 5.2$ .

$$u^+ = \frac{1}{\kappa} \ln(y^+) + B \quad (3.4)$$

- **The Buffer layer ( $5 < y^+ < 30$ )** The buffer layer is the transition region between the viscosity-dominated region and turbulence-dominated part of the flow. Viscous and turbulent stresses are of similar magnitude and since it is complex, the velocity profile is not well defined and the original wall functions avoid the first cell center located in this region [46].

- The distance,  $y$ , from the wall [m].
- The mean velocity (or velocity profile),  $u(y)$  [m/s].
- The shear stress,  $\tau_w$ , at the wall [kg/m.s<sup>2</sup>].
- The fluid density,  $\rho$  [kg/m<sup>3</sup>].
- The fluid kinematic viscosity,  $\nu$  [m<sup>2</sup>/s].

In ANSYS Meshing, there’s inflation function used to create layers of elements with a high aspect ratio near the boundaries of a geometry. This is particularly important

for accurately capturing boundary layer effects in fluid flow simulations. The inflation layer meshing strategy is crucial for resolving the gradients in the boundary layer, which can significantly impact the accuracy of the simulation results. When meshing geometry for a CFD analysis, it is often useful to estimate the wall distance to obtain a certain  $y^+$ . These are Formulas used to calculate the wall distance from  $y^+$ :

The predefined values for density and dynamic viscosity are for air at  $p = 1\text{atm}$  and  $T=20^\circ\text{C}$ ,  $\rho = 1.225 \text{ kg/m}^3$  and  $\mu = 1.75e - 05$

The Reynold Number for a given free stream velocity  $U_\infty$  is

$$Re = \frac{\rho U_\infty L_{\text{boundar layer}}}{\mu} \quad (3.5)$$

The Schlichting formula to obtain the skin friction coefficient  $C_f$  is used in this calculator and is valid for  $Re_x < 10e+9$

$$C_f = [2 \cdot \log_{10}(Re_x) - 0.65]^{-2.3} \text{ with } Re_x < 10^9 \quad (3.6)$$

The wall shear stress is calculated from the skin friction coefficient  $C_f$

$$\tau_w = C_f * \frac{1}{2} * \rho * U_\infty^2 \quad (3.7)$$

The friction Velocity  $u^*$  is a function of the fluid density and the wall shear stress

$$u^* = \sqrt{\frac{\tau_w}{\rho}} \quad (3.8)$$

And eventually the wall distance for a desired  $y^+$  is

$$y_p = \frac{y^+ \mu}{\rho u^*} \quad (3.9)$$

For complex flows, where accuracy is important and the flow is very different to a pipe flow,  $y^+$  near 1 is more accurate, because no correction is applied to the wall shear stress. Add to that wall functions are likely to be inaccurate here. In table 3.3 the first cell distance is computed.

**Table 3.3** Wall distance calculations for inflation configuration.

$Re$	22806
$C_f$	8.273e-3
$\tau_w$	1.824e-1 N/m <sup>2</sup>
$u^*$	3.859e-1 m/s
$y_p$	0.03785 mm

After generating the mesh, it is possible to observe in Figure 3.3, near the walls, a stacking of several layers with a certain growth ratio. This is due to the inflation applied, specifying a distance  $y_p = 0.03785$  mm as the thickness of the first layer. Inflation is very important for capturing phenomena occurring near the wall, such as the separation of the boundary layer.

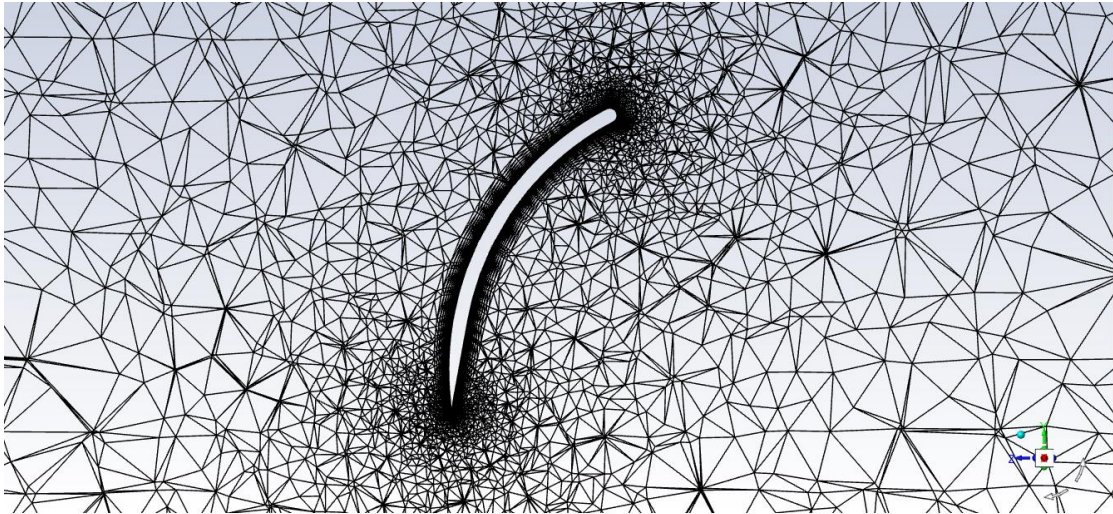


**Figure 3.3** Detailed view of blade inflation.

In Figure 3.4, the tetrahedral mesh generated by the Fluent solver is shown. At the leading and trailing edges, the cells become narrower to enhance the accuracy in that zones and catch more details due to the unstable behavior of the fluid. This instability is caused by various factors such as the geometric shape of the airfoil, the formation of the boundary layer, pressure fluctuations, and irreversibility like vortex generation and wake formation, as well as boundary layer separation.

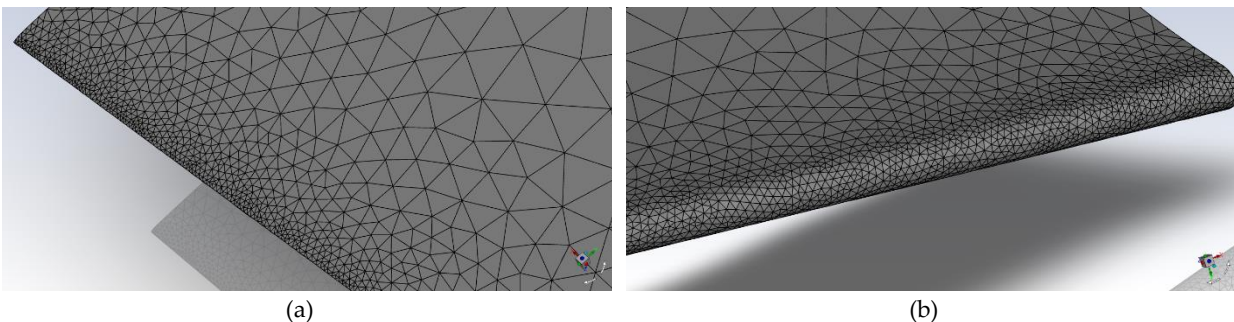


**Figure 3.4** Clear view of the mesh around blade (a) trailing edge (b) leading edge.

### 3.3.3 Solver configuration

CFD computations are performed by imposing flow velocities, static pressure and static temperature at the far-field inlet and outlet boundaries. The turbulent wind flows

towards the positive z-direction at 6 m/s which is a typical rated wind speed for a turbine at this size. This incoming flow is assumed to make the blade rotate at an angular velocity of 22.642 rad/s about the z-axis. The tip speed ratio is therefore equal to 1 which is a reasonable value for a slow wind turbine. The blade root is offset from the axis of rotation by 0.07 meter. We define the velocity at the inlet and the far field (top-inlet) of 6 m/s with turbulent intensity of 5% and turbulent viscosity ratio of 10 and the Pressure of 1 atm to validate the present simulation. **Frame motion-based** approaches simplify the simulation of moving reference frames by keeping the mesh stationary and adding forces as source terms. As the physical geometry and the flow solution have a periodically repeating nature figure 3.5, a **periodic boundary conditions** function is available in ANSYS FLUENT. Periodic boundary conditions are a powerful tool in computational simulations, enabling efficient modeling of systems with inherent periodicity. They help reduce computational resources while accurately capturing the repetitive nature of the physical phenomena under study.

Key points before applying the periodic boundary condition:

- The two faces need to be of the same size and shape
- The two faces need not be in the same orientation
- The face elements of the mesh on the two faces need not be congruent. This means both structured and unstructured meshes can be used.

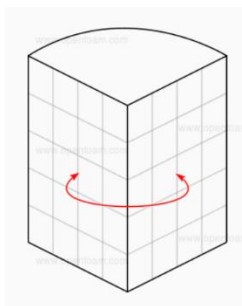


**Figure 3.5** Periodic boundary conditions.

To create periodic boundary conditions in recent versions of Fluent, the meshes of the two interfaces must be identical. Achieving these conditions can be challenging. However, it is possible to create a non-conformal periodic boundary condition using the Fluent console by typing `\define/boundary-conditions/create-periodic-mesh\`. This command generates the necessary mesh interface.

**Mathematic Model.** The governing equations are the continuity and Navier-Stokes equations. These equations are written in a frame of reference rotating with the blade. This has the advantage of making our simulation not require a moving mesh to account for the rotation of the blade. The equations that we will use look as follows:

Conservation of mass [47]

$$\nabla \cdot \rho v_r = 0 \tag{3.10}$$

Conservation of Momentum (Navier-Stokes):

$$\nabla \cdot (\rho v_r) + \rho(2\omega \times v_r \times \omega + \omega \times \omega \times r) = -\nabla p + \nabla \cdot \tau_r \tag{3.11}$$

Wherever is the relative velocity (the velocity viewed from the moving frame) and  $\omega$  is the angular velocity.

**Limitations of Wall Functions.** In cases of boundary layer separation, wall functions are inadequate as they fail to correctly predict the profile. Directly resolving the viscous sublayer is necessary for accurate results [48]. Essentially for high angle of attack wall function might be less accurate as shown in Figure 3.6.

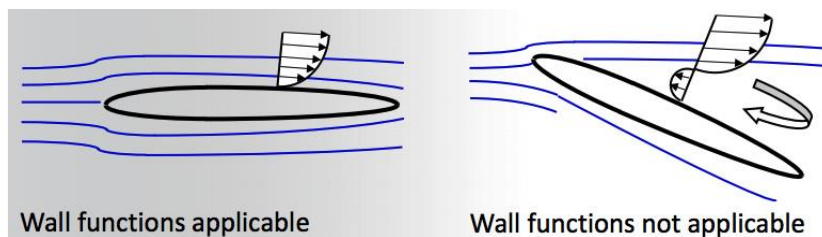


Figure 3.6 Wall function limitations.

We chose the Spalart-Allmaras turbulence model for this study due to its robustness and efficiency in handling boundary layer flows, particularly in aerodynamic applications. This one-equation model simplifies the computational process while providing reliable results for flows with adverse pressure gradients and mild separation. Unlike other turbulence models, the Spalart-Allmaras model does not rely on wall functions to approximate the near-wall region. Instead, it resolves the viscous sublayer directly, ensuring that the dimensionless wall distance,  $y^+$ , is maintained at around 1. This approach allows for a more accurate representation of the flow characteristics close to the wall, capturing the effects of viscosity and turbulence interactions with greater precision. By ensuring  $y^+$  is approximately 1, we achieve a fine mesh resolution near the wall, which is crucial for accurately predicting shear stresses and heat transfer rates. This direct resolution of the near-wall region enhances the model's accuracy and reduce the time-cost, making it an optimal choice for our simulations.

The Spalart-Allmaras turbulence model is a RANS approach that involves a single governing kinematic equation to describe kinematic eddy viscosity. The model was specifically derived for use in aerodynamic applications involving wall-bounded systems as well as in turbomachinery applications. This one-equation model allows simpler resolution of the eddy viscosity near a system boundary (such as a wall).

The Spalart-Allmaras turbulence model follows a single dynamic equation

describing a kinematic viscosity-like variable, called the Spalart–Allmaras variable [49]:

$$\frac{\partial \hat{\nu}}{\partial t} + u_j \frac{\partial \hat{\nu}}{\partial x_j} = c_{b1}(1 - f_{t2})\hat{S}\hat{\nu} - [c_{w1}f_w - \frac{c_{b1}}{\kappa^2}f_{t2}]\left(\frac{\hat{\nu}}{d}\right)^2 + \frac{1}{\sigma}\left[\frac{\partial}{\partial x_j}\left((\nu + \hat{\nu})\frac{\partial \hat{\nu}}{\partial x_j}\right) + c_{b2}\frac{\partial \hat{\nu}}{\partial x_i}\frac{\partial \hat{\nu}}{\partial x_i}\right] \quad (3.12)$$

The goal in this equation is to determine the turbulent eddy viscosity, which is determined from:

$$\mu_t = \rho \hat{\nu} f_{v1} \quad (3.13)$$

Where

$$f_{v1} = \frac{\chi^3}{\chi^3 + c_{v1}^3} \quad (3.14)$$

And

$$\chi = \frac{\hat{\nu}}{\nu} \quad (3.15)$$

In these equations, the molecular kinematic viscosity is  $\nu = \mu/\rho$ , the fluid density is  $\rho$ , and  $\mu$  is the fluid's molecular dynamic viscosity. The other parameters in the model are given in terms of the distance from the field point to the nearest wall  $d$ , and the vorticity magnitude

$$\Omega = \sqrt{2W_{ij}W_{ij}} \quad (3.16)$$

Where

$$W_{ij} = \frac{1}{2}\left(\frac{\partial u_i}{\partial x_j} - \frac{\partial u_j}{\partial x_i}\right) \quad (3.17)$$

We have the following definitions

$$\hat{S} = \Omega + \frac{\hat{\nu}}{\kappa^2 d^2} f_{v2} \quad (3.18)$$

$$f_{v2} = 1 - \frac{\chi}{1 + \chi f_{v1}} \quad (3.19)$$

$$f_w = g \left[ \frac{1 + c_{w3}^6}{g^6 + C_{w3}^6} \right]^{1/6} \quad (3.20)$$

$$g = r + c_{w2}(r^6 - r) \quad (3.21)$$

And

$$f_{v2} = c_{t3} \exp(-c_{t4}\chi^2) \quad (3.22)$$

One can see several constants in the above definitions. These constants are defined as follows

$$\kappa = 0.41, c_{b1} = 0.135, \sigma = \frac{2}{3}, c_{b2} = 0.622, c_{v1} = 7.1, c_{w2} = 0.3, c_{w3} = 2, c_{t3} = 1.2 \text{ and } , c_{t4} = 0.5$$

### 3.3.4 Mesh dependency

As in two-dimensional simulation, the results of modeling work may not be satisfactory on the first attempt, and CFD studies require multiple trials to achieve consistent results. Finding the right mesh for a CFD simulation is a repetitive and tedious task. The accuracy of numerical simulation results first depends on the results of a mesh independence test. In this study, the choice of the test led us to perform a steady-state simulation to ensure result accuracy. For this purpose, the simulation domain meshes were progressively refined until the rotor total torque remained constant, and it was verified for each mesh that  $y^+$  was below 1. The numerical simulation results are shown in Table 3.4.

**Table 3.4** Mesh dependency results.

	<b>Mesh 1</b>	<b>Mesh 2</b>	<b>Mesh 3</b>
<b>Nodes</b>	869.504	1.190.768	1.604.336
<b>Cells</b>	3395905	4929624	7037540
<b>CPU time</b>	1h30min	2h30 min	5h30min
<b>Total Torque [N.m]</b>	0.4656	0.4635	0.4665
<b>Average Wall <math>y^+</math> near the blade</b>	0.552469	0.558367	0.558846

In figure 3.7, the scatter and histogram plot show that the majority of  $y^+$  values are below 1 which also indicates a very fine mesh, it is ideal for accurately capturing the boundary layer and resolving the viscous sublayer without relying on wall functions. This leads to improved accuracy in predicting skin friction, lift, and drag forces. However, this level of detail comes with increased computational cost.

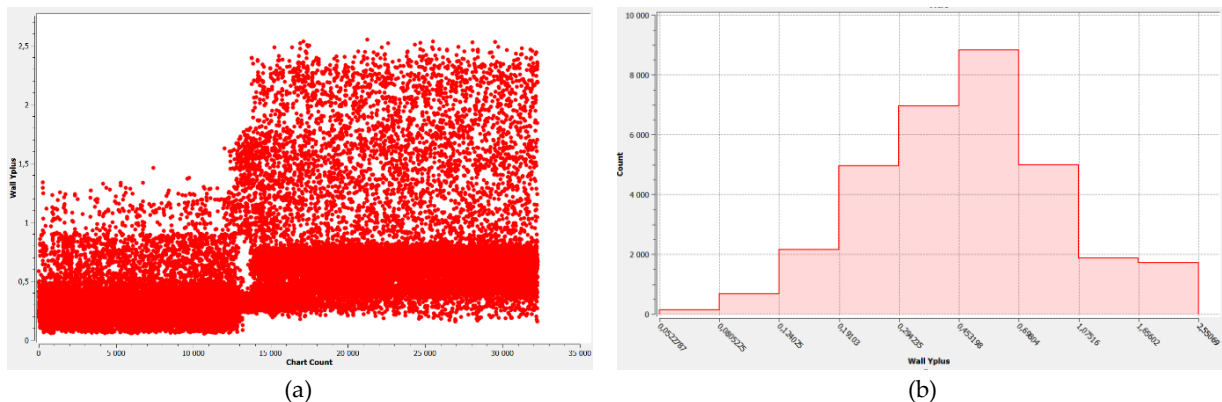


**Figure 3.7** Statistics on the values of  $y^+$  around the blade.

In Figure 3.8, the areas with  $y^+$  values above 1, particularly the red and green regions along the leading edge, highlight the challenges Fluent encountered in accurately capturing the curvatures in this area. These issues stem from insufficient mesh resolution in regions with high curvature, leading to less accurate modeling of complex flows. To address this, the mesh can be refined by increasing cell density, employing adaptive meshing techniques, and adjusting meshing parameters to better follow the leading edge contours. However, these solutions can significantly raise the computational cost and resource requirements, necessitating a balance between accuracy and computational expense.

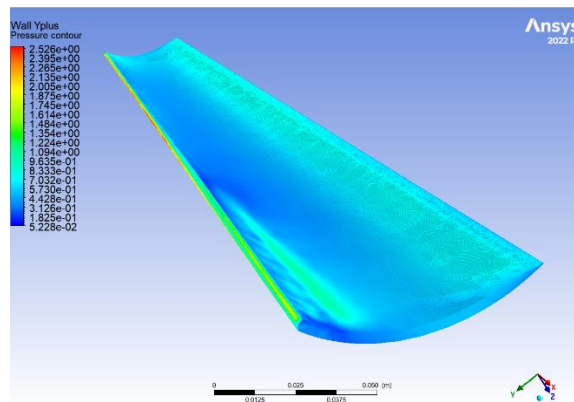


**Figure 3.8** Contour plot of the  $y^+$  values near the blade.

After analyzing the results of the three meshes, we observed that for meshes 1, 2, and 3 (coarse, fine and very fine meshes), the total torque values obtained were very close. Therefore, to avoid unnecessary mesh refinement and to save computational time, we decided to use mesh 1 (coarse) for the remaining calculations.

# Chapter 4

## Fabrication and Experimental Validation

### 4.1 Manufacturing Experience

To prepare the test bench, a comprehensive set of parts, as detailed in Table 4.1, was fabricated using both 3D printing and traditional machining techniques. The hub, connecting rod, shaft, and blades were specifically manufactured using 3D printing technology, utilizing Creality CR10 and Ender 3 with a precision of  $\pm 0.4 \text{ mm}$  as depicted in Figure 4.1. The process began with the creation of detailed 3D models using SolidWorks, a CAD software. These models were then exported as STL files, which were subsequently imported into Cura, a slicing software, to generate the necessary G-code for the 3D printers. The material chosen for 3D printing was PLA (Polylactic Acid), a biodegradable and environmentally friendly thermoplastic known for its ease of use and good mechanical properties. The printing process involved meticulously layering the PLA to form the desired shapes, a task that required several hours to complete due to the complexity and precision needed for each part.



Figure 4.1 3D printer (a) Ender 3 (b) Creality 10.

Table 4.1 Designations of the different mechanical components.

Designation	Illustration	Description
Hub		The role of a hub in a wind turbine is to connect the blades to the main shaft, facilitating the transfer of rotational energy to the generator.
Blade		The role of a blade in a wind turbine is to capture the kinetic energy of the wind and convert it into mechanical energy to generate electricity.
Shaft		The role of a shaft is to transmit torque and rotational motion from rotor part to connecting rod.
Connecting rod		The role of a connecting rod is to transfer motion and force between the piston.

Tower



The role of the tower in a wind turbine is to support the rotor and blades.

---

Bearing



The role of a bearing is to support and reduce friction between moving parts, enabling smooth and efficient rotation or linear movement.

---

Weight holder



The weight plate is used to support the mass needed to be hung to neutralize the rotor moment.

---



**Figure 4.2** Final Assembly of the windmill.

## 4.2 Operation of the test bench system

The mechanical power of the rotor can be determined by measuring the mechanical torque on the rotating shaft and the rotational speed at different wind speeds. The wind tunnel used for this purpose is illustrated in Figure 4.3. The wind turbine was designed with a connecting rod, an inextensible fabric cord, and a weight-carrying plate. The plate and the spring were used to apply braking load on the rotor to measure its torque, and they were attached by a 1 mm diameter fabric thread. The cord was wrapped (360°) around the big end of the connecting rod, and the axis was fixed by a bearing to guide the rotor.



Figure 4.3 Wind tunnel.

The rotor spins freely under the effect of wind produced by the wind tunnel. The wind speed and rotor rotation speed were recorded using an anemometer and a digital tachometer. For each test, the mass remains constant, and it is this load that will eventually stop the rotation of the wind turbine. Simultaneously, the wind speed is increased in increments of 0.1 m/s until the wind turbine starts to rotate. This load allows us to determine the braking torque according to the equilibrium equations below.

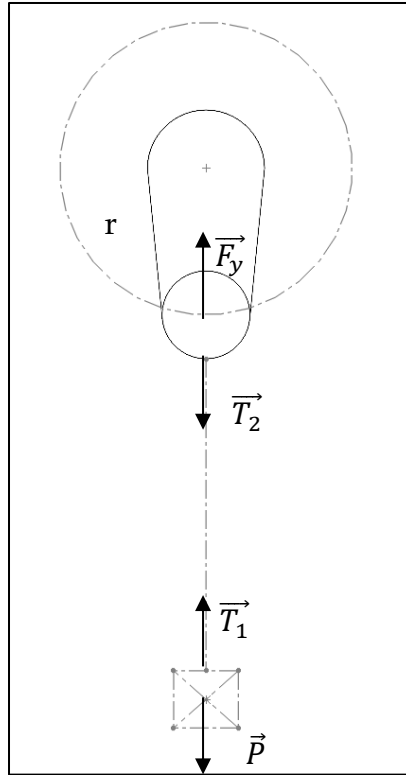


Figure 4.4 Diagram of forces.

Applying the fundamental relation of dynamics to a rotating system, we have

$$\sum \vec{F}_{ext} = m \cdot \vec{a} \quad (4.1)$$

At the equilibrium

$$\sum \vec{F}_{ext} = 0 \quad (4.2)$$

$$\vec{P} + \vec{T}_1 + \vec{T}_2 + \vec{F}_y = 0 \quad (4.3)$$

Where

- $\vec{P}$  : The weight applied by the mass
- $\vec{T}$  : Forces applied by both ends of the wire
- $\vec{F}_y$  : Shaft Force

By projection we find

$$-P + T_1 - T_2 + F_y = 0 \quad (4.4)$$

For inextensible wires and negligible friction, we have

$$T_1 = T_2 \quad (4.5)$$

We will get

$$F_y = P \quad (4.6)$$

Then

$$F_y = m * g \quad (4.7)$$

To calculate the braking torque

$$T_{braking} = m * g * r \quad (4.8)$$

With  $r$  is the distance of the arm

Concerning the torque as a function of the angle travelled, it is written as follows

$$T = A(1 + \cos\theta) \quad (4.9)$$

When  $\theta = 0$ , the torque is equal to  $2A$  so it will be presented as the braking torque and the maximum torque.

### 4.3 Assessment of uncertainty propagation

The wind speed measurement was done using an anemometer KIMO MP200, allowing for precise determination of the air flow intensity in the wind tunnel. A Pitot tube anemometer works by measuring the pressure difference between two points. The Pitot tube has a front opening that captures the total pressure (dynamic pressure plus static pressure) and a lateral opening that captures only the static pressure. The difference between these two pressures allows for the calculation of wind speed using Bernoulli's equation. When it comes to a wind speed between 2 and 5 m/s, the manufacturer has given an uncertainty of  $\Delta y = \pm 0.3$  m/s otherwise  $\Delta y = \pm 0.2$  m/s.

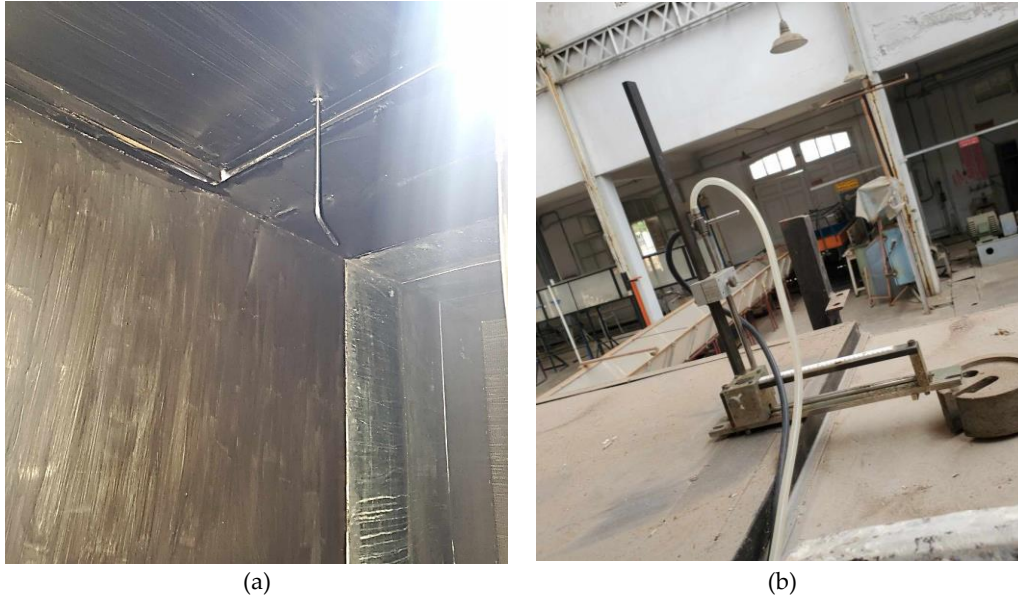


**Figure 4.5** Anemometer.

The rotation speed measurement was done using a digital tachometer UT371, providing an accurate reading of the rotor's revolutions per minute (RPM). It uses an optical or magnetic sensor to detect the rotor's movements. As the rotor turns, the sensor sends pulses to the tachometer, which counts these pulses over a defined period of time. The tachometer then converts these pulses into a rotational speed measurement, typically expressed in revolutions per minute (RPM). When it comes to a rotational speed between 100 *rpm* and 999 *rpm*, the manufacturer has given an uncertainty of  $\Delta y = \pm 0.04\%$

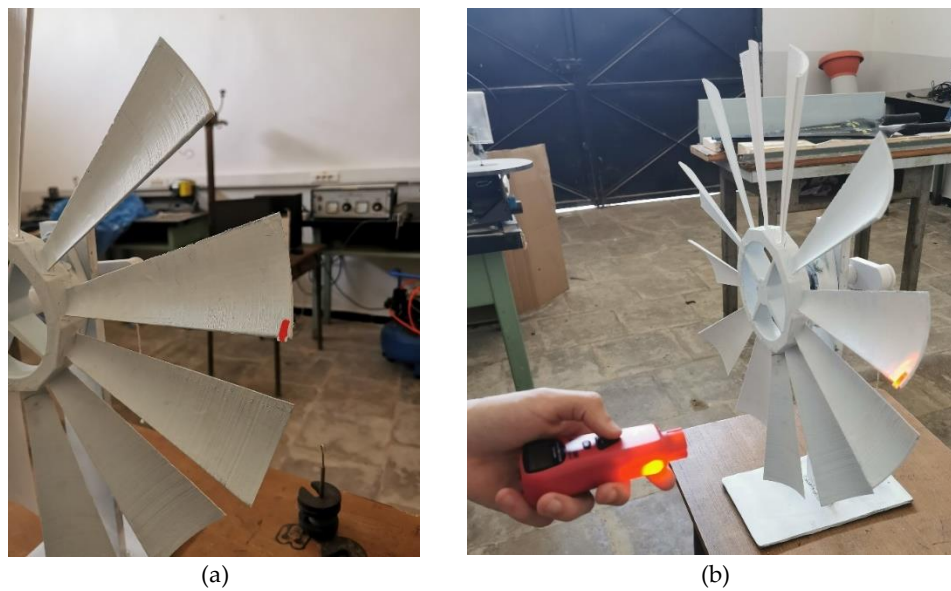


**Figure 4.6** Tachometer.

The braking torque was applied using a series of calibrated masses, allowing for

precise determination of the force needed to stop the rotor's rotation. For the uncertainty of the masses which are already calibrated, an uncertainty of  $\pm 1$  g has been estimated by us due to the deterioration of the material by unfavorable external conditions.



Figure 4.7 Calibrated weights.

Each measured quantity has a certain uncertainty  $\Delta x_1, \Delta x_2, \dots$ , and these combine to produce the total uncertainty  $\Delta y$  in the result  $y$ . The way in which the uncertainty of each individual parameter contributes to the total uncertainty is described by the propagation of uncertainties. The application of the propagation of uncertainties is described by the following formulas:

**Sum/Difference:** when the composite quantity consists only of sums or differences

$$\Delta y = \Delta x_1 + \Delta x_2 + \Delta x_3 + \dots \quad (4.10)$$

Where  $y = x_1 \pm x_2 \pm x_3$

In a sum (or difference), the absolute errors are added together.

**Product/Quotient:** when the composite quantity consists only of products or quotients

$$\frac{\Delta y}{|y|} = \frac{\Delta x_1}{|x_1|} + \frac{\Delta x_2}{|x_2|} + \frac{\Delta x_3}{|x_3|} + \dots \quad (4.11)$$

Where  $y = x_1 \cdot x_2 / x_3$

In a product (or quotient), the relative errors are added together.

**Product of powers:** when the composite quantity consists only of a product of powers.

$$\frac{\Delta y}{|y|} = |\alpha| \frac{\Delta x_1}{|x_1|} + |\beta| \frac{\Delta x_2}{|x_2|} + |\gamma| \frac{\Delta x_3}{|x_3|} + \dots \quad (4.12)$$

Where  $y = x_1^\alpha \cdot x_2^\beta \cdot x_3^\gamma$

# Chapter 5

## Results and Discussion

In this chapter we will present the results of the numerical CFD simulations mentioned in Chapter 3 and the results of the experiment in Chapter 4 by validating our reduced model.

### 5.1 Discussion of numerical simulation CFD results

When wind passes through a wind turbine, its pressure experiences significant changes due to the conversion of kinetic energy into mechanical energy. Figure 5.1 shows the pressure variance along the z-axis, where we can clearly see the pressure drop at the  $z = 0$  because of the wind turbine. As the wind approaches the turbine blades, the pressure increases slightly due to the aerodynamic effect of the blades slowing the wind down. This pressure variance is a crucial factor in the efficiency and performance of the wind turbine.

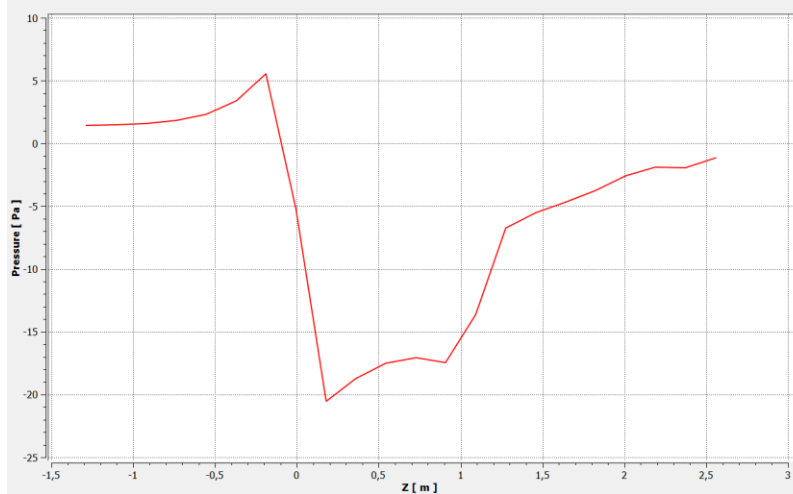


Figure 5.1 Pressure Variance.

Figure 5.2 illustrates the velocity magnitude contour plot for the 3D wind turbine. The wind turbine blade rotates along the z-axis. As we move away from the root, velocity increases and is maximum at the tips of the blade. Very high velocities of up to 6 m/s are observed at the tip of the blade, re-emphasizing the need for thicker profile of the root of the blade.

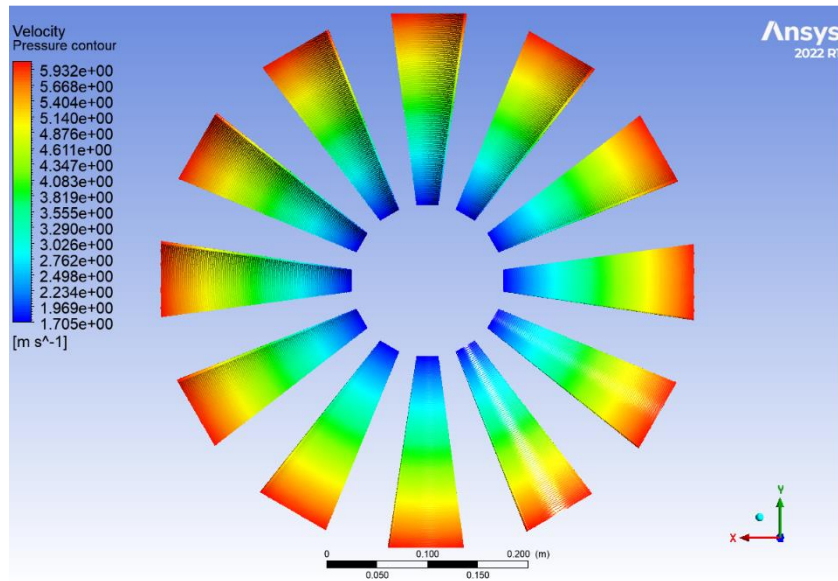


Figure 5.2 Velocity contour plot.

Figure 5.3 represents the 2-D cross sectional view of pressure contours streamline at 50% from root to tip, for 6 m/s free stream velocity. Due to the larger negative pressure on the upper surface, lift force is generated and as a result the wind turbine blade rotates. Negative pressure can be explained by the wake generation from the blade.

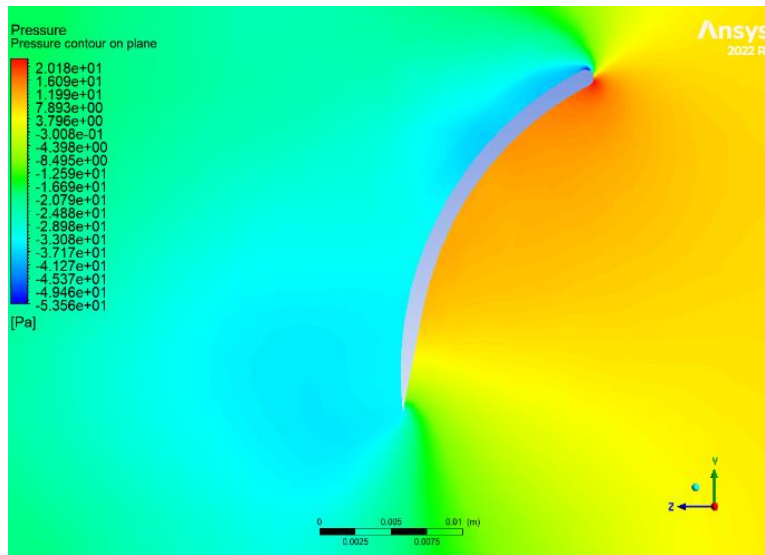


Figure 5.3 Airfoil pressure contour plot at the half of the blade.

Figure 5.4 shows a velocity contour plot for airfoil 6m/s and angle of attack of 24 degree. A stagnation point is observed at the leading edge of the plot where the velocity is zero. As air flows around the airfoil, higher velocities are observed at the top of the airfoil as compared to the bottom. This happens due to the shape of the airfoil. A small region of separation is also visible in this plot at the tail of the airfoil.

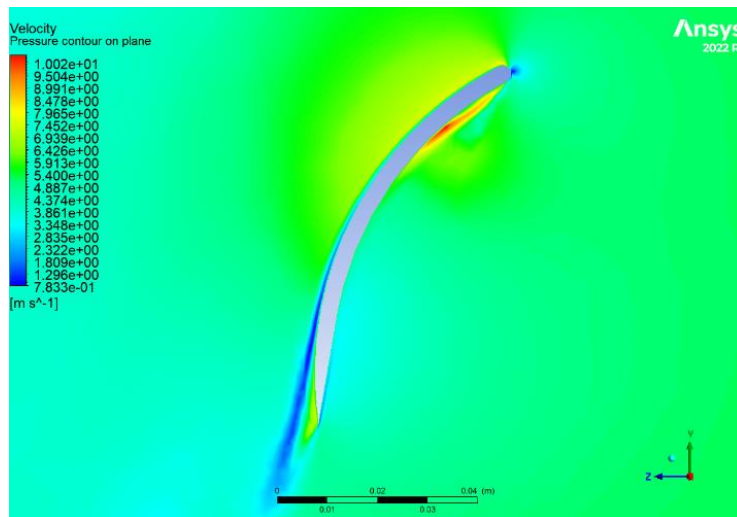


Figure 5.4 Velocity contour plot of the airfoil at the half of the blade.

According to Bernoulli's equation for incompressible fluids, the change in pressure is always inversely proportional to the change in speed, when the speed reaches its maximum at the point of stopping at the pressure it reaches its minimum.

The recent version of QBlade offers a new correction add to tip loss and 3d correction called DTU Poly BEM correction. In our work and because there's a lake of

information about this correction we did a little investigation on the influence of this correction and we found that there's a significant effect on the results as shown in Figure 5.5.

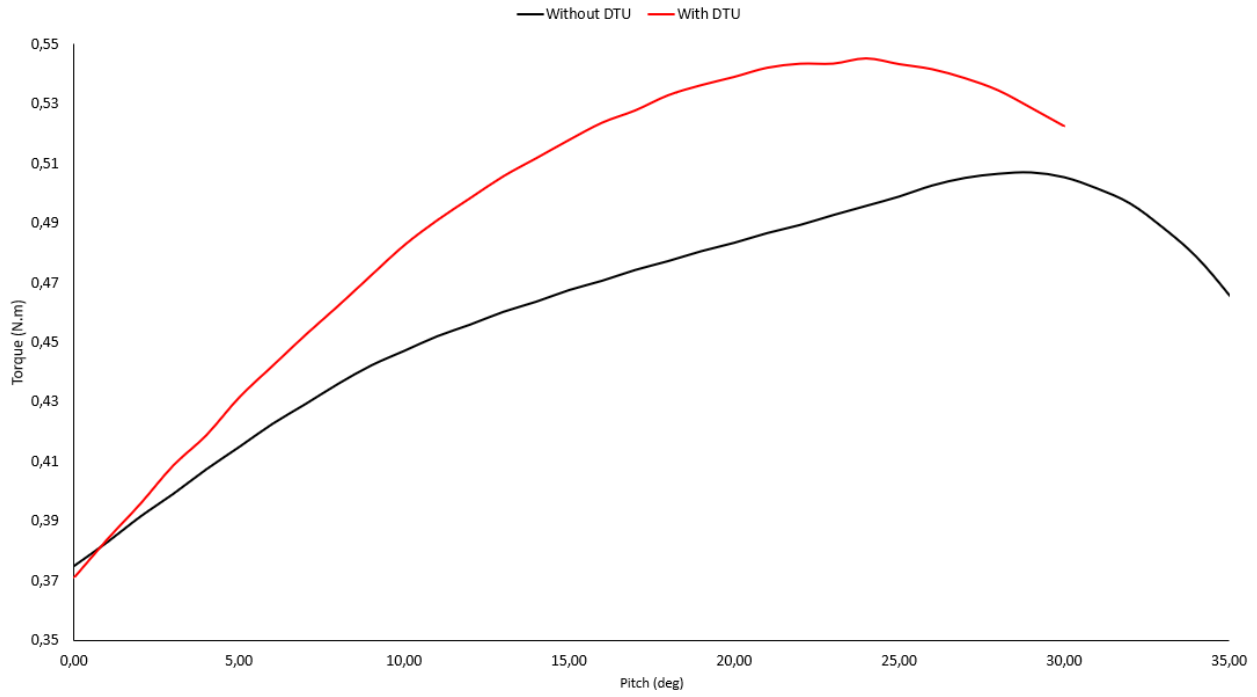


Figure 5.5 DTU poly bem correction effect.

The “DTU Poly BEM” refers to the relationship between the axial induction factor and the thrust coefficient that is expressed as a third-order polynomial. If the DTU Poly-BEM is not selected the standard Glauert correction is used in QBlade.

$$C_T = 4a(1 - a) \tag{5.1}$$

When the thrust coefficient  $C_T$  is high positive, Qblade use the polynomial equation of a induction factor in the equation 5.2 and expressed through the following third-order polynomial shown in Figure 5.6:

$$a = k_3 C_T^3 + k_2 C_T^2 + k_1 C_T \tag{5.2}$$

where the coefficients  $k_1 \dots k_3$  are defined as  $k_1 = 0.2460$ ,  $k_2 = 0.0586$  and  $k_3 = 0.0883$ .

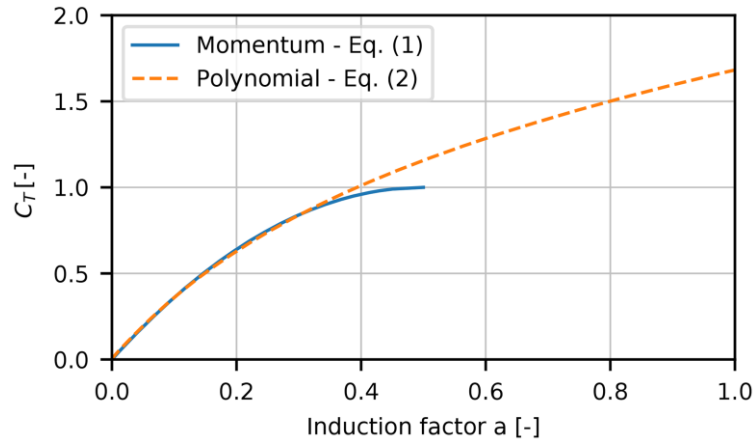


**Figure 5.6** Induction factor formulas effect on the thrust coefficient [50].

For  $C_T < 0.89$ , the polynomial fits well the momentum equation [50], and in our case thrust coefficient is under 0.80 and obviously we must use the momentum equation.

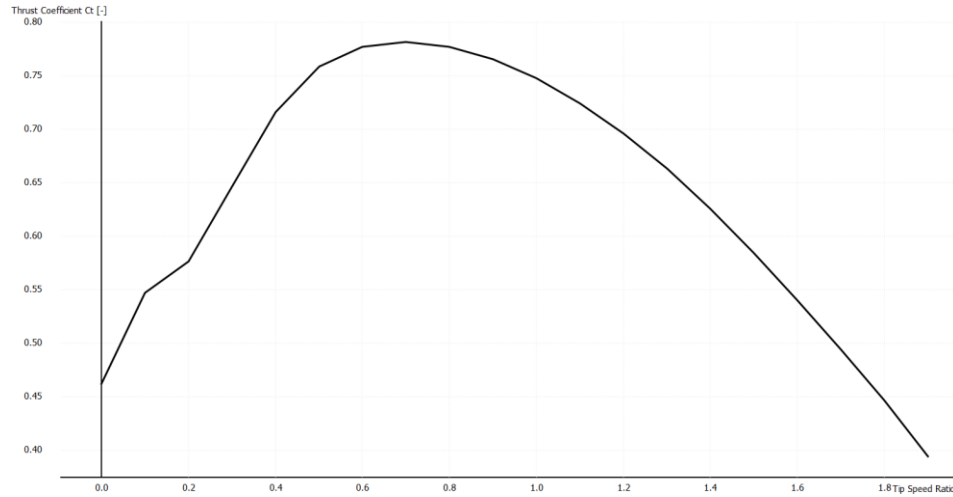


**Figure 5.7** Thrust coefficient of the wind turbine.

**Table 5.1** Poly BEM vs No Poly BEM correction.

	Optimal angle	BEM Torque	CFD Torque	Relative Error
Poly BEM DTU correction	24°	0.5450	0.4372	20%
Without Poly BEM DTU correction	29°	0.5070	0.4656	8%

## 5.2 Experimental results

As soon as the scale model and the test bench have been made, we start the validation tests of such a model. To simulate the wind flow, we used a wind tunnel, the results of the experiment are presented in the following.

### 5.2.1 Discussion of experimental tests

First of all, in order to calculate the braking torque, we used a series of mass with increments of 50 g, and we increased the wind speed by a step of 0.1 m/s until the wind turbine started and we recorded the corresponding speed.

**Table 5.2** Results of wind speed measurements.

Mass (g)	100	150	200	300	400	500	600	700
Wind speed (m/s)	2.1	2.6	3.3	4.2	5	5.6	6.1	6.9
Braking Torque (N.m)	0.049	0.074	0.098	0.147	0.196	0.246	0.295	0.344

After having the wind speed series, we had to have the rotation speed for each point. This was achieved with a free wind turbine without a resistant load (without mass). And using the equation 5.3 relation we have to calculate the TSR

$$\lambda = \frac{\omega R}{v} \quad (5.3)$$

To have the uncertainty of the TSR

$$\frac{\Delta\lambda}{\lambda} = \frac{\Delta\omega}{\omega} + \frac{\Delta R}{R} + \frac{\Delta v}{v} \quad (5.4)$$

And the uncertainty of power is calculated as follows

$$\Delta\lambda = \lambda \left( \frac{\Delta\omega}{\omega} + \frac{\Delta R}{R} + \frac{\Delta v}{v} \right) \quad (5.5)$$

**Table 5.3** Results of rotational speed measurements.

Wind speed (m/s)	2.1	2.6	3.3	4.2	5	5.6	6.1	6.9
Rotation speed (RPM)	57.5	82	135	200	268	300	330	410
TSR	0.76	0.875	1.135	1.321	1.487	1.487	1.501	1.649
$\Delta\lambda$	0.110	0.103	0.105	0.097	0.092	0.082	0.077	0.075

The next step is to determine the performance parameters using the following formulas  
To calculate the torque

$$T = Mgr \quad (5.6)$$

Where  $g = 9.82 \text{ m/s}^2$ ,  $r = 0.05 \text{ m}$  and  $M$  is mass in  $kg$   
To calculate the power for each point in this way

$$P = T \cdot \omega \quad (5.7)$$

Where  $\omega$  is the rotation speed in  $rad/s$   
To calculate the uncertainty of the power

$$\frac{\Delta P}{P} = \frac{\Delta T}{T} + \frac{\Delta \omega}{\omega} \quad (5.8)$$

Then

$$\frac{\Delta P}{P} = gr \frac{\Delta M}{M} + \frac{\Delta \omega}{\omega} \quad (5.9)$$

And the uncertainty of power is calculated as follows

$$\Delta P = P \left( gr \frac{\Delta M}{M} + \frac{\Delta \omega}{\omega} \right) \quad (5.10)$$

To calculate the power coefficient

$$C_p = \frac{P}{\frac{1}{2} \rho \pi \frac{d^2}{4} v^3} \quad (5.11)$$

Where  $\rho = 1.225 \text{ kg/m}^3$  and  $d$  is the rotor diameter

To calculate the uncertainty of the power coefficient

$$\frac{\Delta C_p}{C_p} = |1| \frac{\Delta P}{P} + |-3| \frac{\Delta v}{v} + |-2| \frac{\Delta d}{d} \quad (5.12)$$

Then

$$\Delta C_p = C_p \left( |1| \frac{\Delta P}{P} + |-3| \frac{\Delta v}{v} + |-2| \frac{\Delta d}{d} \right) \quad (5.13)$$

Torque coefficient is then deduced

$$C_m = \frac{C_p}{\lambda} \quad (5.14)$$

To calculate the torque coefficient uncertainty

$$\frac{\Delta C_m}{C_m} = \frac{\Delta C_p}{C_p} + \frac{\Delta \lambda}{\lambda} \quad (5.15)$$

Then

$$\Delta C_m = C_m \left( \frac{\Delta C_p}{C_p} + \frac{\Delta \lambda}{\lambda} \right) \quad (5.16)$$

## 5.2.2 Comparative study between BEM, CFD and experimental results

Table 5.4 summarizes the results of the mesh 1 chosen in the previous chapter 3 as well as the values predicted by QBlade using the BEM theory with the correction tip loss and 3d correction. This good agreement of the results comes down to the optimization and homogeneity of the chosen mesh, which allows the solver to grasp the main flow characteristics.

**Table 5.4** Comparison between BEM, CFD and experimental results.

TSR	BEM		CFD			Experimental				
	$C_p$	$C_m$	$C_p$	$C_m$	Relative Error	$C_p$	Incertainty $\Delta C_p$	$C_m$	Incertainty $\Delta C_m$	Relative Error
0.760	0.289	0.380	0.264	0.347	8.684%	0.236	$\pm 0.0958$	0.311	$\pm 0.0958$	18.18%
0.875	0.311	0.355	0.283	0.323	9.014%	0.266	$\pm 0.0731$	0.304	$\pm 0.0731$	14.30%
1.135	0.341	0.300	0.312	0.275	8.333%	0.286	$\pm 0.0484$	0.252	$\pm 0.0484$	16.06%
1.321	0.357	0.270	0.334	0.253	6.296%	0.308	$\pm 0.0339$	0.233	$\pm 0.0339$	13.63%
1.421	0.369	0.260	0.347	0.244	6.154%	0.312	$\pm 0.0262$	0.219	$\pm 0.0262$	15.62%
1.487	0.376	0.253	0.357	0.240	6.957%	0.325	$\pm 0.0223$	0.219	$\pm 0.0223$	13.59%
1.501	0.378	0.252	0.362	0.241	7.540%	0.332	$\pm 0.0201$	0.221	$\pm 0.0201$	12.26%
1.649	0.407	0.247	0.391	0.237	8.907%	0.332	$\pm 0.0161$	0.202	$\pm 0.0161$	18.38%

We observe that the experimental performance results of the scaled-down model, constructed according to similarity principles, and the prototype show a maximum error of 18% as seen in table 5.4 and Figure 5.8. Nonetheless, it is worth noting that the experimentation was beneficial for validating the results. As for the accuracy of the results, it remains very good due to the digital equipment used and the proper handling of this equipment as seen in error bars in Figure 5.9.

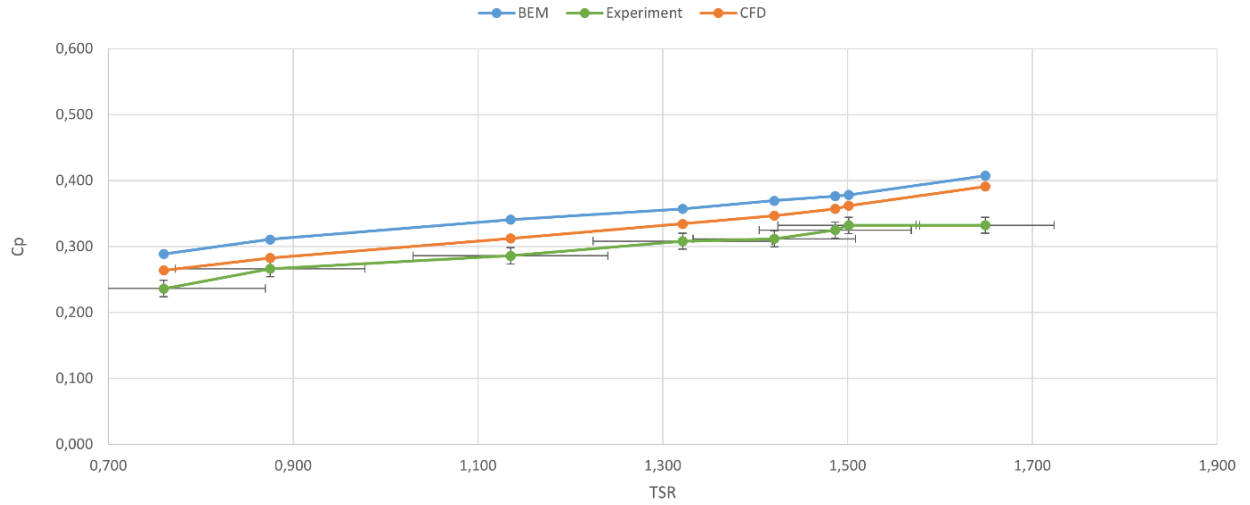


Figure 5.8 Cp-TSR curve comparison between BEM, CFD and experimental results.

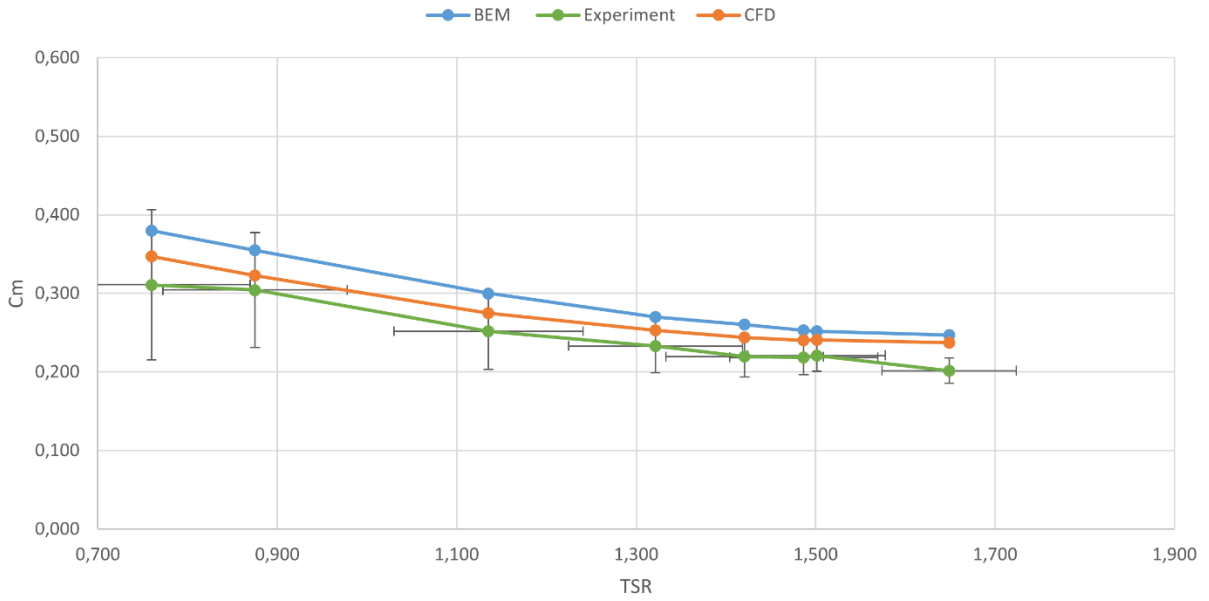


Figure 5.9 Cm-TSR curve comparison between BEM, CFD and experimental results.

# General conclusion

The primary objective of this project is to address a crucial need for water. As a solution, we proposed designing a wind pump based on reverse engineering and rigorous optimization, supported by scientific research. Next, we built a scaled-down model of a wind turbine and a test bench designed to measure its dynamic torque, then tested the performance of this model in a wind tunnel. Another objective was to model and simulate the wind turbine in 3D using the CFD software Fluent. The design and construction of our scaled-down wind turbine and test bench allowed us to master the use of SolidWorks software and to improve our proficiency with 3D printers. The difficulties encountered during the production phase taught us a lot, especially how to overcome them and find alternative solutions to each problem, notably during the construction of the rotor and the frameworks. In the end, we managed to build our wind turbine model, test it, and validate the simulation and experimental results by comparing them to numerical references computed through QBlade software.

The results demonstrated significant findings from both numerical CFD simulations and experimental work. Experimental results showed a good agreement with the numerical predictions, validating the reduced model used in the study. The comparative study between Blade Element Momentum (BEM), CFD, and experimental results indicated a maximum error of 30%, with detailed analysis providing insights into performance and optimization potential for wind-powered piston pumps.

## Project Perspectives:

- Proceed with further development of the scaled model using steel and reel manufacturing techniques. Additionally, integrate a transmission system and a pump for water lifting to strengthen the study.
- For the simulation phase, recommend exploring alternative turbulence models such as the SST  $k-\omega$  model for varying wind speeds. Compare these findings with results obtained using the Spalart-Allmaras model utilized in our current research.
- Enhance the instrumentation on the test bench to ensure more accurate and reliable measurements. Consider future projects including the use of a generator to assess electrical power production and various efficiencies.
- Fabricate a full-scale wind pump and deploy it under real operational conditions.

# References

1. H. Daaou Nedjari , S. Kheder Haddouche, A. Balehouane, O. Guerri. Optimal windy sites in Algeria: Potential and perspectives. *Energy* 147 (2018) 1240-1255.
2. Yelmen, B., Kurt, C., & Çakır, M.T.(2021). Water Pumping Systems with Wind Turbines in Sinop. *European Journal of Science and Technology*, (31), 515-522.TATA
3. Madjid, *Bulletin des Energies Renouvelables* N°49 – 2020
4. Donald Routledge Hill, « Mechanical Engineering in the Medieval Near East », *Scientific American*, mai 1991, p. 64-69.
5. « Water-lifting mills in the Région de Murcie, Espagne », sur [yachtmollymawk.com](http://yachtmollymawk.com), novembre 2008.
6. Bernard Forest de Bélidor, *Architecture hydraulique ou l'art de conduire, d'élever, et de ménager les eaux*, vol. 1 à 2, Charles-Antoine Jombert, 1739.
7. By T. Lindsay Baker, « Brief History of Windmills in the New World », in [windmillersgazette.com](http://windmillersgazette.com). Posted on July 18, 2015 by ssneed, consulted July 19, 2024. <https://windmillersgazette.org/brief-history-of-windmills-in-the-new-world>
8. Paul Gipe, *Wind Energy Comes of Age*, John Wiley and Sons, 1995
9. Willard on 17/04/2019. Windpump on Wikipedia website. <https://en.wikipedia.org/wiki/Windpump>
10. O. Guerri, K. Ameur, A. Kaabache, S. Moussa et A. Harhad. Pompage de l'Eau à l'Aide d'un Aérogénérateur Utilisation de L'Energie Eolienne pour le Pompage de l'Eau dans la Région d'Adrar. *Rev.Energ Ren.: Zones Arides*, pp.63-68, 2002.
11. Aermotor windmill company. Windmill pumping capacities on aermotor windmill website. Consulted in July 19, 2024. <https://aermotorwindmill.com/pages/windmill-pumping-capacities>.
12. K. AMEUR dans le *Bulletin des énergies renouvelables* - N° 2 Décembre 2002. Page 14
13. CDER, *Bulletin des énergies renouvelables* - N° 48 2019. Page 12-19.
14. A. Samil, *Bulletin des Energies Renouvelables*, N°4, Décembre 2003.
15. K. Bendiff, *L'expérience du HCDS dans le développement des Energies renouvelables*, 2008
16. GUERRI Ouahiba dans le *Bulletin des Energies Renouvelables* - N° 21 2011 page 3-4

17. Maouedj, Rachid & Bousalem, Souad. (2008). Optimisation d'un système de pompage éolien Application aux sites sahariens. *Revue des Énergies Renouvelables*. 11. 10.54966/jreen.v11i2.73.
18. Chamlong Prabkeao, Akapot Tantrapiwat. Study on wind energy potential for agricultural water pumping system in the middle part of Thailand. *MATEC Web Conf*. 192 03058 (2018). DOI: 10.1051/mateconf/201819203058
19. Nghi, Nguyen & Gavino, Helen & Regalado, M.J.C.. (2015). Optimizing water utilization from a windpump-drip irrigation system for high-value crop production. *International Journal of Geomate*. 8. 1293-1299. 10.21660/2015.16.4118.
20. YEK (2019) :Republic of Turkey Ministry of Energy and Natural Resources. General directorate of renewable energy. <https://enerji.gov.tr/enerji-isleri-genel-mudurlugu-yenilenebilir-enerji>
21. Réalisé par Alizés Sénégal, Capitalisation 1997-2003, EER/SEMIS/GRET. Cahier n°5 : Modèles techniques et critères de choix, p.1. [https://www.pseau.org/outils/ouvrages/gret\\_alizes\\_electrique\\_cahier\\_capitalisation\\_05.pdf](https://www.pseau.org/outils/ouvrages/gret_alizes_electrique_cahier_capitalisation_05.pdf)
22. N. Argaw, Renewable Energy for Water Pumping Applications in Rural Villages, NREL Report 30361, 2003, p. 27.
23. L. Vadot (1957) Water pumping by windmills, *La Houille Blanche*, 43:4, 496-535, DOI: 10.1051/lhb/1957044
24. Siddig, Mohammed. (2010). Operation Theory of Wind Pumps. *Wind Engineering*. 34. 361-373. 10.1260/0309-524X.34.4.361.
25. Manwell, J.F., McGowan, J.G. & Rogers, A.L., *Wind Energy Explained: Theory, Design and Application*, 2nd edn. John Wiley and Sons, Ltd.: West Sussex, UK, 2009.
26. H Glauert. *Airplane propellers, aerodynamic theory: A general review of progress*, edited by F. W. Durand. Springer, 4 :169–360, 1935.
27. W. Timmer. Aerodynamic characteristics of wind turbine blade airfoils at high angles-of-attack. *American Journal of Medical Genetics Part A - AM J MED GENET PART A*, 01 2010
28. Z. Du and Micheal S. Selig. 3-D stall-delay model for HAWT performance prediction. 1997.
29. J.J Corrigan and J. J. Schilling. Empirical model for stall delay due to rotation. San Francisco, CA, Jan 1994. American Helicopter Society Aeromechanics Specialists.
30. John Chapman, Ian Masters, M. Togneri, and J.A.C. Orme. The buhl correction factor applied to high induction conditions for tidal stream turbines. *Renewable Energy*, 60 :472–480, 12 2013.

31. R. Dhepakumar, R. Ganesh. Reverse Engineering in Mechanical Component. International Journal of Engineering Research & Technology (IJERT) ISSN: 2278-0181. CONFCALL - 2019 Conference Proceedings
32. Prepared by Miss T.Rastogi. Wind pump handbook in May 1982. <https://www.ircwash.org/sites/default/files/232.3-82WI.pdf>
33. Aized T, Sohail Rehman SM, Kamran S, Kazim AH, Ubaid ur Rehman S. Design and analysis of wind pump for wind conditions in Pakistan. *Advances in Mechanical Engineering*. 2019;11(9). doi:10.1177/1687814019880405
34. John, Itoje & Wood, David & Vaz, Jerson. (2022). Helical vortex theory and blade element analysis of multi-bladed windmills. *Wind Energy*. 26. 10.1002/we.2796.
35. Pengky, wind rotor solidity on the site pengky.cn <https://www.pengky.cn/zz-horizontal-axis-turbine/05-wind-rotor-solidity/wind-rotor-solidity.html#:~:text=The%20concept%20of%20wind%20rotor>
36. Anonymous in August 2012. Wind turbine design - blade count section on Wikipedia website. [https://en.wikipedia.org/wiki/Wind\\_turbine\\_design](https://en.wikipedia.org/wiki/Wind_turbine_design).
37. Jansen, W. A. M., & Smulders, P. T. (1977). Rotor design for horizontal axis windmills. (SWD publications; Vol.7701). Stuurgroep Windenergie Ontwikkelingslanden.
38. Cambered plate C=16% T=5% R=0.86 (cp-160-050-gn) in Airfoil tools. <http://airfoiltools.com/airfoil/detail?s?airfoil=cp-160-050-gn>.
39. Lin, Khaing & Htay, Thwe & Win, Su. (2018). Aerodynamic Analysis of Curved Blade for Water Pumping Windmill. *International Journal of Science and Engineering Applications*. 7. 307-312. 10.7753/IJSEA0709.1012.
40. GINA STOICA, BERNARD LEDUC méthodologie de calcul et de conception d'un réducteur d'engrenage cylindrique ou conique; université POLITHNICA de Bucarest, université libre de Bruxelles, année 2009.
41. Nakacho Kawaguchi-shi Saitama-ken. Involute Gear Profile in gear knowledge. Consulted July 19, 2024. [https://khkgears.net/new/gear\\_knowledge/gear\\_technical\\_reference/involute\\_gear\\_profile.html](https://khkgears.net/new/gear_knowledge/gear_technical_reference/involute_gear_profile.html)
42. Van Treuren, Kenneth. (2015). Small-Scale Wind Turbine Testing in Wind Tunnels Under Low Reynolds Number Conditions. *Journal of Energy Resources Technology*. 137. 10.1115/1.4030617.
43. Gao, X. & Hu, J., Numerical research of Reynolds number impact on scale model of wind turbine. *IEEE World Non-Grid-Connected Wind Power and Energy Conference*, Nanjing, China, pp. 1–4, 2009.
44. Beslagic, Ernad & Lemeš, Samir & Hadžikadunić, Fuad. (2020). Procedure for Determining the Wind Tunnel Blockage Correction Factor. 10.1007/978-3-030-46817-0\_38.
45. Hamlaoui, Mohammed Nadjib & Bouhelal, Abdelhamid & Smaïli, Arezki & Fellouah, H. (2024). An Engineering Approach to Improve Performance

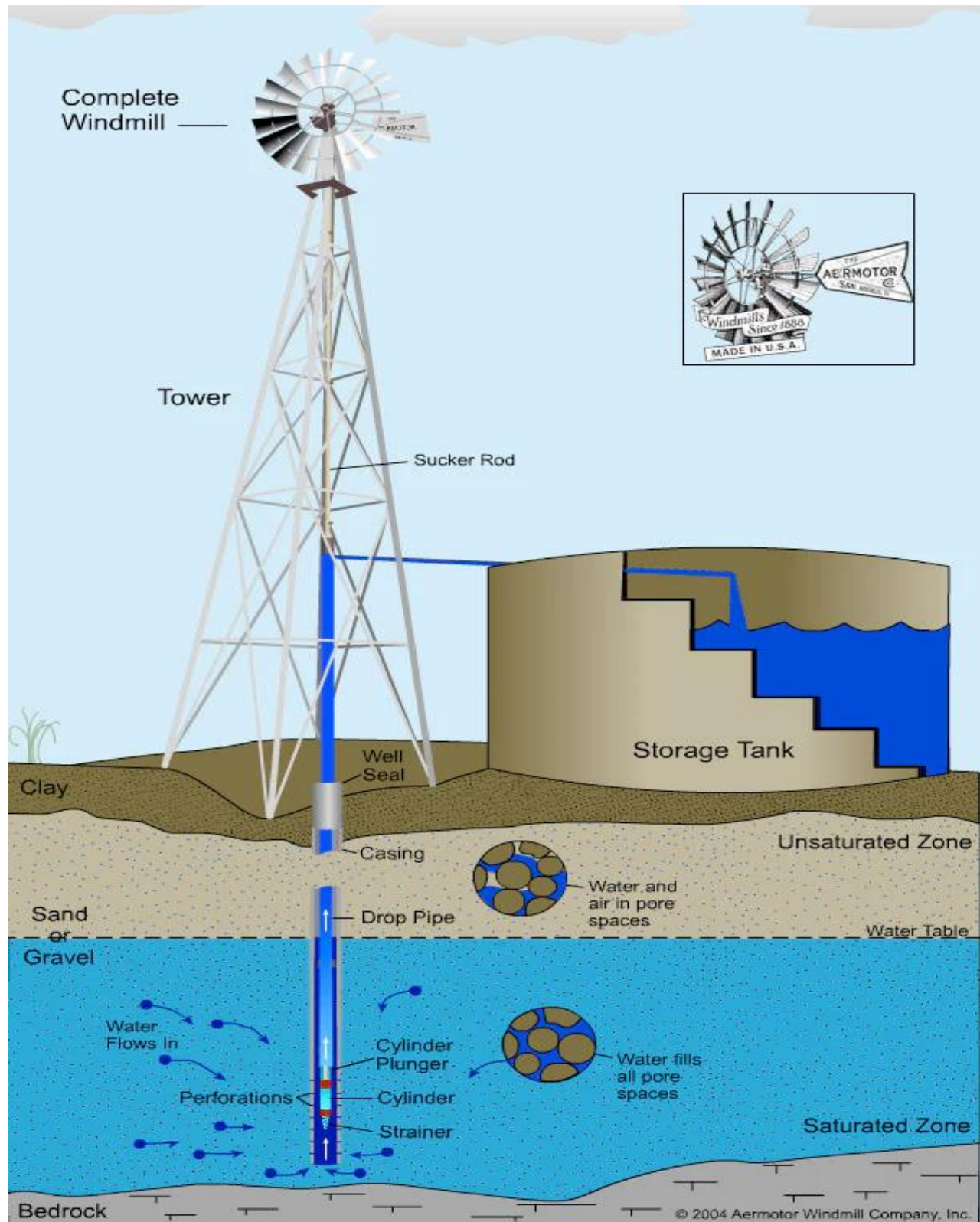
- Predictions for Wind Turbine Applications: Comparison with Full Navier-Stokes Model and Experimental Measurements. *Journal of Applied Fluid Mechanics*. 17. 1379-1397. 10.47176/jafm.17.7.2404.
46. Jousefm November 2020. What's y plus in simscale site. <https://www.simscale.com/forum/t/what-is-y-plus/82394>
47. Sanaa El Mouhsine, Karim Oukassou, Mohammed Marouan Ichenial, Boussselham Kharbouch, Abderrahmane Hajraoui, Aerodynamics and structural analysis of wind turbine blade, *Procedia Manufacturing*, Volume 22, 2018, Pages 747-756, ISSN 2351-9789, <https://doi.org/10.1016/j.promfg.2018.03.107>.
48. Panayampilly\_Abdul\_Samad. Lecture 7 : Turbulence Modelin. Introduction to Ansys fluent introduction. [https://www.researchgate.net/profile/Panayampilly\\_Abdul\\_Samad/post/y\\_plus\\_range\\_for\\_turbulent\\_models/attachment/59d6393c79197b8077996735/AS%3A400990483304449%401472614989133/download/Fluent-Intro\\_15.0\\_L07\\_Turbulence.pdf](https://www.researchgate.net/profile/Panayampilly_Abdul_Samad/post/y_plus_range_for_turbulent_models/attachment/59d6393c79197b8077996735/AS%3A400990483304449%401472614989133/download/Fluent-Intro_15.0_L07_Turbulence.pdf)
49. Christopher Rumsey in 02/06/2024. Nasa Official website. <https://turbmodels.larc.nasa.gov/spalart.html>
50. Madsen, H. A., Larsen, T. J., Pirrung, G. R., Li, A., and Zahle, F.: Implementation of the blade element momentum model on a polar grid and its aeroelastic load impact, *Wind Energ. Sci.*, 5, 1–27, <https://doi.org/10.5194/wes-5-1-2020>, 2020.

# Appendices

## Appendix A

### Descriptive diagram of the wind pump

#### A. Mechanism of a slow wind turbine



# Appendix B

## Wind Pump Technical Document

### B.1 Poval Windmill Data Sheet

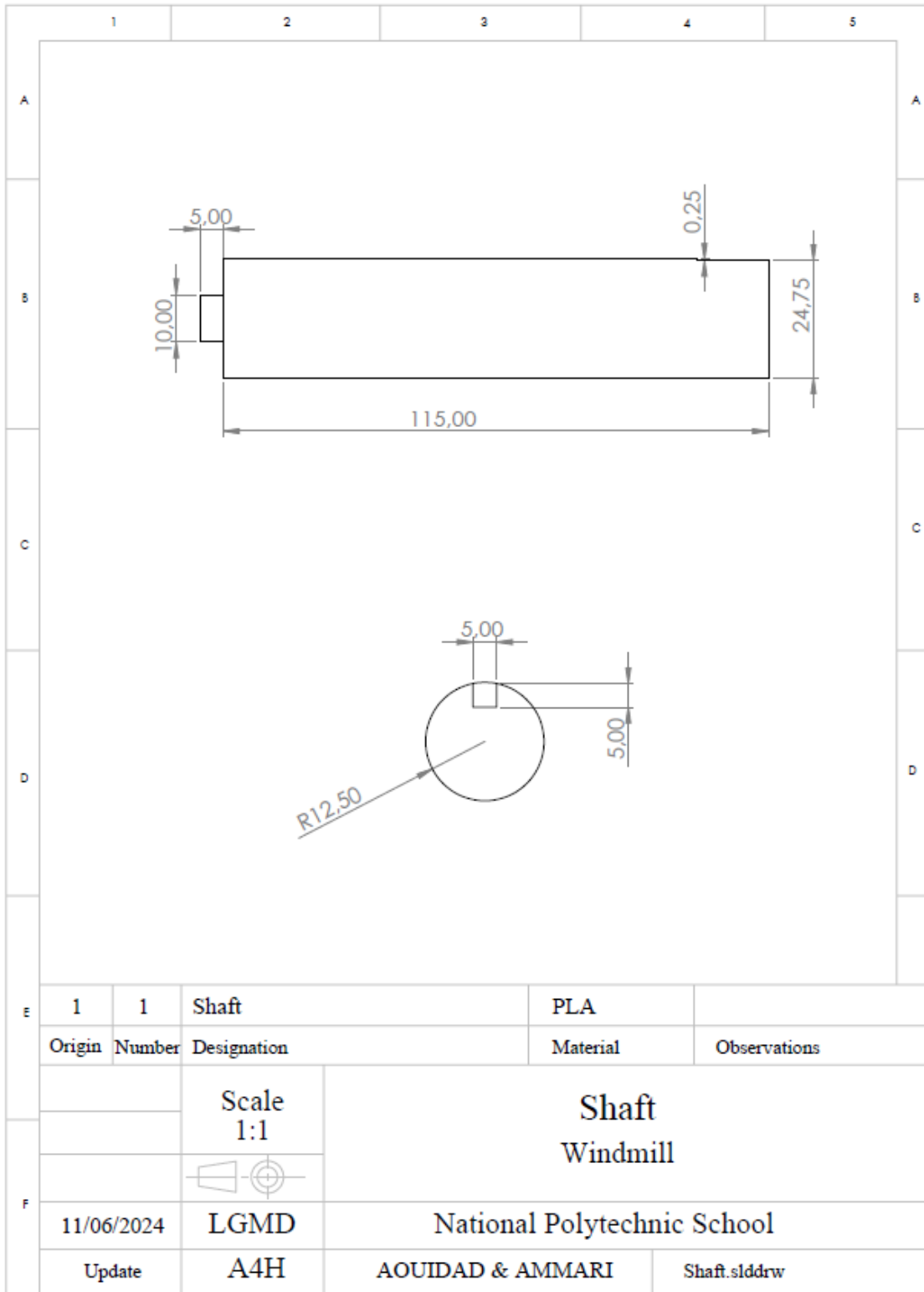
Pump Diametres (in mm)	Capacity in Litre/hour		AE8	AE 10	Total manometrical height in meter wheel diameter (in meter)			
	1.8	2.4 à 4.8	1.8	2.4	3	3.6	4.2	4.8
50	490	790	28	42	65	96	138	225
57	680	1000	23	34	52	77	110	160
63	850	1230	19	29	43	65	92	150
70	1000	1460	17	25	37	55	80	130
76	1210	1780	14	21	31	47	67	110
82	1400	2075	12	17	27	40	57	93
90	1665	2420	10	15	23	35	49	82
95	1890	2750	9	13	20	30	44	70
100	2155	3150	8	12	18	26	38	61
108		3555		10	15	23	33	54
114	2740	4000	6	9	14	21	30	49
120		4425			12	18	26	42
127	3400	4900	5	8	11	17	24	40
146		6430				12	18	30
152		7100		5	8	11	17	26
178		9650		5	6	8	12	19
203		12490			4	7	9	15

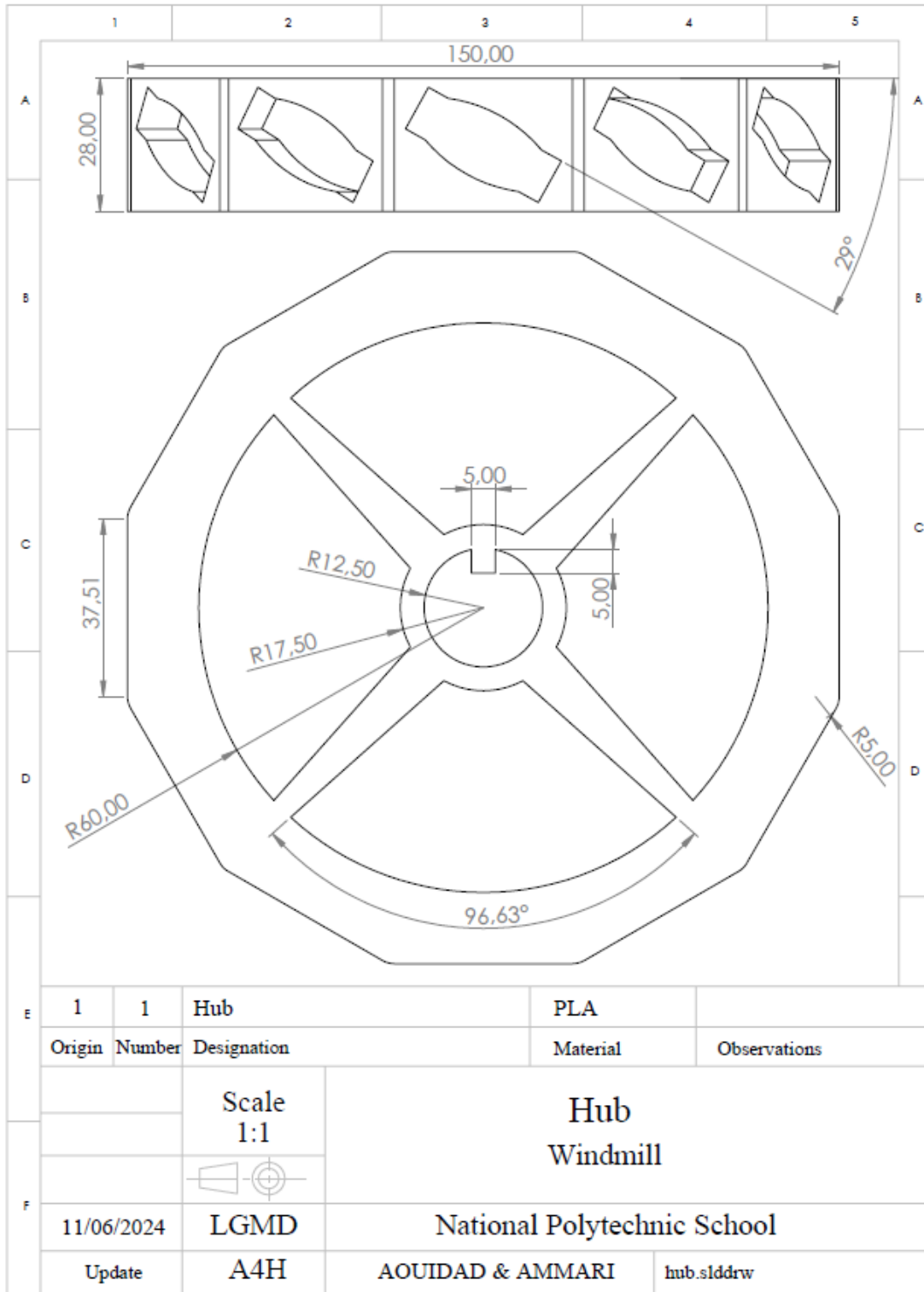
## B.2 Proposed Windmill Data Sheet

<b>Windmill with 3 meters rotor diameter</b>			
<b>Piston diameter (m)</b>	<b>Stroke (m)</b>	<b>Head (m)</b>	<b>Capacity (l/h)</b>
<b>Short stroke</b>			
0,050	0,100	267	383
0,057	0,100	205	498
0,063	0,100	168	608
0,070	0,100	136	751
0,076	0,100	115	888
0,082	0,100	99	1031
0,090	0,100	82	1245
0,095	0,100	74	1380
0,100	0,100	67	1524
0,108	0,100	57	1791
0,114	0,100	51	2002
0,120	0,100	46	2219
0,127	0,100	41	2490
0,146	0,100	31	3293
0,152	0,100	29	3520
0,178	0,100	21	4861
0,203	0,100	16	6380
<b>Long stroke</b>			
0,050	0,200	133	765
0,057	0,200	103	991
0,063	0,200	84	1215
0,070	0,200	68	1501
0,076	0,200	58	1760
0,082	0,200	50	2042
0,090	0,200	41	2490
0,095	0,200	37	2759
0,114	0,200	26	3926
0,120	0,200	23	4438
0,127	0,200	21	4861
0,146	0,200	16	6380
0,152	0,200	14	7292
0,178	0,200	11	9280
0,203	0,200	8	12760

# Appendix C

## Technical Drawings





=

